Torsion Balance Investigation of the Casimir Effect

A thesis
submitted for the Degree of

Doctor of Philosophy

in

The Faculty of Science

Bangalore University

by

G RAJALAKSHMI

Indian Institute of Astrophysics

Bangalore 560 034, India

May 2004

Declaration

I hereby declare that the matter contained in this thesis is the result of the investigations carried out by me at the Indian Institute of Astrophysics, Bangalore, under the supervision of Prof. R. Cowsik. This work has not been submitted for the award of any degree, diploma, associateship, fellowship etc. of any university or institute.

Prof. R. Cowsik
(Thesis Supervisor)

G Rajalakshmi
(Ph.D. Candidate)

Indian Institute of Astrophysics

Bangalore 560 034, India

May, 2004

Certificate

This is to certify that the thesis entitled ' Torsion Balance Investigation of the Casimir Effect' submitted to the Bangalore University by Ms. G. Rajalakshmi for the award of the degree of Doctor of Philosophy in the faculty of Science, is based on the results of the investigations carried out by her under my supervision and guidance, at the Indian Institute of Astrophysics, Bangalore. This thesis has not been submitted for the award of any degree, diploma, associateship, fellowship etc. of any university or institute.

Indian Institute of Astrophysics,
Bangalore
May, 2004

Prof. R Cowsik
(Thesis Supervisor)

Acknowledgements

I thank Prof. R. Cowsik for his guidance and continuous support as my thesis advisor during the course of this work. I have learnt many aspects of research from discussion with him.

I thank Dr. C. S. Unnikrishnan for his support and encouragement throughout - as a colleague and as a friend. His never ending stream of crazy-sounding ideas are a constant source of inspiration.

I have gained a lot from discussions with Dr. N. Krishnan and Prof. S. N Tandon. Their open criticisms have put me on the right track many a times.

I thank Prof. R. Srinivasan, for the technical help and support he provided in building the experiment, especially the CCD optical lever.

I thank Dr. B. R. Prasad and Dr. Pijush Bhattacharjee, who as doctoral committee members helped in advancing the thesis.

I thank Prof. B. P. Das, Dr. Sharath Ananthamurthy, Prof. C. Sivaram, Dr. A. K. Pati and Dr. Andal Narayanan for the interesting discussions I have had with them.

I thank Suresh for his patient support and companionship during the years it took to build the experiments.

I thank Ms. A. Vagiswari, Ms. Christina Birdie and all the other library staff for the excellent library facility provided at the Institute.

I thank the present and past members of the Board of Graduate Studies for their help and guidance.

I thank Mr. J. P. A. Samson, Mr. Thimmiah, Mr. Sagayanathan and Mr. Periyanayagam of the mechanical workshop for their help with the design and fabrication of the various mechanical parts of the experimental apparatus.

Building a lab requires support and advice from many people on aspects ranging from instrumentation to administration, it is impossible to acknowledge everybody's

contribution individually. I thank all the staff of IIA who helped in the setting up of the 'Zerolab'. I thank the staff of the computer center, electrical section, photonics and the administration for their continuous support.

I thank the present and past Chairmen of the Physics Department of Bangalore University and the members of staff in the University for their help with the administrative matters related to the thesis.

The several years I have spend in IIA was made pleasant by the many wonderful friends that I was lucky to have. I thank - Ramesh, Krishna, Sankar, Sivarani, Geetha, Sridharan and Rajesh Kumapuaram for introducing me into IIA; Mogna and Holger for being there during hard times; Arun, Rana and Pratho for those numerous discussion - scientific and otherwise; Dharam for being a nag and for the care; Manoj for the enumerable arguments on wide ranging topics; Appu for being such a patient listener; Ravi for help in a many a things- personal and technical; Preeti, Latha, Sivarani and Shalima for those many early morning chais; Geetanjali for being a wonderful roommate. I also thank E Reddy, Sujan, Annapurani, Srikanth, Rajguru, Pandey, Swara, Bhargavi, Sanjoy, Pavan, Mangala, Jana, Ramachandra, Ambika, Shanmugham, Kathiravan, Reji, Sahu, Malai, Jayendra, Nagaraj and Maiti for making my stay at IIA enjoyable.

I thank Pramila, Rani and Samson for their hospitality and care.

I thank my loving parents whose guidance and encouragement has made me what I am. My brother, Sankar for his silent support and affection. I thank Raja for enduring me through these years and being a constant source of encouragement and companionship. Athai and Athember for their affection and support. Last but not the least, I thank my grand fathers - Chandrasekharan, Ananthanarayanan and Krishnamurthy - who at a very young age guided me in developing a personality of my own. To them I dedicate this thesis.

CONTENTS

1. INTRODUCTION

Abstract: This chapter presents an overview of the theoretical background and the motivations for the experiment. The chapter begins with a general description of Casimir force, with discussions on the effect of finite temperature and finite conductivity. This is followed by a short historical review of the earlier experiments to measure Casimir force. The recent motivations to study Casimir force are then presented.

1.1 Casimir Force - an introduction

Even Schwinger, who was awarded the Nobel Prize for his pioneering contribution to Quantum Electrodynamics, has remarked that one of the least intuitive consequences of Quantum electrodynamics is the existence of a force of attraction between two perfectly conducting uncharged plates [45]. In 1948, H. B. Casimir [3], showed that for two infinite parallel plates, separated by a distance d, this force per unit area is given by,

$$F_c(d) = -\frac{\pi^2 \hbar c}{240 d^4} \tag{1.1}$$

$$= -\frac{0.013}{d_\mu^4} \quad \text{dyn. cm}^{-2} \quad \text{where } d_\mu \equiv d \text{ in microns} \tag{1.2}$$

The force is independent of the charge or mass of the plate. For plates of 1 cm^2 area separated by 1 μm, the force is comparable to the gravitational attraction of two 400 g masses separated by 1 cm or the Coloumb force on the electron in a hydrogen atom.

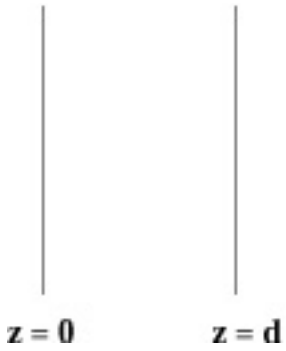

Fig. 1.1: Two perfectly conducting infinite plates, placed distance d apart.

1.1.1 Casimir force as a manifestation of zero point energy

When electromagnetic field is described quantum mechanically, it has properties similar to an assembly of quantized harmonic oscillators. Each mode of the electromagnetic field defined by a set of parameters like frequency and polarization, is represented by one oscillator. The allowed energy levels of an electromagnetic wave of angular frequency ω are given by the Planck relation $E_n = (n+\frac{1}{2})\hbar\omega, n = 0, 1, 2, 3 \ldots$. The integer n, for the electromagnetic field, corresponds to the number of photons. Thus, even the zero quanta or the 'vacuum' state of the field still contains field fluctuations which result in a non-zero energy. In free space, all modes (frequencies) of the electromagnetic wave are possible and each mode has a finite energy. As a consequence the vacuum or the zero photon state of the electromagnetic field in free space has infinite energy and infinite energy density. However, physically real effects arising from quantum fluctuations in the vacuum turn out to be finite and"renormalized". One example is the Lamb shift of atomic energy levels.

These vacuum field fluctuations also give rise to measurable mechanical effects on macroscopic systems which manifest as Casimir forces [29]. If an infinite, planar cavity comprising of perfect conducting plates separated by a distance, d, is placed in 'vacuum', it imposes boundary conditions on the zero-point electromagnetic fluctuations. As a result, the possible modes of the electromagnetic field is restricted within

the cavity. Thus there is a finite difference in the energy of the vacuum field outside and inside the cavity. This results in a quantum vacuum pressure that attracts the cavity plates together. For the zero photon state, this pressure is given by Eqn. 1.1 (see Appendix A for details).

1.1.2 Effect of Finite Temperature

The non-vacuum state of the electromagnetic field also has a Casimir force associated with it. In general at any finite temperature, T, thermal fields are also present in addition to the vacuum electromagnetic fields and the possible energy levels are given by the Planck's spectrum,

$$E_n = \left(n(\omega) + \frac{1}{2} \right) \hbar\omega, \text{ where } n(\omega) = \frac{1}{e^{\frac{\hbar\omega}{k_B T}} - 1}. \tag{1.3}$$

The Casimir vacuum pressure (force per unit area) is then given by [5],

$$F_c^T(d) = -\frac{k_B T}{4\pi d^3} \sum_{n=0}^{n}{}' \int_{nx}^{\infty} \frac{dy y^2}{e^y - 1} \quad \text{where } x \equiv 4\pi k_B T d/\hbar c^{\dagger} \tag{1.4}$$

$$F_c(d) \simeq -\frac{\pi^2 \hbar c}{240 d^4} \quad \text{at low } T \ (i.e.\ x \ll 1)$$

$$F_c^T(d) \simeq -\frac{\zeta(3) k_B T}{4\pi d^3} \quad \text{at high } T \ (i.e.\ x \gg 1) \tag{1.5}$$

$$\text{with } \zeta(3) = 1.20206 \tag{1.6}$$

From these results note that *the distance dependence changes from* $1/d^4$ *at low temperatures to* $1/d^3$ *at high temperatures.*

Considering Eqn. 1.5, it is obvious that the important non-dimensional parameter, that distinguishes the domains of *high* and *low* temperature, is $x = 4\pi k_B T d/\hbar c$. *Moreover, it is interesting to note that high temperature also corresponds to larger*

[†] The prime over the summation symbol means that a factor half should be inserted for the $n = 0$ term. See for example [5]

Fig. 1.2: Two semi-infinite dielectric slabs of dielectric constants ϵ_1 and ϵ_2, placed distance d apart in vacuum.

separation d between the plates and vice versa. Thus at any given temperature, the law which governs the vacuum pressure will depend on the distance between the plates. No experiment till date has been able to observe these finite temperature corrections to Casimir force, due to limitations in sensitivity in the distance range where such effects start to become significant.

The primary aim of the work described in this thesis is to observe the Casimir force in the distance range where this change in the distance dependance of the force occurs. At a temperature of $\sim 300^\circ$ K, the change from $1/d^4$ to $1/d^3$ is expected to occur at about 2 μm to 4 μm. Our experiments scan separations from about 1 μm to 10 μm and thus will be able to probe this change over from the low temperature to the high temperature domain.

1.1.3 Effect of Finite Conductivity

The discussions so far assumed that the cavity plates are perfectly conducting, i.e, they have infinite conductivity at all frequencies of the electromagnetic field. In experimental situations, this simplified assumption is unrealistic and the dielectric properties of the cavity plates should also be considered.

Liftshitz [4] , developed the first macroscopic theory of forces between dielectrics. His results reduce to the Casimir force given by Eqn. 1.1 for the case of perfect conductors. For finite size plates with dielectric constants $\epsilon_1(\omega)$ and $\epsilon_2(\omega)$ [Fig. 1.2], the Casimir force per unit area is given by the Liftshitz formula,

$$\begin{aligned} F_c^p(d) &= -\frac{\hbar}{2\pi^2 c^3}\int_1^\infty dp\ p^2 \int_0^\infty d\xi\ \xi^3 \\ &\left[\left\{\frac{s_1+\epsilon_1 p}{s_1-\epsilon_1 p}.\frac{s_2+\epsilon_2 p}{s_2-\epsilon_1 p}.e^{2\xi p d/c}-1\right\}^{-1}\right. \\ &\left.+\left\{\frac{s_1+p}{s_1-p}.\frac{s_2+p}{s_2-p}.e^{2\xi p d/c}-1\right\}^{-1}\right] \end{aligned} \tag{1.7}$$

where $s_i,\ p$ are variables that depend on the dielectric constants ϵ_i of the medium and the wave vector k of the electromagnetic field. (see Appendix A for details).

1.1.4 Importance of these effects for experiments

The experiments on Casimir force are typically carried out at room temperature using metals with finite electrical conductivity. In order to make a comparison between the experiments and the theory, it is essential to quantify the effects of temperature and conductivity. As summarized above the effects of the thermal field fluctuations on the Casimir force are known to become important when the spacing between the boundaries is of the order of the characteristic length, $\lambda_T = \frac{2\pi}{\omega_T}$. ω_T is the dominant thermal angular frequency at the temperature T. Similarly, the plasma frequency ω_p of the metal determines the length scale, λ_p at which the finite conductivity effects are appreciable, i.e, $\lambda_p = \frac{2\pi}{\omega_p}$.

These effects have been calculated by several methods (see for example, [16, 17, 7]). Fig. 5.2 represents one such calculation [17]. The figure shows a plot of the correction

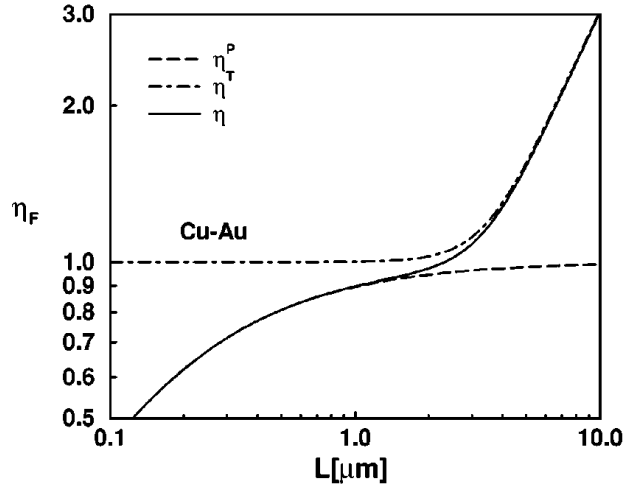

Fig. 1.3: Force correction factors as defined by Eqns. 1.8, 1.9 and 1.10 are plotted as a function of spacing between plates at a temperature of 300° K (from, [17]).

factors estimated using,

$$\eta^T = \frac{F_c^T(d)}{F_c(d)} \tag{1.8}$$

$$\eta^p = \frac{F_c^p(d)}{F_c(d)} \tag{1.9}$$

$$\eta = \eta^T \eta^p \tag{1.10}$$

Thus η^T and η^p are the estimates of the thermal and the conductivity effects respectively. η is the combined corrections. As is clear from Fig. 5.2, the thermal effects and finite reflectivity of the metals are significant at quite different distance scales. At the sub-micron distances, the finite temperature effects are negligible, while the conductivity effects are considerable. Above a few microns the reflectivity effects are small as compared to the appreciable thermal effects. Thus, to study the effects due to finite temperature on the Casimir force, experiments need to be performed in the distance range of a few microns.

1.2 Historical Review of Experimental Status

Experiments to detect forces between flat plates have been attempted since the 17^{th} century [17]. These early experiments were aimed at studying the existence or non-

existence of the physical "vacuum". They studied the adhesion forces between two plates in 'evacuated' containers. In the 20^{th} century, with the emergence of theories concerning long-range, London - van der Waals interactions and Casimir force, renewed experiments were carried out. (For a review of the experiments until 2001, see [4])

The earliest attempt to measure Casimir force was by Overbeek and Sparnaay [15] in 1952. They tried to measure the force between two parallel polished flat glass plates with a surface area of 1 cm^2, in the distance range of 0.6 μm to 1.5 μm. The measurements at 1.2 μm, 'pointed to the existence of a force which was of the expected order of magnitude' [17].

Derjaguin and Abrikossova [8, 7] were the first to obtain results in the distance range 0.1 μm - 1.0 μm that were in agreement with Lifshitz's theory. Sparnaay [16] repeated his measurements with metal plates in 1957. He measured the force between chromium plates and chromium-steel plates. The measurements did not 'contradict' the expected force per unit area from Casimir's relation.

The next major set of improved measurements with metallic surfaces were performed by van Blokland and Overbeek [18] nearly 20 years later, in 1978. They measured the forces between a lens and a flat plate coated with chromium using a spring balance at distances between 0.13 μm and 0.67 μm. This measurement can be considered as the first unambiguous demonstration of the Casimir force between metallic surfaces.

In the last decade, attempts to understand the nature of quantum fluctuations at macroscopic scales and predictions of new long range forces at the sub-millimeter scales by theories that unify the fundamental forces have rekindled interest in Casimir force measurements. The earliest of these was by Lamoreaux in 1997 [24], who measured the Casimir force between a lens and a plate using a torsion balance in the range

0.6 μm - 6 μm. In a later experiment, Mohideen *et al.* [14] measured the Casimir force for separations from 0.1 μm to 0.9 μm using an atomic force microscope. Experiments at Bell-Labs by Chan *et al.* [4] indicate that Casimir type forces play an important role in micro-electromechanical systems. Recently Bressi *et al.* [2] have carried out high precision experiments between parallel plates in the range 0.5 μm - 3 μm and the related force coefficient was determined at the 15% precision level. The most recent experiment by Decaa *et. al.* measures the Casimir force between two dissimilar metals for separations of 0.2 μm - 2 μm.

A more detailed review and a discussion of data from the recent experiments on Casimir force will be presented in a later chapter. All the experiments performed so far to measure Casimir force were carried out at room temperatures and probed the distance range of 0.1 μm to 3 μm. As the separation increases, the force decreases rapidly as d^{-4} to start with and as d^{-3} in the finite temperature regime [Eqn. 1.5]. It is important to measure the force at $d > 3$ μm to detect and characterize the finite temperature corrections to the Casimir force.

1.3 Motivations to study Casimir force

Historically Casimir derived his results while attempting to explain the inter-molecular interactions seen in experiments on colloidal suspensions. Casimir force was looked upon as the effect of finite speed of light (retardation effect) on the London - van der Waals interaction. The early experiments that measured the force of attraction between surfaces where aimed at understanding the inter atom interactions and to see the change over from the van der Waals force at very small separations to the retarded van der Waals or Casimir force as the separations increased. The interest slowly waned once the macroscopic theories of interactions were verified by experiments.

In modern times, interest in Casimir force has been aroused by the crucial role it plays

in theories of fundamental physics. Casimir force provides explicit evidence for the existence of vacuum fluctuations and for the interplay between the microscopic (quantum) and the macroscopic worlds. Also, in the last couple of decades, several new theories have been proposed that predict new physics in the sub-millimeter distance range. Casimir force is the dominant background in this range and hence it becomes essential to understand all aspects of Casimir force before looking for new forces at these scales.

1.3.1 Understanding the Quantum Vacuum

The existences of electromagnetic field fluctuations in vacuum presents problems due to the amount of energy it carries. General Relativity states that all forms of matter and energy should gravitate. The large energy density, ρ_v associated with the vacuum fluctuations should induce very large gravitational effects, much larger than that allowed by observations. This "vacuum catastrophe" is related to the famous cosmological constant problem (see [51, 52, 44, 40] for a review).

In 1917, when Einstein first attempted to apply his new theory to relativity to the Universe, the Universe was believed to be static. Einstein could not construct a static universe if there was only matter and curvature, so he introduced a free parameter Λ, the cosmological constant, into his theory which was a form of energy with negative pressure. With the discovery of the expansion of the Universe, Einstein suggested that this could be dropped. But it was retained alive in discussions of cosmology, and has been used time and again to explain observations that did not fit into the standard scenarios in cosmology [10, 48]. Currently, there is strong observational evidence [43, 41] for an accelerated expansion of the Universe. This can be explained by a non-vanishing cosmological constant. Thus, in the present scenario, the geometry of the Universe is determined by the energy density of matter, ρ_m, the energy density due to vacuum, ρ_v and that from the cosmological constant, $\Lambda/(8\pi G)$. The quantum vacuum has properties similar to those attributed to a positive cosmological constant,

the most important property being an effective repulsive gravity. This is because the acceleration is proportional, in General Relativity, to the term $-(\rho + 3p)$ of the matter, where ρ is the energy density and p the pressure. For normal matter, the term $(\rho + 3p)$ is positive and therefore, the universe is expected to decelerate as it expands. The diagonal elements of the energy momentum tensor are energy density and the three components of pressure. Therefore, an energy momentum tensor that is proportional to "vacuum" with diagonal elements $(1, -1, -1, -1)$ will have its equation of state $\rho = -p$, and the effective acceleration of the Universe with such a source term will be positive. It is this property that allowed Einstein to construct a static Universe, balancing the gravitational attraction of normal matter with the effective repulsion of the cosmological constant. The total energy density in the Universe, ρ_c can be determined from the expansion rate of the Universe and is given by $3H_0^2/(8\pi G)$, where H_0 is the Hubble constant. Cosmological data indicates that $\rho_v = 0.7\ \rho_c\ \sim 4$ keV/cm^3. A naive estimate of ρ_v calculated for all modes of the zero point field with a high frequency cut-off at the Planck scale is 120 orders of magnitude larger than ρ_c. Therefore, there is a need to find a fine-tuned suppression mechanism that will bring this large number close to zero. If a small vacuum energy as well as a cosmological constant are present, then their values need to be fine tuned to the small number ρ_c, which amounts to a fine cancelation to 120 decimal places. This bizarre coincidence is the present cosmological constant problem. To find a solution to this problem, the contributions from the vacuum fields have to be understood and estimated better. Since Casimir force is a direct manifestation of the vacuum fluctuations, it provides a tool to comprehend the 'vacuum'.

1.3.2 "The Hierarchy Problem"

Interactions in nature have been identified to be of four fundamental type: gravitational, electromagnetic, strong and weak. General Theory of relativity and Standard Model of particles physics are the two most successful theories that explain these interactions. Attempts to link these two theories are plagued with difficulties due to the

vast differences in the strength of gravity as compared to others. The Standard Model of electroweak and strong interactions unifies electromagnetic and weak interactions at the characteristic energy scale, M_{ew} of 10^3 GeV (= 1 TeV). The energy scale of gravity is the Planck energy, M_{pl} (= 10^{19} GeV), where the Compton wavelength of a particle becomes equal to its Schwarzchild radius. In natural units ($\hbar = c = 1$), the gravitational constant $G = 1/M_{pl}^2$. The vast difference between these two energy scales is the "hierarchy problem". Several frameworks have been put forward to solve this problem. The most popular among them are string theories, M-theory and theories with large extra dimensions (see [1] for a recent review).

Large extra dimensions and Warped geometries

A model that attempts to reconcile gravity and quantum theory is one in which the fundamental objects that constitute our Universe are not particles but very tiny extended objects: strings. However, to have a consistent string theory that can explain all known phenomena, spatial dimensions larger than 3 are required (for a review, see [42, 4, 1]). The question then is, why do we not see these additional dimensions?

Two scenarios have been proposed to explain this. One that follows the original idea by Kaluza [32], which tries to unify the fundamental forces at Planck scale. In this picture, besides the three spatial dimensions of infinite extent, there are additional dimensions of finite size, r_c, that are curled up as compactified circular extra dimensions. The typical size of the circle would be determined by the Planck length, 10^{-33}cm. This means that physics at short distances appears to be higher dimensional and forces go as $1/r^{-(n+2)}$, where n is the number of extra dimensions. At distances much larger than r_c, $n = 0$ and one observes the $1/r^2$ law. Around the compatification scale, the forces can be modelled as e^{-r/r_c} and would show up as deviations from the standard law.

The other idea proposed by Arkani-Hamed and others [5, 3] , tries to unify forces at

the TeV scale, thereby removing the hierarchy problem. The 10^{32} times weakness of gravity as compared to the other forces at this electroweak scale is explained by the presence of the extra-dimensions of finite size R_*. They propose that the three spatial dimensions in which we live are perhaps just a membrane (3-brane) embedded in a higher dimensional bulk of $(3+n)$ spatial dimensions. The Standard Model fields are confined to the 3-brane while gravity can propagate into the bulk. Thus, at distances greater than R_*, gravity spreads in all $3+n$ dimensions and goes as $1/r^{-(n+2)}$ while the strength of the other forces, still falls as $1/r^2$. At $r > R_*$, gravity too reverts back to $1/r^2$. This scenario is distinguished by the term, "large extra dimensions scenario", as the additional dimensions in this theory could even be macroscopic. If there were only one extra dimension, its size would have to be of the order of 10^{10} km to account for the weakness of gravity. Such an extra dimension would change the dynamics of the Solar system and is eliminated by known experimental results. With two equal extra dimensions, the scale length would be of the order of a 0.3 mm. This is inconsistent with laboratory experiments [22] and astrophysical bounds [2, 12, 20, 21]. For $n \geq 3$, the scale length is less than about a nanometer. This does not imply that the new dimensions will not show observable effects in experiments at sub-millimeter scales. A single large dimension of size 1 mm with several much smaller extra dimensions is still allowed. Experiments have shown that the scale length of the 'largest' extra dimension has to be < 200 μm [22, 1]. This would give rise to observable changes to inverse square law of gravity at these scales. At such distances, the strengths of gravity and Casimir forces are comparable and in order to look for new corrections to inverse square law of gravity, Casimir background has to be first understood and eliminated.

New particles

The super-symmetric extensions to standard model unify the electro-weak and strong interactions at energy scales of 10^{16} GeV, which is very close to the Planck scale,

with the additional assumption that there are no charged particles between the TeV and the Planck scale (see for ex. [4, 42] and references therein). A trade mark of super-string theories is the occurrence of scalar partners of the graviton (dilaton), gravitationally coupled massless scalers called moduli, and other light scalers like axions. The exchange of these particles could give rise to Yukawa type interactions, that would appear in experiments that measure forces. The range λ, of these interactions depends on the mass of the elementary particle. For super-symmetric theories with low energy (few TeV) symmetry breaking, these scalar particles would produce effects in the sub-millimeter scales [23, 30]. The predictions on the strength of these effects is less precise than those of the extra-dimension scenarios.

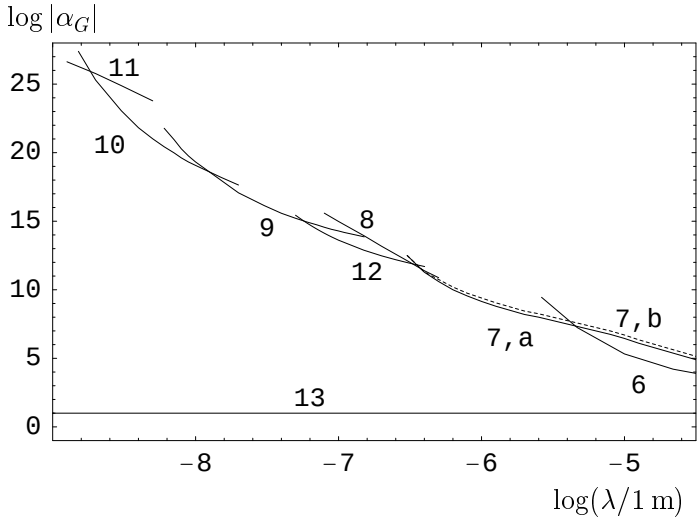

Fig. 1.4: Plot of the constraints on the Yukawa interaction parameter α from various ranges of λ reproduced from [26]. Curves 7-10, 12 follow from Casimir force measurements, Curve 11 from van der Waals force measurements. Curve 6 is from an experiment that measured deviations from Newton's law of gravity [25]. The typical prediction of extra dimensional physics is shown in Curve 13. The region in the (α, λ) plane above each curve is excluded and the region below each curve is allowed.

1.3.3 Constraints on new macroscopic forces

Keeping in mind that the strengths of the new macroscopic forces are small, their potentials are scaled with respect to the gravitational interaction between two point masses as shown below:

$$V(r) = -\frac{GM_1M_2}{r}\left(1 + \alpha e^{-\frac{r}{\lambda}}\right) \tag{1.11}$$

where α represents the coupling strength of the interaction and λ the range [23, 27]. The typical scale of λ will vary depending on the source of the potential. For the extra dimension scenarios it would be the size of the extra dimension, while for the new string inspired forces, it would be proportional to the inverse of the mass of the mediating particle. Thus constraints can be placed on the parameter space of $\alpha - \lambda$ from experiments that study long-range interactions [5]-[11]. For distances of $\lesssim 0.1$ mm, Casimir force provides the dominant background and best limits on α for these λ can be obtained from Casimir force measurements. The available constraints to date on $\alpha - \lambda$ from various experiments are summarised in Fig.1.4.

The torsion balance experiments described in this thesis are capable of strongly constraining theories with macroscopic extra dimensions, apart from measuring the Casimir force and its finite temperature corrections.

References

[1] E. G. Adelberger. Sub-millimeter Tests of the Gravitational Inverse Square Law. *http://arXiv.org/abs*, hep-ex/0202008, 2002.

[2] E. G. Adelberger, Heckel, and Nelson A. E. B. R. Tests of the Gravitational Inverse sqare law. *Ann. Rev. of Nuclear and Particle Science*, 53:77, December 2003.

[3] I. Antoniadis, N. Arkani-Hamed, S. Dimopoulos, and G. Dvali. New Dimension at a Millimeter to a Fermi and Superstrings at a TeV. *Phys. Lett. B*, 436:257, 1998.

[4] N. Arkani-Hamed. Large Extra Dimensions: A new Arena for Particle Physics. *Physics Today*, page 35, Feb. 2002.

[5] N. Arkani-Hamed, S. Dimopoulos, and G. Dvali. The Hierarchy Problem and New Dimension at a Millimeter. *Phys. Lett. B*, 429:268, 1998.

[6] N. Arkani-Hamed, S. Dimopoulos, and G. Dvali. Phenomenology, astrophysics, and cosmology of theories with submillimeter dimensions and TeV scale quantum gravity. *Phys. Rev. D*, 59:086004, April 1999.

[7] M. Bordag, B. Geyer, G. L. Klimchitskaya, and V. M. Mostepanenko. Casimir Force at Both Nonzero Temperature and Finite Conductivity. *Physical Review Letters*, 85:503–506, July 2000.

[8] M. Bordag, U. Mohideen, and V. M. Mostepanenko. New Developements in Casimir Force. *Phys. Rep.*, 353:1, 2001.

[9] G. Bressi et al. Measurement of the Casimir Force between Parallel Metallic Surfaces. *Phys. Rev. Lett*, 88:041804–1, 2002.

[10] R. R Caldwell and P J Steinhardt. Quintessence. *Physics Worlds*, page 31, Nov 2000.

[11] H. B. Casimir. On the Attraction Between Two Perfectly Conducting Plates. *Proc. K. Ned. Akad. Wet.*, 51:793, 1948.

[12] H. B. Chan et al. Quantum Mechanical Actuation of Micromechanical Systems by the Casimir Force. *Science*, 291:9, 2001.

[13] R Cowsik. A new torsion balance for studies in gravitation and cosmology. *Indian Journal of Physics*, 55B:487, 1981.

[14] R Cowsik. Challenges in experimental gravitation and cosmology. Technical report, Dept. of Science & Technology, New Delhi, 1982.

[15] R Cowsik. Search for new forces in nature. In *From Mantle to Meteorites (Prof. D.Lal Festschrift)*, 1990.

[16] R. Cowsik, N. Krishnan, P. Sarawat, S. N Tandon, and S. Unnikrishnan. The Fifth Force Experiment at the TIFR. In *Gravitational Measurements, Fundamental Metrology and Constants*, 1988.

[17] R. Cowsik, N. Krishnan, P. Sarawat, S. N Tandon, and S. Unnikrishnan. Limits on the strength of the fifth-force. In *Advances in Space Research (Proc. XXI COSPAR, Espoo)*, 1989.

[18] R. Cowsik, N. Krishnan, S. N. Tandon, and C. S. Unnikrishnan. Limit on the strength of intermediate-range forces coupling to isospin. *Physical Review Letters*, 61:2179–2181, November 1988.

[19] R. Cowsik, S. N Tandon, and N. Krishnan. Sensitive test of Equivalence Principle. Technical report, Dept. of Science & Technology, New Delhi, 1982.

[20] S. Cullen and M. Perelstein. SN 1987A Constraints on Large Compact Dimensions. *Physical Review Letters*, 83:268–271, July 1999.

[21] B. V Derjaguin. The Force Between Molecules. *Sci. Am.*, 203:47, 1960.

[22] B. V Derjaguin and J. J. Abrikossova. *Disc. Faraday Soc.*, 18:33, 1954.

[23] S. Dimopoulos and G. F. Giudice. Macroscopic Forces from Supersymmetry. *Phys. Lett. B*, 379:105, 1996.

[24] C. Genet. *La Force de Casimir Entre Deux Miroirs Metalliques À témperature Non Nulle*. PhD thesis, Laboratoire Kastler Brossel, University of Paris, Paris, Italy, 1999.

[25] C. Genet, A. Lambrecht, and S. Reynaud. Temperature dependence of the Casimir effect between metallic mirrors. *Phy.Rev. A*, 62:012110, July 2000.

[26] C. Hanhart, D. R. Phillips, S. Reddy, and M. Savage. Extra dimensions, SN1987a, and nucleon-nucleon scattering data. *Nuclear Physics B*, 595:335–359, February 2001.

[27] C. Hanhart, J. A. Pons, D. R. Phillips, and S. Reddy. The likelihood of GODs' existence: improving the SN 1987a constraint on the size of large compact dimensions. *Physics Letters B*, 509:1–2, June 2001.

[28] C. D. Hoyle, U. Schmidt, B. R. Heckel, E. G. Adelberger, J. H. Gundlach, D. J. Kapner, and H. E. Swanson. Submillimeter Test of the Gravitational Inverse-Square Law: A Search for "Large" Extra Dimensions. *Physical Review Letters*, 86:1418–1421, February 2001.

[29] M. Jaekel, A. Lambrecht, and S. Reynaud. Quantum vacuum, inertia and gravitation. *New Astronomy Review*, 46:727–739, November 2002.

[30] D. B. Kaplan and M. B. Wise. Coupling of the light Dialoton and Violations of the Equivalance Principle. *J. High Energy Phys.*, 08:37, 2000.

[31] N. Krishnan. *Search for Intermidiate Range forces Weaker than Gravity.* PhD thesis, Tata Institute of Fundamental Research, Mumbai, India, 1989.

[32] T. Kulza. *Preuss. Akad. Wiss.*, page 966, 1921.

[33] S. K. Lamoreaux. Demonstration of the Casimir Force in the 0.6 to 6 μ Range. *Phys. Rev. Lett*, 78:5, 1997.

[34] E. M. Lifshitz. Theory of molecular attraction between solids. *Sov. Phys. JETP*, 2:73, 1956.

[35] J. C. Long et al. Upper Limit on Submillimeter-range Forces from Extra Spacetime dimensions. *Nature*, 421:924, 2003.

[36] W. P Milonni. *The Quantum Vacuum: An Introduction to Quantum Electrodynamics.* Academic Press, Newyork, 1994.

[37] U. Mohideen and A Roy. Precision Measurement of the Casimir Force from 0.1 to 0.9 μm Range. *Phys. Rev. Lett*, 81:4549, 1998.

[38] V. M. Mostepanenko. Constraints on Non-Newtonian Gravity from Recent Casimir Force Measurements. *ArXiv General Relativity and Quantum Cosmology e-prints*, November 2003.

[39] J. T. G. Overbeek and M. J. Sparnaay. *Proc. K. Ned. Akad. Wet.*, 54:387, 1952.

[40] T. Padmanabhan. Cosmological constant-the weight of the vacuum. *Phys. Rep.*, 380:235–320, July 2003.

[41] S. Perlmutter et al. Measurements of Omega and Lambda from 42 High-Redshift Supernovae. *Astrophys. J*, 517:565–586, June 1999.

[42] L. Randall. Extra Dimensions and Warped Geometries. *Science*, 296:1422, 2002.

[43] A. G. Riess et al. Observational Evidence from Supernovae for an Accelerating Universe and a Cosmological Constant. *Astron. J*, 116:1009–1038, September 1998.

[44] V. Sahni. The cosmological constant problem and quintessence. *Classical and Quantum Gravity*, 19:3435–3448, July 2002.

[45] J. Schwinger, L. L. DeRaad, Jr., and K. A. Milton. Casimir Effect in Dielectrics. *Ann. Phys. NY*, 115:1, 1978.

[46] M. J. Sparnaay. Attractive Forces Between Flat Plates. *Nature*, 180:334, 1957.

[47] M. J. Sparnaay. Historical Background of Casimir force. In A. Sarlemijn and M. J. Sparnaay, editors, *Physics in the Making*, North-Holland, 1989. Elsevier Science Publishers B V.

[48] N. Straumann. The History of the Cosmological COnstant Problem. *ArXiv General Relativity and Quantum Cosmology e-prints*, August 2008.

[49] C. S. Unnikrishnan. *Torsion Balance Experiments to Search for New Composition Dependant Forces*. PhD thesis, Tata Institute of Fundamental Research, Mumbai, India, 1992.

[50] P. H. G. M van Blokland and J. T. G. Overbeek. van der Waals Forces Between Objects Covered with Chromium Layer. *J. Chem. Soc. Faraday Trans. 72*, 72:2637, 1978.

[51] S. Weinberg. The cosmological constant problem. *Reviews of Modern Physics*, 61:1–23, January 1989.

[52] S. Weinberg. The Cosmological Constant Problems. In *Sources and Detection of Dark Matter and Dark Energy in the Universe*, page 18, 2001.

2. TORSION BALANCE- DESIGN AND FABRICATION

Abstract: This chapter is devoted to the description of the main components of the experimental set up. An overview of the experimental scheme will be followed by a detailed explanation of the various components of the experiment. The procedures followed during assembly to reduce systematic and environmental noises will be described.

2.1 General principle of the apparatus

Torsion pendulums have been used as transducers for precision measurements for over two centuries. They are known for their capability to isolate and measure feeble effects that would otherwise be difficult if not impossible to observe against the background gravitational field of the earth.(see for ex., [3, 1]) Our experimental set up is aimed at achieving the sensitivity required to measure the finite temperature effect in the Casimir force using a torsion pendulum, optical auto-collimator combination. [2, 4]. The experiment was to be performed in the separation range 2 μm - 10 μm. Casimir force at 10 μm will produce, in static case, a deflection of $\sim 10^{-6}$ radians on our pendulum. This is well with in the sensitivity of $\sim 10^{-8}$ radians of our optical lever.

The measurement scheme [Fig. 2.1] broadly consists of a torsional pendulum with a flat circular disc, P , as mass element, suspended using a thin strip fibre. The source

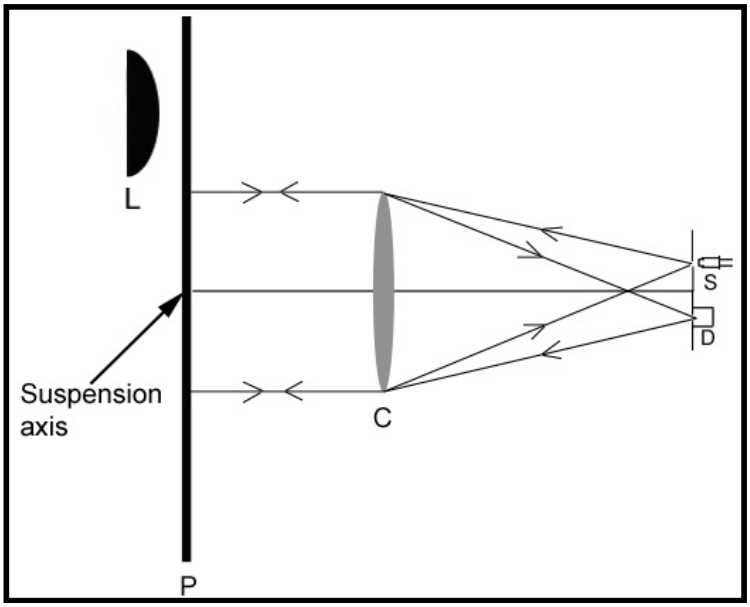

Fig. 2.1: Figure representing the measurement scheme. L = spherical surface, P = pendulum disc, C = collimating lens, S = source of light, D = Light Detector

of the force field we wish to study is provided by a spherical surface, L , located close to one edge of the suspended disc. The torque on the pendulum due to this force is inferred from the deflection of the pendulum measured using an auto-collimating optical lever.

2.2 Torsion Pendulum

2.2.1 Mass Element

The mass element of the torsion pendulum has two parts. A circular disc and a mechanism to attach the disc to the suspension. The mass element assembly weighs a total of 52 grams and has a moment of inertia of ~ 198 g.cm^2

The Disc:

The active element of the suspension is a circular disc of thickness 4 mm and diameter 80 mm made of glass. The edges of the disc are chamfered and both the faces are polished to have a surface finish of $\lambda/2$ and are coated with a 1 μm thick layer of gold. One of the faces acts as a conducting boundary for the force under study and the other face acts as a mirror viewed by a sensitive optical lever which measures the angle that the normal to the disc makes with the optic axis of the optical lever.

The Disc holder:

The gold coated glass disc is held in a frame made of a gold strip that is 80 μm thick and 4 mm wide. In order to hold the glass disc firmly, this strip is shaped to form a groove that matches the chamfered edges of the disc and forms a circular frame around the disc. The ends of this strip are held securely between the flat surfaces of an Aluminium holder [Fig. 2.2]. The flat surfaces that press the strip ends together have 50 μm deep, 4mm wide channels machined with the central axis of the channel along the axis of the holder. These locate the strip and hence the pendulum bob along the axis of the holder. The top of this holder has a 2 mm diameter hole through its central axis to hold the torsional fibre. This holder is also gold coated to avoid aluminium oxide layers that can accumulate charges.

2.2.2 The Pendulum Suspension

The mass element is suspended in two stages to avoid non-torsional modes of oscillation of the pendulum. The suspension consists of a pre-suspension, a device to damp the simple pendular modes of the fibre, and the main suspension.

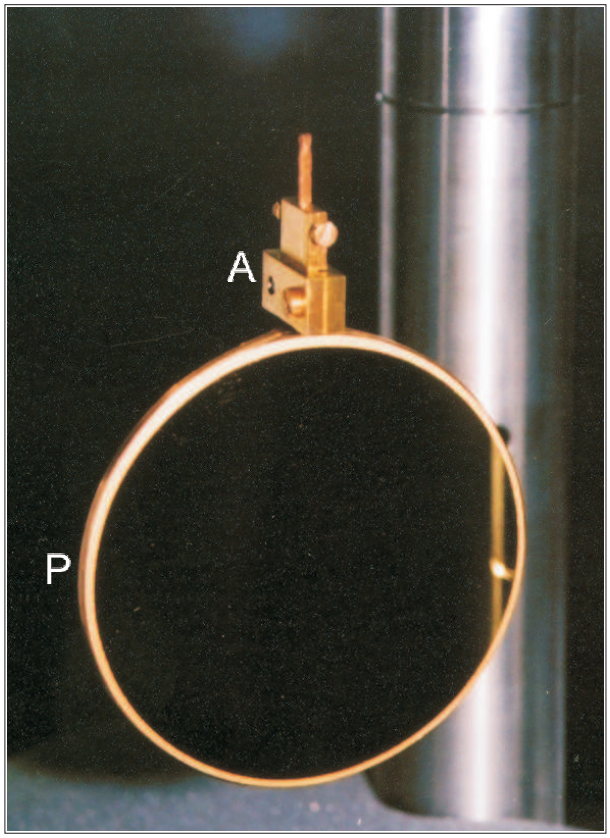

Fig. 2.2: Picture of Mass element assembly. A = Aluminium holder, P = Pendulum Disc

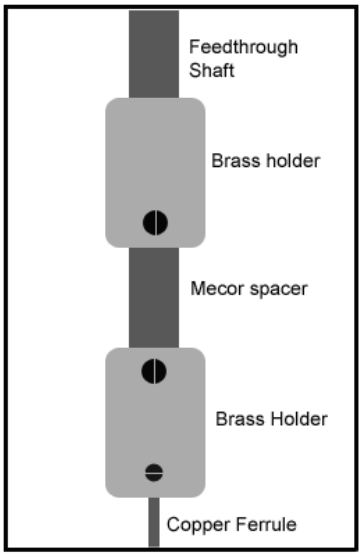

Fig. 2.3: A schematic of the pre-suspension mount

Pre-suspension:

The first portion of the suspension is a torsionally stiff copper wire of 100 μm diameter. This ensures verticality of the main suspension that uses a metal ribbon. The pre-suspension is essential to avoid spurious torsional effects due to tilts of the suspensions. The ends of the stiff wire are passed through a copper ferrule of outer diameter 2 mm and bore diameter of about 0.5 mm. The ferrule is crimped such that it holds the fibre gently but firmly along its central axis. The length of the Copper wire is 7 cm between the ferrules. The wire is mounted from the shaft of a rotary feed-through that is attached to the top of the vacuum chamber housing the experiment. To electrically isolate the suspension from the chamber, the wire is held through a Macor insulator as described below [Fig. 2.3]. The shaft holds a cylindrical clamp made of brass, which in turn holds a Macor cylinder. Another cylindrical brass holder is mounted to this Macor piece and has a 2 mm diameter hole along its axis. The ferrule at one end of the wire is passed through this hole and held in place by a screw. A copper disc is suspended from the ferrule at the other end of the wire using a similar mechanism [Fig. 2.4]. Kapton insulated copper wires connect the fibre suspension to an electrical feed-through mounted on the vacuum chamber.

Pendular Mode Damper:

The copper disc (C) passes between the pole pieces of an aluminium-nickel-cobalt ring magnets (M) [Fig. 2.4] such that it cuts across the field lines (B) of the magnet. The fast pendular oscillations of the fibre and violin modes cause eddy currents to flow in the copper disc and dissipate these modes. Thus, these modes will be damped out rapidly. Since the copper disc and the magnet are axially symmetric, the very slow torsional modes are not damped.

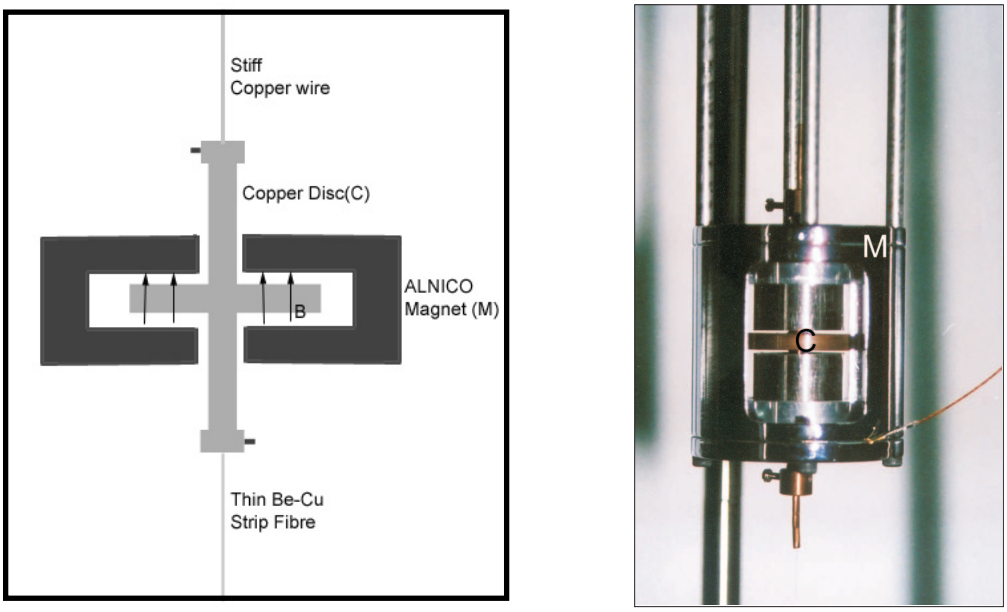

(a) (b)

Fig. 2.4: The pendular mode damper assembly: (a)Shows the general scheme and (b) shows a photograph of the assembly

The Torsional Fibre:

The main torsional element is a Beryllium-Copper strip fibre of width = 90 μm, thickness = 9 μm and length = 39 cm. The breaking strength of the fibre is approximately 100 g. Thus our load of 52 g is well within its breaking strength. Copper ferrules are crimped at either end of this fibre as in the case of the torsionally stiff copper wire. The fibre is anchored to the copper disc on the top and holds the active mass element at the bottom. The fibre is pre-annealed under a load of 50 g at a temperature of about 150° C for a day.

The torsion constant of the suspension $k_f \approx 0.05$ dyne cm rad^{-1} and the suspension has a time period of $\sim$ 406 sec. The thermal amplitude of the suspension in the absence of external disturbances is $\sim 9 \times 10^{-7}$ radians at room temperature of $\sim$ 300° K.

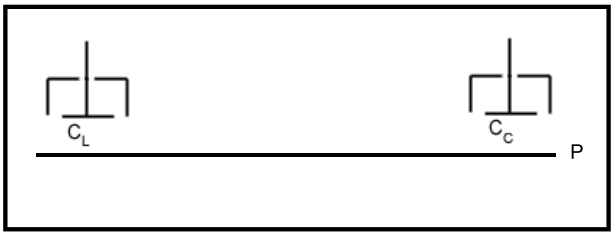

Fig. 2.5: The capacitance arrangement for damping torsional modes

2.3 The Capacitor Plates and Torsion Mode Damping

The torsional oscillations of the pendulum can be damped to an amplitude of about 10^{-5} radians by applying capacitive forces to the suspended disc. Two capacitor plates are mounted such that they produce opposing torque on the disc. The net torque due to the capacitances is varied by adjusting the individual voltages on them. A schematic of the arrangement is shown in Fig. 2.5. A voltage applied to C_L rotates the pendulum, P clockwise as seen from above while a voltage on C_C rotates it anticlockwise. By switching the voltages exactly out of phase with the torsional oscillations of the pendulum, these oscillations are damped.

The capacitor plates are made of aluminium and consist of circular plates of 1.2 cm diameter that are placed within grounded guard rings. The guard ring is insulated from the plate with Macor positioners. The two sets of capacitor plates are mounted together on another Aluminium fixture such that they are on diametrically opposite edges of the suspended disc and positioned at about 2 mm separation from the disc. Shielded Kapton insulated copper leads connect the capacitor plates to electrical feedthroughs on the vacuum chamber. The capacitors and the mount are gold coated to avoid exposed Aluminium oxide surfaces.

These capacitors can also be used to perform a null experiment in which the deflection of the torsional pendulum is balanced by capacitive forces. The position signal from

the optical lever is fed back to control the effective voltage on the capacitor plates and the torsion pendulum 'locked' at a fixed position. If the torque on the pendulum due to force between the pendulum and the spherical lens surface is modified, voltage on the capacitors changes to balance this torque. Thus, the change in voltage on the capacitor is a direct signal of the torque acting on the pendulum.

The varying voltages are generated from a 16 bit DAC in a PCI interface card. Typically one volt on the capacitor at 1 mm separation, gives rise to a torque of $\sim 10^{-3}$ dyne.cm. The voltage on one capacitor is kept fixed at about 4 V and that on the other is varied from 0 V - 10 V so that both positive and negative torques may be applied to the pendulum. The information on the angular position of the suspended disc obtained from the autocollimator is fed back to a PID loop through software (Labview) to control the voltage of the capacitor. When the lens is far away and the only force on the suspension is the restoring force from the fibre, the PID loop keeps the position of the pendulum locked to about 1/10 of a pixel or 5×10^{-7} radians (1 sec integration). This is below the thermal amplitude of the pendulum which is of the order of 10^{-6} radians.

2.4 The Spherical Lens and the Compensating Plate

In our experiment the Casimir force between the suspended disc and the spherical surface of a lens is measured. This configuration is simpler to implement as difficulties in holding the 2 plates parallel to each other while measuring the force are avoided. The lens is 25 mm in diameter and has a radius of curvature of about 38 cm. It is coated with 1 μm thick layer of gold. It is mounted in a cell and held along the diameter of the suspended disc close to one edge such that the interactions between the lens and the mass element apply a torque on the pendulum. In this position, the gravity due to the lens cell assembly will also apply a torque on the suspension. This is minimized by using a compensating plate of Aluminium with mass equal to

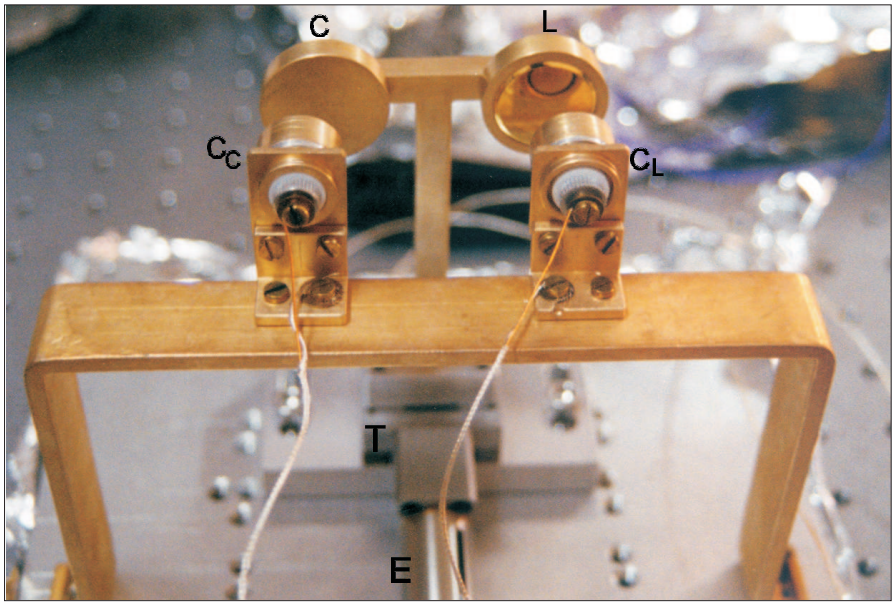

Fig. 2.6: The lens (L), compensating plate (C) and the capacitor plates (C_L and C_c) assembled (without the pendulum). T is the translation stage and E the EncoderMike®

that of lens and the cell [Fig. 2.6]. The outer diameter of the compensating plate is equal to that of the lens cell, but the compensating plate has a flat surface facing the suspended disc and its thickness is adjusted to equalize the masses. The compensating plate is mounted such that the gravitational torque due to the plate opposes the gravity due to the lens assembly. The net gravitational torque on the pendulum is small. More importantly, changes in the force as the lens is moved through small distances is negligible compared to the changes in Casimir force and electrostatics forces. The lens assembly and the compensating plate are together mounted on a translation stage (T) (Newport Model- 461 series)(Fig. 2.6). An EncoderMike® actuator (E) from Oriel is used to translate this stage perpendicular to the disc surface. The actuator movement is controlled by DC voltages applied to it. The encoder has a resolution of 0.05 μm and its output is monitored using a Data acquisition card with a PCI interface attached to the PC.

The lens assembly and the compensating plate are electrically isolated from each other and from the mount. Kapton insulated copper wires connect them to separate

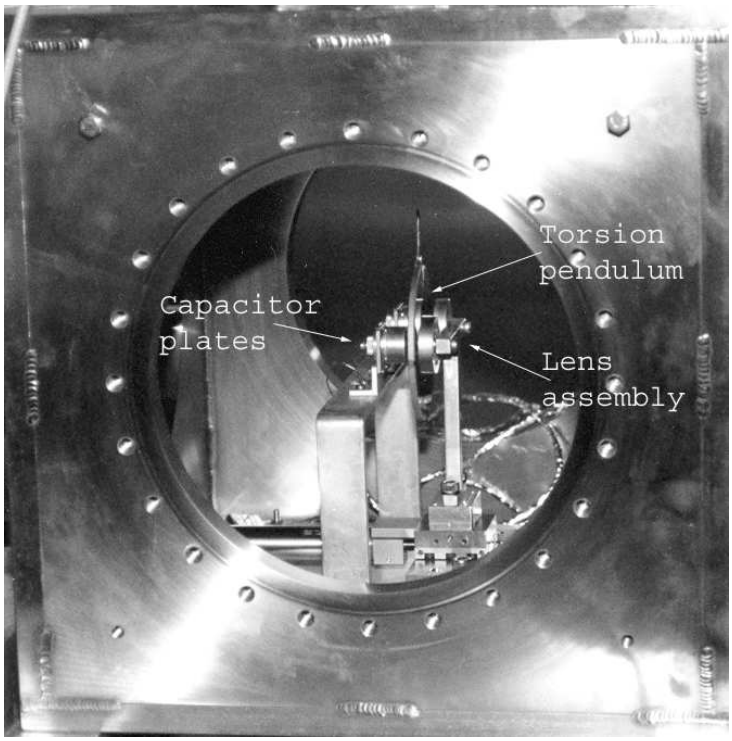

Fig. 2.7: Picture of the torsion pendulum, capacitors and the lens assembled inside the vacuum chamber

connectors on an electrical feed-through attached to the vacuum chamber.

2.5 The Vacuum Chamber

The experiment is conducted in high vacuum ($\sim 4 \times 10^{-8}$ Torr). The presence of gas surrounding the pendulum at pressures above 10^{-6} Torr not only damps its oscillations very quickly, but also produces pressure gradients which lead to erratic, anharmonic deflections of the pendulum. A cubical vacuum chamber with side ports for optical windows with 300 mm long extension tube on its top flange was designed and fabricated. The experimental apparatus are mounted inside this chamber [Fig. 2.7 and Fig. 2.8]. The extension tube is fitted with a rotary feed through at the top, from which the pendulum is suspended. This enables us to rotate the pendulum and change its equilibrium position. The feed through is motorized and has angular resolution of 0.1 degree. The MotorMikes®, translation stages and all other components were

vacuum tested to $\sim 10^{-8}$ Torr individually before assembly into the main vacuum chamber.

The vacuum chamber is initially pumped down to $\sim 10^{-8}$ Torr using a turbo molecular pump from Varian with a pumping speed of 250 litre/s. An ion pump is switched on at this stage. The system is baked at 90° C for 2 days. The turbo pump is then valved shut and switched off. The ion pump remains on through out the experiment and maintains the pressure at 3×10^{-8} Torr without any mechanical disturbances. The pressure inside the vacuum chamber is measured using a compact full range cold cathode gauge from Pfeiffer Vacuum. The ion current read out from the ion pump is also used to monitor the pressure.

For the optical lever to view the mirror suspended inside the vacuum chamber a home made wire sealed optical glass window is used. The window is made of BK7 glass, 25 mm thick and is polished on either side to a surface accuracy of $\lambda/4$. A commercial glass view port typically does not have the optical quality required to get sharply focused image of the source slits of the optical lever on the CCD detector. There are also two other standard glass view ports to see into the chamber. Glass surface being dielectric and insulating, accumulates charges. These charges can create electric fields inside the vacuum chamber that influences the torsional pendulum. To shield these fields grounded wire mesh are mounted inside the vacuum chamber in front of all the glass windows. Without these wire meshes, the pendulum can get 'locked' into position determined by stray electric fields from the view ports.

2.6 The Electrical Wiring and Grounding in the Apparatus

The vacuum chamber is held at ground potential by a thick copper cable. This shields the apparatus inside from electrical pick ups. The pendulum and the compensating plates are externally connected to the same ground point. The capacitor plates and

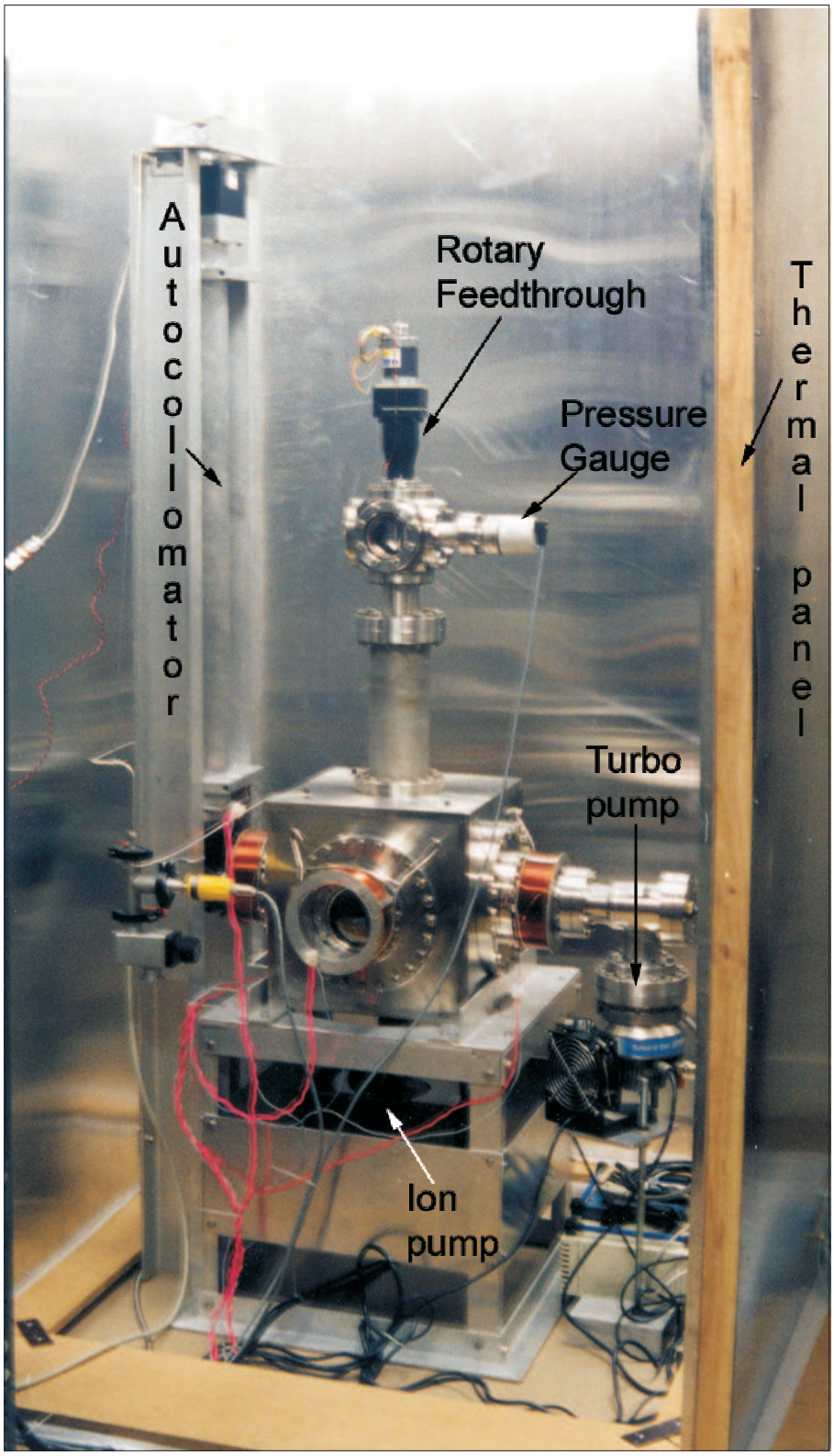

Fig. 2.8: A photograph of the experimental set up during assembly

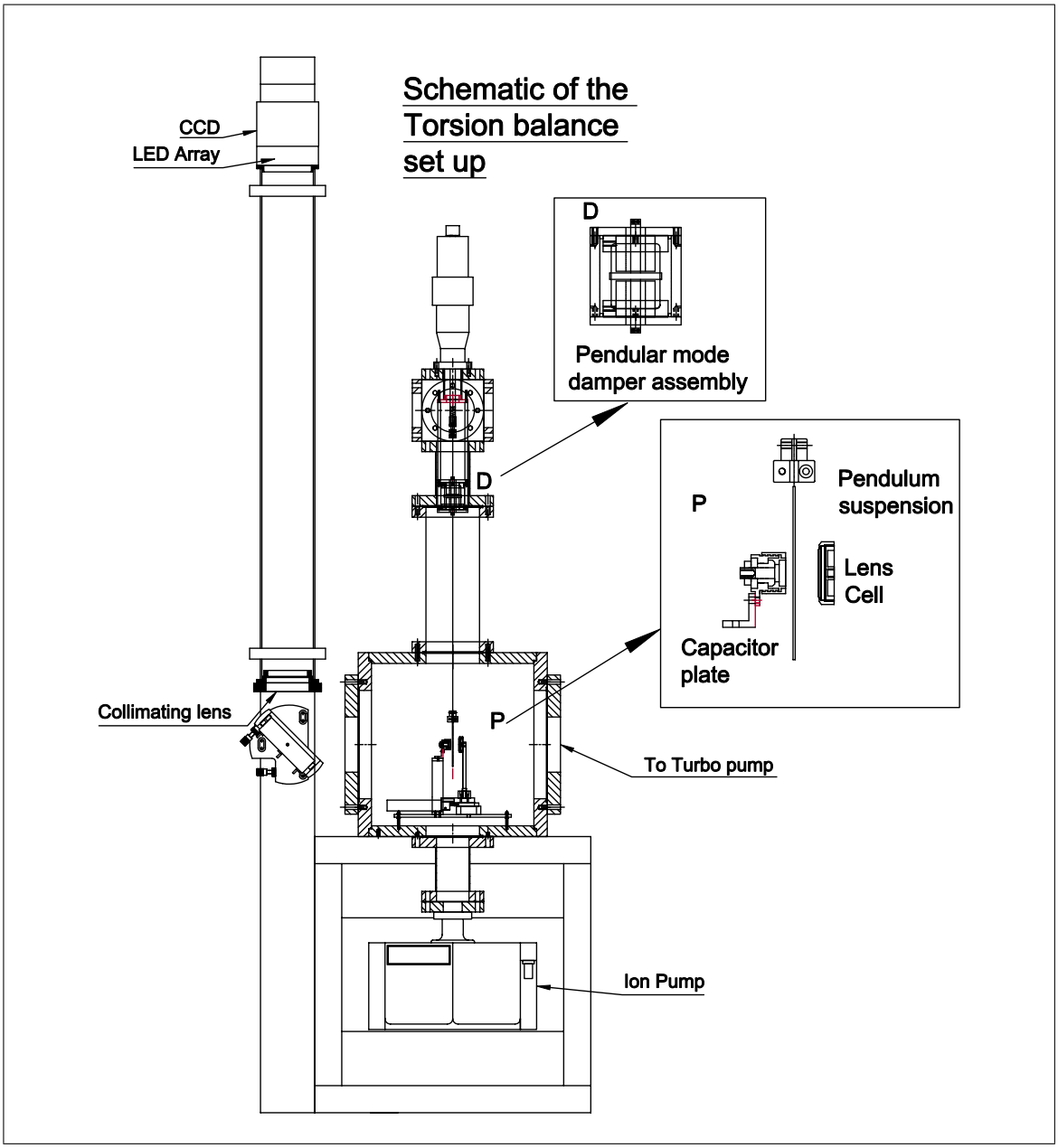

Fig. 2.9: Schematic of the experimental set up

the lens are also connected to this ground point when voltages are not applied on them.

A UV lamp is placed inside the chamber and flashed on during pump down when the pressure in the chamber is dropping from 10 Torr to 1 Torr. This generates lots of electrons (by photoelectric effect) and some ions; thus allowing a neutralization of the electrical charges. The usage of the lamp was 'empirical' and was not very systematic. We found small reduction in the residual electrostatic force when the lamp was operated for short duration during pump down.

2.7 The Thermal Panels

The experimental set up is shielded from fast temperature variations and temperature gradients in the environment. The set up is surrounded by four 1.2×4.2 meter, insulating panels. Each of these panels is made of several layers of thermocol and plywood sheets sandwiched between Aluminium sheets and held together by a wooden frame. The 'walls' formed by these is covered on the top by thermocol layers attached to Aluminium sheet. Various electrical and signal cables come out through tightly packed holes in the shroud. The entire apparatus is placed within a closed room and controlled from outside. The peak to peak variation in temperature inside the enclosure is 1 degree per day (diurnal cycle), while the ambient temperature changes by as much as 10 degree per day. However, fluctuations over time scales of an hour are within 5 millidegree.

References

[1] R Cowsik. Torsion balances and their application to the study of gravitation at Gauribidanur. In *New Challenges in Astrophysics. Special Volume of the IUCAA Dedication Seminar*, 1997.

[2] R. Cowsik, B. P. Das, N. Krishnan, G. Rajalakshmi, D. Suresh, and C. S. Un-

nikrishnan. High Sensitivity Measurement of Casimir Force and Observability of Finite Temperature Effects. In *Proceedings of the Eighth Marcell-Grossmann Meeting on General Relativity*, page 949. World Scientific, 1998.

[3] G. T. Gillies and R. C. Ritter. Torsion balances, torsion pendulums, and related devices. *Review of Scientific Instruments*, 64:283–309, 1993.

[4] C. S. Unnikrishnan. Observability of the Casimir force at macroscopic distances: A proposal. *Unpublished, TIFR Preprint*, G-EXP/95/11, 1995.

3. THE AUTOCOLLIMATING OPTICAL LEVER

Abstract: An optical lever of novel design built to measure the deflection of the torsional pendulum will be described in this chapter. The optical level has a large dynamic range of 10^6 *and a sensitivity of* $\sim 1 \times 10^{-8}$ *radians/*$\sqrt{Hz}$*. The chapter will begin with the discussion of the principle of the design and go on to describe its implementation. Finally the tests and characterization of the autocollimator will be discussed.*

3.1 Conceptual aspects of the design

The angular deflection of the torsion balance contains the signal in our experiment. The method used for its measurement is the standard optical lever arrangement [see for example, [2, 3], [1] and references therein] where a beam of light is reflected off a mirror on the torsional pendulum and the deflection of the light beam is then proportional to the rotation of the pendulum. This basic scheme has been modified to give good accuracy and large dynamic range for angle measurements.

The optical lever is arranged in an auto-collimating configuration. In this configuration, the translation of the mirror does not change the image on the detector and the optical lever is sensitive to only rotations of the mirror. An illuminated array of slits, S , is placed in the focal plane of an achromatic lens, C , with a slight offset with respect to its optical axis. The collimated beam emerging from the lens falls on the mirror, M , whose rotation angle is to be measured. The reflected beam from the

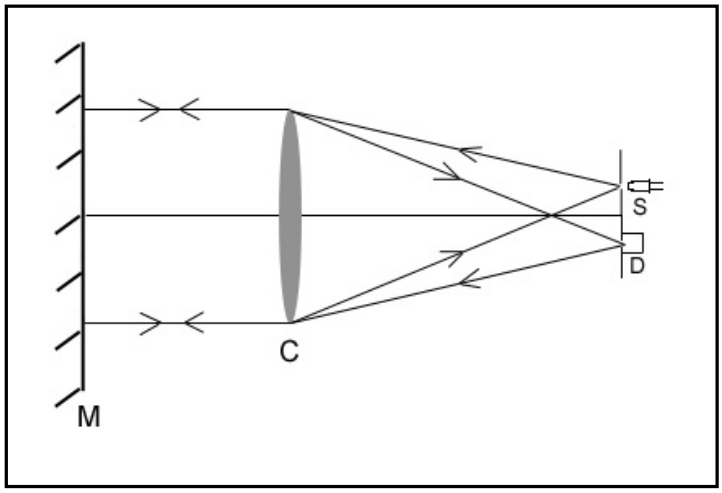

Fig. 3.1: Classical autocollimating arrangement

mirror returns through lens and will form an image of the slit very close to the slit itself, but with an opposite offset with respect to the optical axis. This image falls on a linear array CCD detector, D. The location of the centroid of the image on the CCD is a measure of the angle between the optic axis and the normal to the mirror. In the conventional optical lever, a single slit is imaged on to a photodetector or a position sensitive photodiode. The resolution of the device improves roughly as the inverse of the square root of intensity of light detected and using a multi-slit scheme can increase the sensitivity significantly compared to the single slit scheme. The use of the linear CCD array allows measurement of deflections over much larger range of angles than what is possible in a conventional optical lever.

Let $i(x)$ represent the number density of the photons counted as a function of their location x. For considerations of the design let $i(x)$ be a simple box shaped distribution as shown in Fig. 3.2.

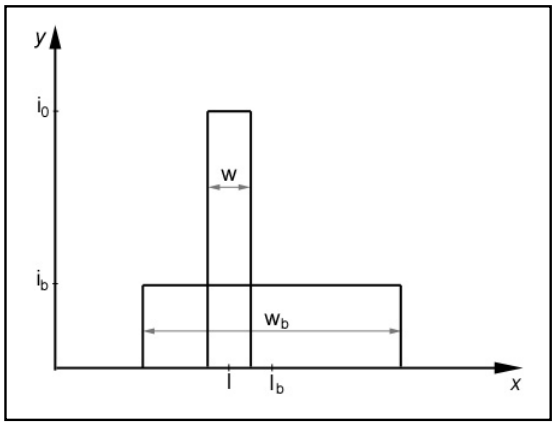

Fig. 3.2: Distribution $i(x)$

The moment, m of the distribution $i(x)$, say about $x = 0$ is simply given by

$$\begin{aligned} m &= \int_{-\infty}^{\infty} i(x) \cdot (x-0)dx; \\ &= i_0 \frac{x^2}{2}\Big|_{l-\frac{w}{2}}^{l+\frac{w}{2}}; \\ &= i_0 l w. \end{aligned} \tag{3.1}$$

The fluctuation in m is given by,

$$\begin{aligned} (\Delta m)^2 &\approx \int i(x)\ x^2\ dx; \\ &= i_0 \frac{x^3}{3}\Big|_{l-\frac{w}{2}}^{l+\frac{w}{2}}; \\ &= \frac{i_0}{3}(3l^2 w + \frac{w^3}{4}). \end{aligned} \tag{3.2}$$

Thus, the centroid of the image is obtained by dividing the moment by the total number of recorded photons $I_0 = i_0 w$

$$x_c = \frac{m \pm \Delta m}{i_0 w} = l \pm \sqrt{\frac{1}{I_0}(l^2 + \frac{w^2}{12})}. \tag{3.3}$$

Now consider the presence of a background light which generates counts $i_b(x)$ spread over a width $w_b > w$ about some location l_b. This will combine with the image and

generate a new centroid given by

$$x_b = \frac{I_0 l + I_b l_b}{I_0 + I_b} \pm \sqrt{\frac{I_0}{(I_0 + I_b)^2}(l^2 + \frac{w^2}{12}) + \frac{I_b}{(I_0 + I_b)^2}(l_b^2 + \frac{{w_b}^2}{12})}. \tag{3.4}$$

The presence of such a background induces both a systematic uncertainty and an additional statistical uncertainty which can be large.

One element in the design of our optical lever is a strategy to eliminate the error due to background light. From the total intensity field $i_t = i(x) + i_b(x)$ we subtract $i_b + 3\frac{\sqrt{i_b p}}{p}$ where p is the width of the digitizing pixel which is much smaller than w and w_b. $\delta = 3\frac{\sqrt{i_b p}}{p}$ is the statistical fluctuation in the background light. After such a subtraction we generate a new intensity field given by

$$\begin{aligned} i_n &= \{i(x) + i_b(x)\} - i_b + 3\sqrt{\frac{i_b}{p}} && (3.5) \\ &\approx i(x) - 3\delta \quad for\ i_n > 0. \\ &= 0 \quad for\ i_n < 0. && (3.6) \end{aligned}$$

The new centroid calculated with this i_n is given by

$$x_n = l \pm \sqrt{\frac{(l^2 + \frac{w^2}{12})}{I_0 - 3\delta w}}. \tag{3.7}$$

Notice that $x_n \approx x_c$ when the fluctuation in the background intensity, δ, are small.

The second element in the design involves having multiple slits and corresponding multiple peaks in the image. Let us consider a grating of ν elements with a spatial periodicity of w, with $\frac{w}{2}$ opaque and $\frac{w}{2}$ transmitting [Fig. 3.3]. The full length of the grating is $W = \nu w$.

Centroiding as before we get

$$x_g = L \pm \sqrt{\frac{2}{\nu I_0}(L^2 + \frac{\nu^2 w^2}{12})}. \tag{3.8}$$

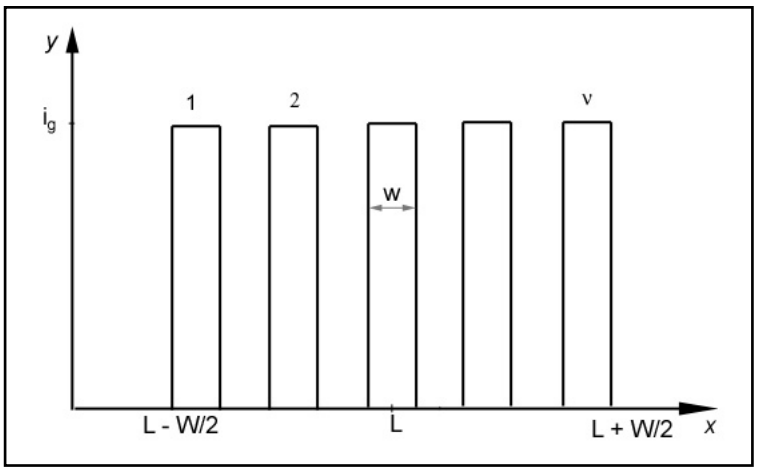

Fig. 3.3: Grating

The uncertainty in x_g is much larger than that in x_c and is about $\sqrt{2\nu}\Delta x_c$. This larger uncertainty is essentially due to the fact that the width of the light distribution has increased ν-fold.

To overcome this, consider a set of ν fiducial points x_i, $i = 1, 2, ..., \nu$, spaced at intervals of w. The centroid of the image of the individual grating elements with respect to the corresponding fiducial elements is given by

$$x_{ci} = x_{ci}^0 \pm \sqrt{\frac{1}{2I_0}(\frac{w^2}{4} + \frac{w^2}{12})}. \tag{3.9}$$

Averaging all the x_{ci}

$$\bar{x} = \frac{\sum x_{ci}^0}{\nu} \pm \sqrt{\frac{w^2}{6\nu I_0}}. \tag{3.10}$$

The precision in the determination of the centroid is substantially improved in this case as opposed to Eqn. 3.8. It is as though the photon density of an individual image of the slit has been increased by a factor ν. Since, the illumination of the slit is limited by the brightness temperature of the source, the above method of decreasing the statistical uncertainties proves useful.

The considerations related to the spacing of the grating are straightforward. The

mirror whose deflection angle is to be measured is smaller than the size of the autocollimator lens and as such determines the diffraction width of the image of the slit. Thus, the width a_0 of the opaque region between the slits may be taken as twice the full width of the diffraction width due to the mirror:

$$a_0 = 2\frac{1.22\lambda}{d_m}f. \tag{3.11}$$

Here d_m is the diameter of the mirror and f the focal length of the lens. The width a_t of the transparent part of the grating should be chosen such that the width of its image covers at least ~ 5 pixels, so that the spatial digitization of the image is adequate and does not lead to inadequate sampling of the possible asymmetries in the image profile.

$$a_t + \frac{1.22\lambda}{d_m}f \gtrsim 5p. \tag{3.12}$$

Although one would like to keep a_t as small as possible in an attempt to improve the angular resolution of the optical lever, it is necessary to keep a_t to be at least as large as the diffraction width itself to achieve a bright enough image, i.e., $a_t \sim 2.5p$. Further, it may be advantageous to choose its width large enough so that the light illuminating it does not get diffracted away even beyond the periphery of the lens. Thus, the grating constant $a = a_0 + a_t$ and it is of the order of four to five times the diffraction width of the mirror.

3.2 Construction of the Optical Lever

A sketch of the optical lever is shown in Fig. 3.4. It consists of an array of slits made with a photographic plate with transparent slits of 30 μm width, 90 in number, separated from each other with dark regions of 120 μm width (opacity of the dark regions is $< 100\%$). This array is illuminated by light emanating from a brightly illuminated ground glass sheet placed about five millimeters behind the array. A bank of red LEDs which emit in a forward cone angle of ~ 15 degree illuminate the ground glass sheet with overlapping circles of light. This increases the brightness and uniformity of

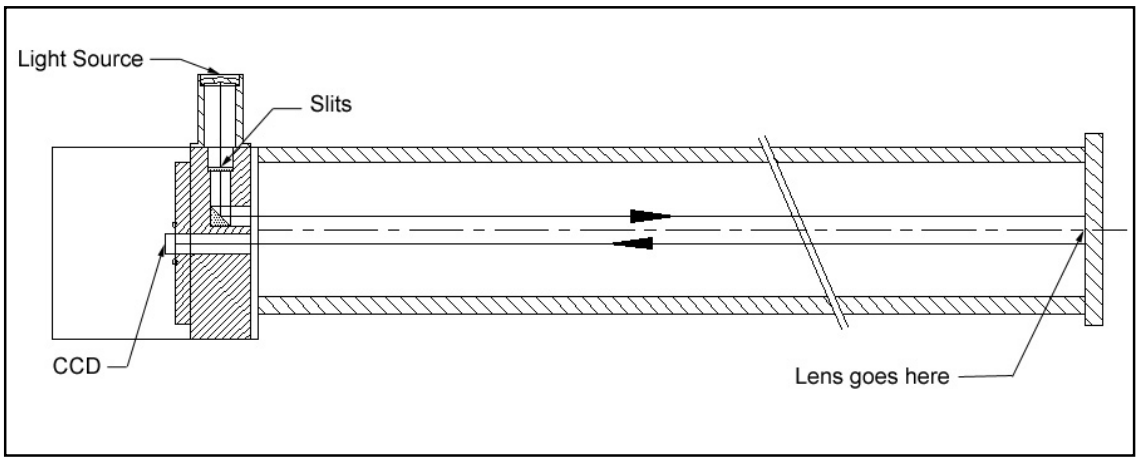

Fig. 3.4: Layout of optical lever assembly

illumination of the slit array. The array is placed in the focal plane of an achromatic lens of 1000 mm focal length and diameter 80 mm. The light passing through the slits is reflected towards the lens by a right angled prism, located such that the virtual image of the array is in the focal plane of the lens. The collimated light passing through the lens is reflected by the mirror whose deflection is to be measured. The reflected light passes back through the lens and gets imaged on the focal plane, just below the virtual image of the source.

The image is recorded on a CCD camera with a linear array of 6000 *Turbosensor*® photo-elements with a pixel size of 10 μm $\times$ 10 μm and center to center spacing of 10 μm. The well depth is 10^5 electrons. Two Analog to Digital Convertors (ADCs) built into the CCD camera digitize the charge on each pixels. The even pixels are read by one ADC while the odd pixels are read by the other. A constant bias voltage is added to the ADC input to ensure that the ADC always has a non-zero input. The camera is controlled using a National Instruments image acquisition card PCI 1424 and LabView software. The card sends the clock signals required to transfer the charges from the CCD pixels one by one to the ADC and also reads out the digitized output of the ADC. The clock signals also control the integration/exposure time of the camera. Thus a digitized image of the slit array is obtained. This image

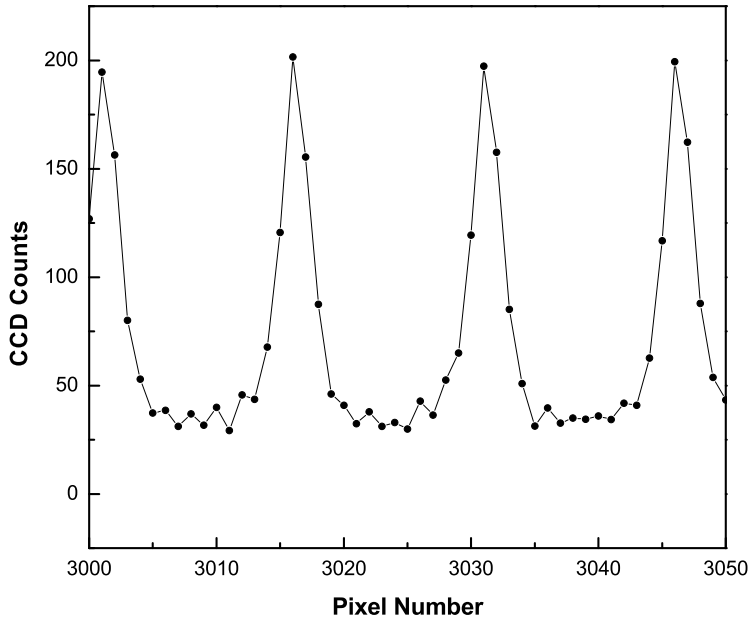

Fig. 3.5: A sample image of the slits falling on the CCD

is diffraction limited by the size of the mirror attached to the balance, yet clear peaks corresponding to the slits of the array can be seen, [Fig. 3.5]. The figure shows the counts of the ADC as a function of the CCD pixels. These images were obtained with an integration time of 32 ms. The calculation of the centroid from these images will be described in §3.3. When the mirror rotates through an angle θ the image and hence its centroid moves through a distance $2F\theta$ on the CCD, where F is the focal length of the lens.

The autocollimator assembly - with the slits, lens and the CCD - is housed such that the path from the slits to the lens and back to the CCD can be evacuated down to 10^{-2} Torr and stays at about 1 Torr for a couple of days when the pump is off. This helps to reduce image wobble on the CCD due to refractive index changes in the air path caused by fluctuations of temperature and by air currents.

3.3 Implementation of the Centroiding Algorithm

The centroid of the image is proportional to the angle the normal to the mirror subtends with respect to the optic axis. The first step in the determination of the centroid is to subtract from the individual pixel values c_i the dark current and the bias. The average value of the sum of dark and bias, d_i for each pixel is estimated from 100 frames without any light falling on the CCD. Accordingly we set the effective counts m_i as,

$$\begin{aligned} m_i &= c_i - d_i \qquad \text{for } d_i < c_i \\ m_i &= 0 \qquad\qquad \text{for } d_i > c_i \end{aligned} \tag{3.13}$$

A typical image profile thus generated would appear as shown in Fig. 3.6. The next step in the analysis is to clip off the low intensity background regions from the image. The background counts M_b, is estimated as 25% of the average counts per pixel falling on the CCD,

$$M_b = 0.25 \, \frac{\sum_{i=1}^{N} m_i}{N} \qquad \text{where } N = \text{Number of pixels} \tag{3.14}$$

$$\begin{aligned} M_i &= m_i - M_b \qquad \text{for } m_i > M_b \\ M_i &= 0 \qquad\qquad \text{for } m_i \leq M_b \end{aligned} \tag{3.15}$$

The intensities M_i represent the image of the sequence of the grating slits with the background subtracted and the noisy low intensity regions trimmed-off.

The next step in obtaining the centroid of the distribution takes note of the points made in Eqn. 3.8 and Eqn. 3.10. These requires us to establish a sequence of fiducial points across the CCD-array so that there is a fiducial point in close proximity to each of the images of the grating slits, ν in number. The location x_i of the first set of fiducials is defined by

$$x_i = \left[\mu(i-1) + \frac{1}{2}\right] p \ , \qquad i = 1, 2, 3, ...D \tag{3.16}$$

where μ is the width of the each slit image in pixels (= 15 in our case) and D is the total number of fiducial points.

Now computing the centroids of the intensity peaks that lie just ahead of each of these fiducials and averaging we get the effective location of the image

$$\bar{x} = \sum_{k=1}^{L}{}' \left(\frac{\sum_{j=k}^{k+\mu-1} M_j[\{(j-1)+\frac{1}{2}\}p - x_k]}{\sum_{j=k}^{k+\mu-1} M_j} \right) \tag{3.17}$$

Notice that in the averaging process we have to include only those values of k for which all $M_j^s(j = k \text{ to } k+\mu-1)$ are not zero; this is indicated with a prime on the outer summation sign. This procedure is similar to folding the image ν-times over so that all the peaks line up on each other. $\bar{x}$ thus obtained is the centroid distance modulo μp i.e., the mantissa. This may be added to a constant x_c defined by

$$\bar{x}_c = \sum_{i=1}^{L}{}' \frac{x_i}{\nu} \tag{3.18}$$

to get the complete centroid X:

$$X = \bar{x}_c + \bar{x} \tag{3.19}$$

One final step is needed before we are sure that the best possible centroid has been obtained. Consider Fig. 3.6 showing two possible image patterns that may occur for the two different orientations of the mirror.

In order to avoid the enhanced errors that will occur when image profiles straddle the fiducial points as in Fig 3.6(b), we need to ensure that the fiducials locate the image well within them. To this end, we introduce μ set of fiducials $x_{i,j}$ where $j = 1, 2 \ldots \mu$ such that $x_{i,j+1} = x_{i,j} + 1$. The image counts at the fiducial locations, $M_{x_{i,j}}$ are scanned to locate fiducial sets in which,

$$M_{x_{i,j}} = 0 \qquad for\ i = 1, 2, \ldots D \tag{3.20}$$

The centroid, X_j are calculated as given in Eqns. 3.17-3.19, for all $x_{i,j}$ that satisfy Eqn. 3.20. The 'true' centroid, C is chosen to be the one for which $\bar{x}_{c,j}$ is closest to $\mu/2$.

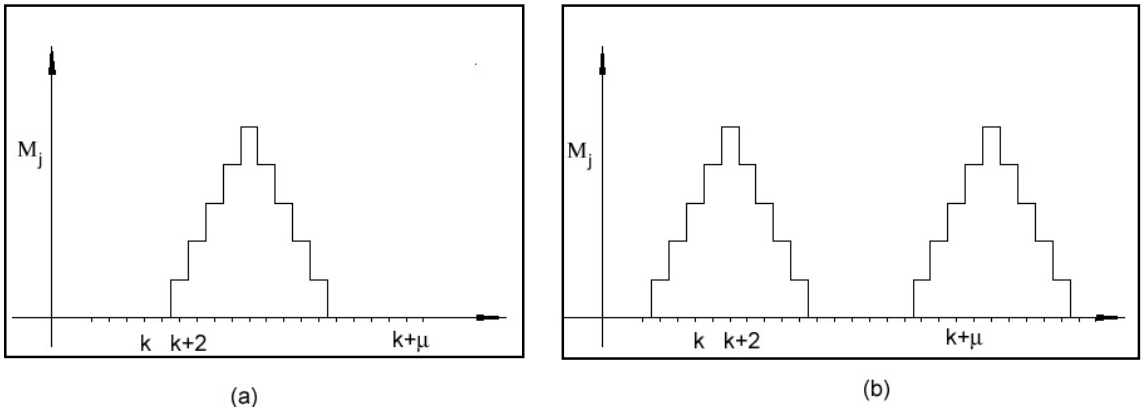

Fig. 3.6: Two possible image profiles with respect to the fiducial location, k; profile in panel (a) will give an accurate centroid as per Eqn.3.19; profile in panel (b) will have larger errors, since the centroid is calculated between k and $k + \mu$

3.4 Tests and characteristics of the optical lever

Several tests were performed to characterize the optical lever. The first was to study the dark and bias counts of the CCD pixels. In the CCD the first and last 2 pixels are internally shielded from light and are used by the CCD electronics to clamp the dark and bias. The bias voltage applied to the ADC convertor, is adjusted such that ADC output corresponding to the charges on these pixels is locked at 4-5 counts. This keeps a check on drifts due to the internal electronics. Over and above this, the counts in each pixel of the CCD were monitored for an exposure time of 32 ms without any light falling on the CCD. 100 such points were averaged for each pixel to determine the average sum of dark and bias of each pixel. This was later subtracted from every frame acquired, to determine the dark and bias subtracted counts per pixel.

The diffraction limited image of the 30 μm slits falling on the CCD are 5 pixels wide and are separated by 15 pixels. For an integration time of 32 ms, the peaks are at 200 counts compared to the saturation counts of 255 (with 8 bit digitization). The counts in the region between the peaks is at 40 as against the dark counts of 5 in the regions

of the CCD where no light is falling. Several such frames are co-added to increase photon counts. Each frame with about 600 counts per peak spread over 5 pixels and a total of 90 such peaks leads to a photon shot noise of 2.15×10^{-2} pixels/frame. This sets 1.08×10^{-7} radians/frame as the shot noise limit to the angular resolution of the optical lever.

In order to characterize the sensitivity of the system, the optical lever is made to look at a rigidly mounted mirror and the centroid of the peak intensity is monitored for several hours. The image is recorded every 1.6 sec after summing over 50 frames of 32 ms exposure time. A plot of the mean subtracted value of the centroid as a function of time is shown in Fig. 3.7. The fluctuations in the value of the centroid, as defined by the standard deviation of the data, are found to be at the 3.6×10^{-7} radians level, which is worse than the expected shot noise limit of 1.53×10^{-8} radians for 50 frames [see Fig. 3.7]. The source of this noise could be the air currents inside the autocollimator tube.

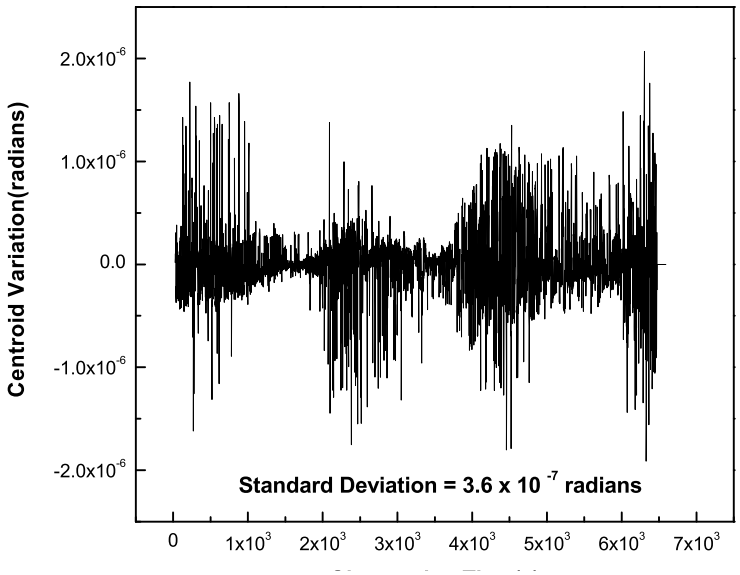

Fig. 3.7: Plot of variation in centroid position of a fixed mirror with time. The optical lever mount is at atmospheric pressure. Interval between readings is 1.6 sec.

To reduce the air currents, the path between the slit and the lens has to be evacuated. The fixed mirror is monitored as before after pumping the autocollimator to 10^{-2} Torr. The variation in the centroid in this case is shown in Fig. 3.8. The fluctuations in the

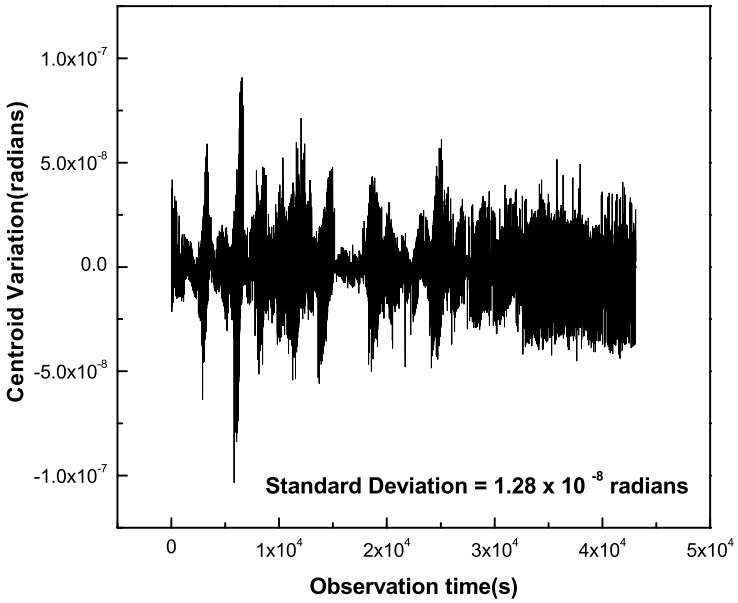

Fig. 3.8: Plot of variation in centroid position of a fixed mirror with time when the optical lever mount is at about 1 Torr. Interval between readings is 1.6 sec.

centroid value are reduced to about 1.28×10^{-8} radians for 50 frames, which is at the shot noise limit. Thus we have achieved a sensitivity of $\sim 1.6 \times 10^{-8}$ radians/$\sqrt{\text{Hz}}$. To improve on this, the total number of photons incident on the CCD will have to be increased by improving the mask and by efficiently coupling the light source to the slits.

The dynamic range of the optical lever is $\sim 1.8 \times 10^6$. The maximum angle that the instrument can measure is defined by the total length of the detector. The present mount for the optical lever masks about 500 pixels on either end of the CCD. Thus, with a total image width of 1.35 cm, the largest displacement in the centroid that we can measure is 3.65 cm, which corresponds to 1.8×10^{-2} radian deflection of the mirror.

Even at this stage we can see the salient features of this design of autocollimating op-

tical lever: it is capable of measuring angles with a sensitivity of $\sim 10^{-8}$ radians/$\sqrt{\text{Hz}}$ and has a dynamic range exceeding a few millions. These features are quite unique. With a better mask and light source we hope to reach a sensitivity of 3×10^{-9} radian/$\sqrt{\text{Hz}}$ without sacrificing the dynamic range.

References

[1] R. Cowsik et al. Torsion Balance Experiment for Measurement of Weak Forces in Nature. *Indian Journal of Pure & Applied Physics*, 27:691–709, 1989.

[2] R. V. Jones. Some Points in the Design of Optical Levers and Amplifiers. *Proceedings of the Physical Society B*, 64:469–482, June 1951.

[3] R. V. Jones and J. C. S. Richards. CORRESPONDENCE: Recording optical lever. *Journal of Scientific Instruments*, 36:199, April 1959.

4. CHARACTERIZATION OF THE APPARATUS

Abstract: This chapter presents the tests and characterizations performed on the experimental apparatus.

4.1 The Torsional Pendulum

The force transducer in our experiment is a torsional pendulum. The sensitivity of the torsional pendulum to any torque acting on it is related to the moment of inertia, I of the mass element suspended and torsional constant of the suspension fibre, κ. These parameters determine the time period of oscillation of the pendulum. The period, T_b is given by

$$T_b = 2\pi\sqrt{\frac{I}{\kappa}} \ .$$

Another important parameter of an oscillator is its quality factor, Q. It is a measure of the damping in the system and is defined as the ratio of time taken for the amplitude of the oscillator to fall by $1/e$ to the time period of the oscillator.

In order to characterize our torsional pendulum, it was allowed to oscillate freely inside the vacuum chamber at a pressure of 4.0×10^{-8} Torr with an amplitude of $\sim 3.0\times10^{-3}$ radians. The oscillations are monitored continuously for about a day. Fig. 4.1 shows a few cycles of the oscillations. The time period and Q are obtained from by Fourier power spectrum of this time series data. The power spectrum calculated from the Fast

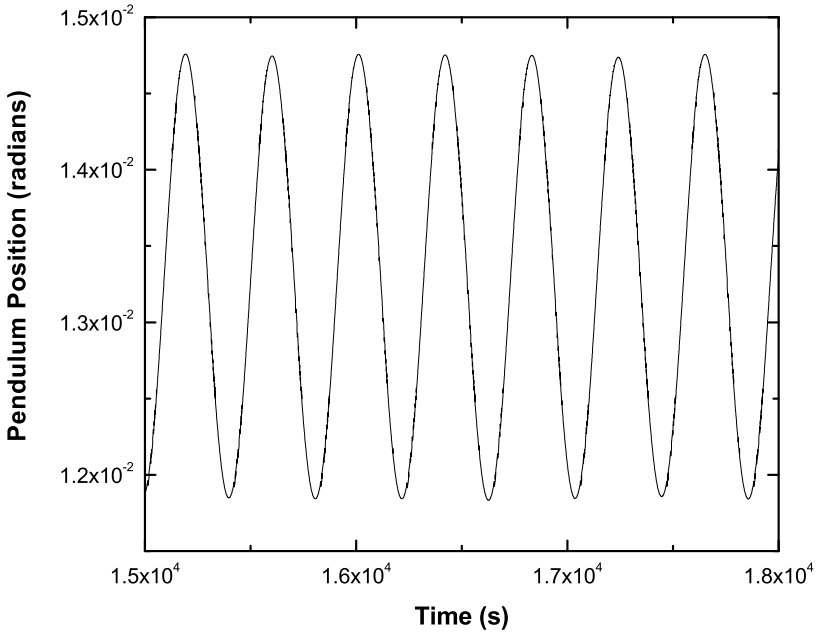

Fig. 4.1: Free Oscillations of the pendulum

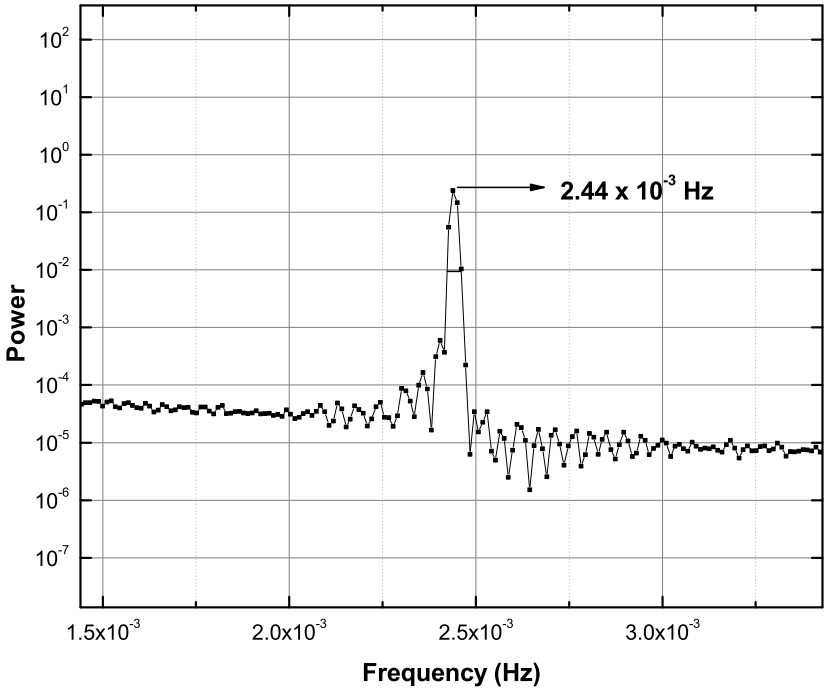

Fig. 4.2: Power spectrum of the torsional oscillations

Fourier Transform(FFT) of the data is shown in Fig. 4.2. The peak in the spectrum occurs at a frequency of 2.44×10^{-3} Hz corresponding to a period of 409 sec. The quality factor as determined from the width of this peak is ~ 56. But this is limited by the resolution of the FFT fixed by the total observing time of about 20 hrs. The true Q is ~ 100 as we can see from several such one day stretches of oscillations. The equilibrium position of the pendulum drifts by $\sim 5.0 \times 10^{-5}$ radians, peak to peak, over a day (diurnal cycle). The signal to noise ratio achievable in the system depends on the Nyquist noise which puts a limit on the smallest torque that we can measure. The Nyquist noise is given by,

$$\tau_{Nyq} = \left(\frac{4k_B T\kappa}{3Qt\omega_b}\right)^{1/2} \tag{4.1}$$

Here, κ is the torsion constant of the suspension fibre, T the laboratory temperature, Q is the quality factor of the fibre, t is the total time of observation and ω_b is natural oscillation frequency of the balance. Taking typical values $T = 300^\circ$ K, $\kappa = 0.05$ dyne.cm.rad^{-1}, $Q = 100$, $t = 50$ s, and $\omega_b = 1.5 \times 10^{-2}$ rad.s^{-1}, $\tau_{Nyq} \approx 6.1 \times 10^{-9}$ dyne.cm. This value is two orders of magnitude smaller than the force sought for in the present set of experiments.

4.2 Pendulum behaviour during evacuation

It is repeatedly noticed that the level of vacuum in the chamber plays a crucial role in determining the trajectory of the pendulum within the assembly. During assembly the lens is typically positioned at a separation > 5 mm from the pendulum while the capacitors are fixed at about 2 mm from it. When pump down starts, the pendulum tends to remain 'stuck' to either of the capacitors until a pressure of $\sim 10^{-3}$ Torr is reached. At this stage the pendulum starts to oscillate with very short periods of about 20 s. As the pressure drops the period progressively increases and reaches ~ 200 s at 10^{-5} Torr. The period stabilizes to the 'free oscillation period' of about 400 s when the pressure reaches $\sim 10^{-7}$ Torr. Further drop in the pressure does not change the period of the pendulum. We have also tested the behaviour of the

pendulum when the pressure is allowed to rise due to degassing, with pumps shut off. The period begins to drop as the pressure increases to about 10^{-6} Torr. This behaviour of the pendulum was not systematically characterized. But, it seems clear that even the low pressure cushions sandwiching the pendulum disc in the small gaps between the capacitors and the disc can severely alter the effective torsional spring constant of the oscillator. Our system is operated at a vacuum of $\sim 4 \times 10^{-8}$ Torr to avoid these effects.

4.3 Calibration of the force arm

The experiment attempts to measure the Casimir force between a spherical lens surface and the flat surface of the torsion pendulum. The torque due to this force on the pendulum, depends on the lateral distance (force arm) of the point at which the force acts on the pendulum as measured from the suspension axis. The force arm is determined from the point of contact between the lens and the pendulum, which is estimated as follows: at some initial position of the lens, the pendulum is pulled towards the lens by applying voltages on the capacitor plates. The pendulum position is monitored using the optical lever as it approaches the lens. The position where the pendulum touches the lens is deciphered from the centroid location on the optical lever at which the pendulum suddenly turns around. The average point of contact of the lens is measured from several touches at each position of the lens. The lens is then translated by known amount using the EncoderMike® actuator [see §2.4]. The point of contact of the lens on the pendulum and the force arm change negligibly, but the angular position of the pendulum at which the contact occurs changes significantly [Fig. 4.3]. This new angular position at which the contact occurs is measured for several displacements of the lens and a plot of it is shown in Fig. 4.4. Thus, the relation between the linear displacement of the lens and the angular displacement of the centroid of the image at the point of contact is obtained from the slope of the data. The slope tells us that 0.114 μm translation of the lens corresponds to 1 pixel movement of the image centroid. Hence when the point of contact moves transverse

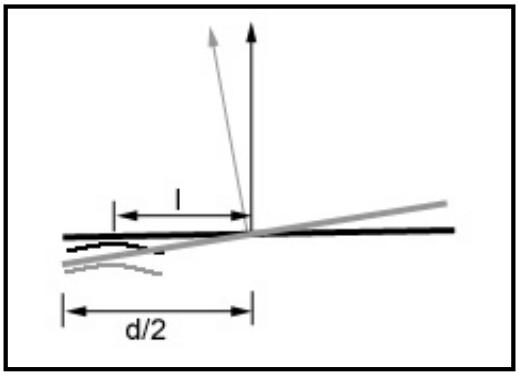

Fig. 4.3: Schematic representing the 'touch position' and its relation to the force arm

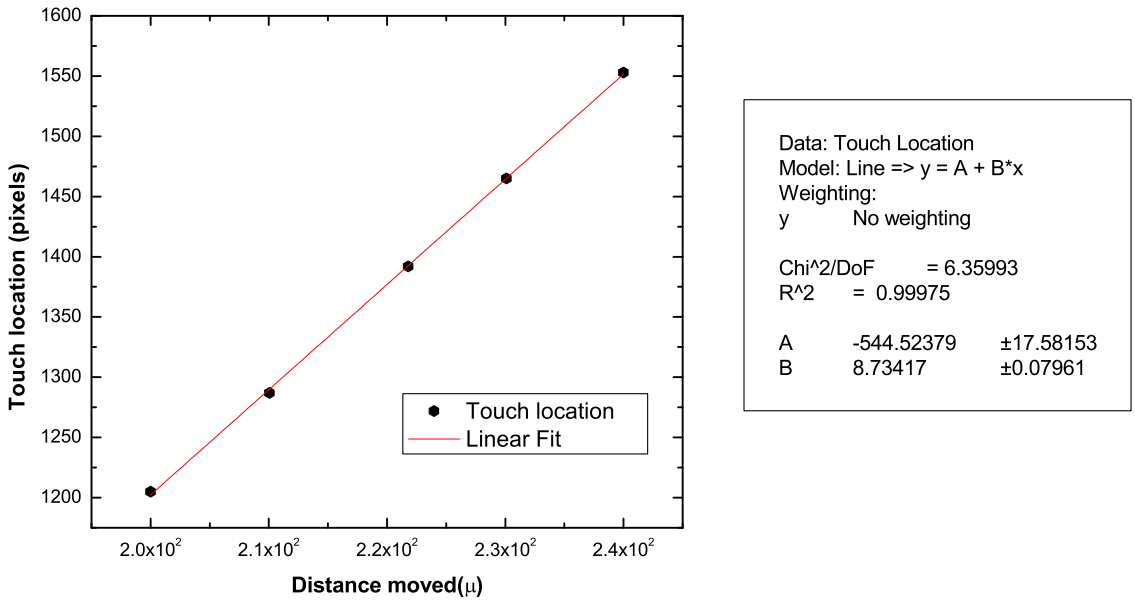

Fig. 4.4: Plot of the touch location as a function of lens position

to the plane of the pendulum (towards or away from the lens) by 0.114 μm, image shifts by 1 pixel. From the optical lever parameters, we know that a image displacement of 1 pixel corresponds to a transverse movement of 0.2 μm at the edge of the pendulum disc which is at $d/2 = 40$ mm from the suspension axis [Fig. 4.3]. Thus the force arm l or point of contact is at 22.8 mm from the axis of the pendulum.

5. CASIMIR FORCE MEASUREMENT - STRATEGY, DATA ACQUISITION AND ANALYSIS

Abstract: The basic procedures followed in our experiment will be described in this chapter. The chapter begins with an overview of the forces influencing our torsion pendulum transducer and goes on to describe how the data is acquired in order to comprehend these. The analysis of this data to extract information about Casimir force is then discussed in detail. There is clear evidence for the finite temperature Casimir force, detected for the first time, in the analyzed data.

5.1 Strategy of the experiment

The main objective of the experiment is to measure the force of attraction between a fixed lens and a flat plate suspended as a torsional pendulum. In the absence of the lens, the only torque acting on the pendulum is the restoring torque from the fibre. As the lens is brought close to the fibre, various forces begin to act on the pendulum. The basic torques acting on the pendulum when the pendulum oscillates near the lens are the fibre restoring torque and the torques due to electrostatic and Casimir force.

The presence of all these forces will introduce changes on the torsional oscillations of the pendulum. Since these forces in general arise from potentials that differ from the

quadratic harmonic potential due to the torsion in the fibre, they make the motion of the pendulum anharmonic. As described in the previous chapters, we record the angular position, θ of the fibre as a function of time, t. Thus the strategy adopted is to extract information about the forces from the t versus θ data.

The free oscillations of a pendulum will be simple harmonic. The existence of other potentials, besides the harmonic potential due to the fibre, will contribute to the acceleration $\ddot{\theta}$, thereby changing the simple linear relationship of $\ddot{\theta}$ with the amplitude of the oscillations. If $f(\theta)$ is the net force on the pendulum then,

The torque on the pendulum,

$$\tau(\theta) = f(\theta)l \text{ and} \tag{5.1}$$

$$I\ddot{\theta} = \tau(\theta) \tag{5.2}$$

where l is the lateral distance of the point at which the force acts on the pendulum as measured from the suspension axis, $\ddot{\theta}$ is the angular acceleration of the pendulum. Similarly the angular velocity $\dot{\theta}$ is related to the potential $U(\theta)$,

$$\frac{1}{2}I\dot{\theta}^2 + U(\theta) = E = const. \tag{5.3}$$

$$\text{where } \tau(\theta) = -\frac{\partial U(\theta)}{\partial \theta} \tag{5.4}$$

Thus, by measuring $\dot{\theta}$ or $\ddot{\theta}$ the potential and the forces that affect the pendulum can be characterized.

5.1.1 Summary of Forces acting on the Pendulum

Several forces between the lens and the pendulum begin to become sizeable as they approach each other to within about 100 μm. We now discuss the forces that play a major role in the motion of the pendulum.

Fibre restoring torque:

The restoring torque due to the fibre makes the pendulum execute simple harmonic motion about a mean position, hereafter referred to as the 'null' position θ_0. As is well known, this torque always acts towards θ_0 and in proportion to the deflection of the torsion balance from this position. In the following descriptions, the distances and the angles are measured with respect to the position of the lens as origin [Fig. 5.1]. During the experiment, the presence of other forces will generate new torques which will shift the balance to a new equilibrium position θ_e. By appropriate rotation of the shaft from which the balance is suspended, the equilibrium position θ_e is made to lie between the lens at $\theta_l = 0$, and θ_0. The restoring torque, τ_{fib} and the acceleration, $\ddot{\theta}_{fib}$ on the pendulum due to this torque are given by:

$$\tau_{fib}(\theta) = \kappa(\theta_0 - \theta) \tag{5.5}$$

$$\ddot{\theta}_{fib} = \frac{\kappa}{I}(\theta_0 - \theta) \tag{5.6}$$

$$\ddot{\theta}_{fib} = 2.46 \times 10^{-4}(\theta_0 - \theta) \tag{5.7}$$

where κ is the torsion constant of the fibre, I the moment of inertia of the pendulum and θ_0 is the equilibrium position of the pendulum. Similarly the potential, U_{fib} and the angular velocity, $\dot{\theta}_{fib}$ are given by,

$$U_{fib} = \frac{\kappa}{2}(\theta_0 - \theta)^2 + const. \tag{5.8}$$

It is convenient to write in general,

$$\dot{\theta}^2_{fib} = -\frac{2U}{I} + const. \tag{5.9}$$

$$\equiv -U_N + const. \tag{5.10}$$

With this we may think of $\dot{\theta}^2$ as just the negative of the normalized potential U_N.

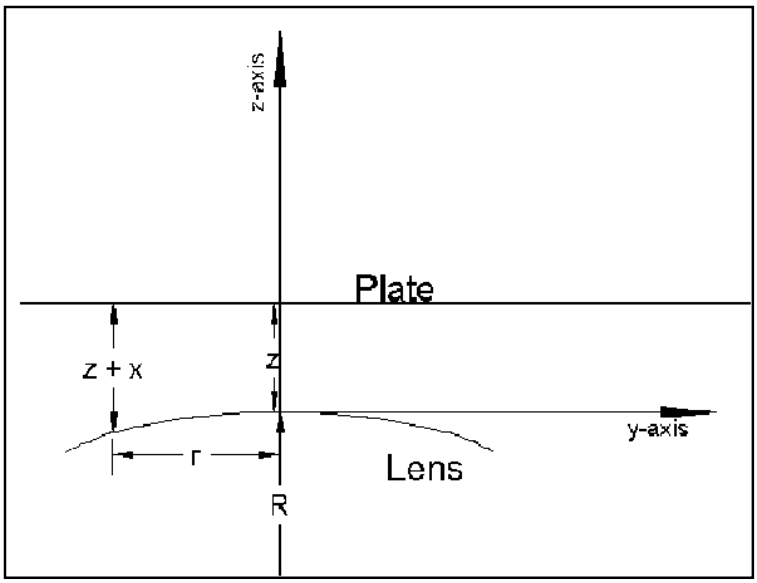

Fig. 5.1: Reference axes for the system.

Casimir Force

The Casimir force per unit area between two parallel conducting plates separated by a distance z, at $T = 0$ K is given by,

$$f_{c0}(z) = -\frac{\pi^2 \hbar c}{240 z^4} \tag{5.11}$$

$$= -\frac{0.013}{z_\mu^4} \quad \text{dyn.cm}^{-2} \quad \text{where } z_\mu \equiv z \text{ in microns} \tag{5.12}$$

For a finite temperature T we approximate the distance dependence as

$$f_{cT}(z) = f_{c0}(z) \qquad \text{for} \quad z < \lambda_T \tag{5.13}$$

$$f_{cT}(z) = f_{c0}(z)\frac{z}{\lambda_T} \qquad \text{for} \quad z > \lambda_T \tag{5.14}$$

where λ_T is the distance at which the finite temperature effects become important. Comparing Eqn. 5.14 with the expression for Casimir force at 'high temperature' described in Chapter 1 (Eqn.1.5),

$$F_c^T(d) \simeq -\frac{1.2 k_B T}{4\pi z^3} \quad \text{at high } T \tag{5.15}$$

we can estimate that for $T = 303^\circ$ K, $\lambda_T \sim 3.26$ μm.

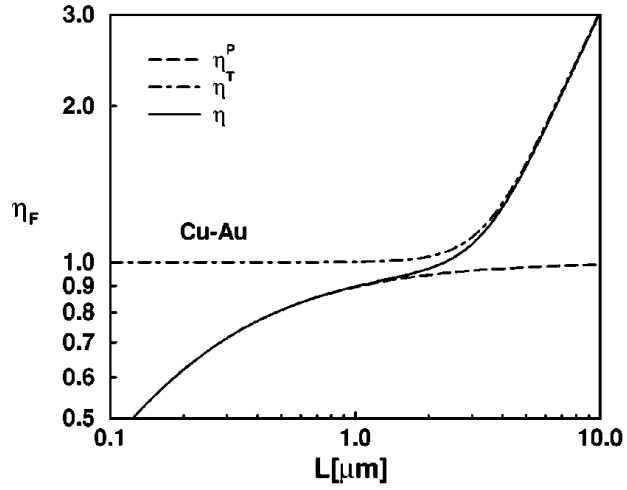

Fig. 5.2: Ratio of the Casimir force calculated taking into account the finite conductivity and finite temperature effects to the Casimir force at zero temperature between ideal conductors is plotted as a function of spacing between plates (from, [17]). Our experiment is in the distance range of 2 μm - 10 μm

For convenience, we write Eqns. 5.11 and 5.14 as,

$$f_{c0}(z) \equiv -\frac{A_c}{z^4} \quad dyn.cm^{-2} \tag{5.16}$$

$$f_{cT}(z) \equiv -\frac{A_c}{\lambda_T z^3} \quad dyn.cm^{-2} \tag{5.17}$$

The Casimir force between the lens and the pendulum can now be estimated using the "Derjaguin (proximity) approximation", often called "proximity theorem" [1]. For our geometry the expression has two parts to it depending on the separation between the lens and the plate. At small separations, the zero temperature Casimir force dominates. As the separation increases, finite temperature effects become important and the force law changes. Fig. 5.2 shows this change in the law (see chapter 1 for the definition of the ratios). The Casimir force for the lens-plate configuration is given

by (see Appendix B for details),

$$f_{cl}(z) = -\frac{2\pi R A_c}{3}\left[\frac{1}{z^3} - \frac{1}{(z+\lambda_T)^3} + \frac{3}{2\lambda_T}\left\{\frac{1}{(z+\lambda_T)^2} - \frac{1}{(z+x_{max})^2}\right\}\right], \quad \text{for } z < \lambda_T \tag{5.18}$$

$$f_{cl}(z) = -\frac{\pi R A_c}{\lambda_T}\left\{\frac{1}{z^2} - \frac{1}{(z+x_{max})^2}\right\}, \quad \text{for } z > \lambda_T$$

where $x_{max} = \frac{r_{max}^2}{2R}$ and $z = l\theta$ is the separation between the lens and the plate, R is the radius of curvature of the lens and r_{max} is the aperture radius of the lens (Fig. 5.1). The potentials for the same configuration are,

$$U_{cl}(z) = \frac{\pi R A_c}{4}\left[\frac{1}{z^2} - \frac{1}{(z+\lambda_T)^2} + \frac{8}{3\lambda_T}\left\{\frac{1}{(z+\lambda_T)} - \frac{1}{(z+x_{max})}\right\}\right], \quad \text{for } z < \lambda_T \tag{5.19}$$

$$U_{cl}(z) = \frac{2\pi R A_c}{3\lambda_T}\left\{\frac{1}{z} - \frac{1}{(z+x_{max})}\right\} \quad \text{for } z > \lambda_T \tag{5.20}$$

The angular velocity and acceleration due to Casimir force can be calculated using Eqns. 5.3 and 5.4.

It may be noted that the roughness of the surface is not a major correction term to the Casimir force in our experiment, since it focuses on Casimir force at relatively large separations between the metal surfaces. However, the finite conductivity correction, a reduction in force amounting to approximately 10% needs to be applied throughout the measurement range.

Electrostatic Forces

There are various sources of electrostatic force between the lens and the plate. Several effects lead to potential differences between metal coated surfaces even when they are externally connected to ground [12, 13, 1]. Small difference in the contact potentials in these connections can lead to potential differences between these surfaces. With care, such potentials can be minimized to a few mV level. Another source of electrostatic interaction between the bodies are patch fields. These are microscopic electric

potentials found on surfaces of metals. The different crystalline planes of a given material can have work functions that can differ by as much as 1 V . If the coated metal surface is a mosaic of random microscopic crystal planes, local potential differences will occur between each of these micro-size patches. Surface contamination in the metal coatings can also lead to local variations in the work function and also provide sites for trapping electrical charges.

Force due to Capacitative coupling:

The conductive surfaces of the lens and the plate, form a capacitance which is given by "proximity theorem" to be,

$$\begin{aligned} C_l &= \epsilon_0 \langle \frac{A}{d} \rangle && (5.21)\\ &= \epsilon_0 \int_{r=0}^{r=r_{max}} \frac{2\pi r dr}{[z + \frac{r^2}{2R}]} && (5.22)\\ &= 2\pi R \epsilon_0 \ln \left\{ \frac{z + \frac{r_{max}^2}{2R}}{z} \right\} && (5.23) \end{aligned}$$

where ϵ_0 is the dielectric constant in free space, R is the radius of curvature of the lens, z the separation between the lens and the pendulum in metres and r_{max} is the aperture radius of the lens. If the voltage difference, V between the lens and the plate were zero, the net force due to this capacitance will be zero. But potentials can be present due to any of the reason mentioned above. The electrostatic potential energy due to these between the lens and the plate is given by,

$$\begin{aligned} U_{el} &= \frac{1}{2} C_l V^2 && (5.24)\\ &= \pi R \epsilon_0 V^2 \ln \left\{ \frac{z + \frac{r_{max}^2}{2R}}{z} \right\} && (5.25) \end{aligned}$$

The resulting capacitative force is given by,

$$\begin{aligned} f_{el} &= -\frac{d}{dz} \left[U_{el} \right], && (5.26)\\ &\approx -\frac{\pi R \epsilon_0 V^2}{z} \qquad \text{for } r_{max}^2 \gg 2Rz. && (5.27)\\ & && (5.28) \end{aligned}$$

We approximate the corrections to the above formula, due to surface roughness and a variety of other causes and write for the torque,

$$\tau_{el} = -\frac{\pi R\epsilon_0 V^2}{(\theta-\theta_r)} \tag{5.29}$$

$$\tag{5.30}$$

where the roughness parameter θ_r will be determined self-consistently from the data. The voltage V comprises of the applied voltage V_{ap}, the D.C voltage $V_{(0,dc)}$ due to contact potentials and other causes and $V_{(0,ac)}$ due to the stray pick up fields and leakage, etc. This contributes to the normalized force a term,

$$\ddot{\theta}_{el} = -\frac{\pi R\epsilon_0 V^2}{I(\theta-\theta_r)}. \tag{5.31}$$

Force due to charges on the lens/pendulum:

Stray electric charges on the surfaces of the lens and the plate also lead to electrostatic forces. The potential between these charges depends in detail on their distribution on the surfaces and cannot be modeled easily [see for example, [10]]. An upper limit to the strength of this force may be obtained by assuming that all the charge is concentrated at the point of contact between the lens and the plate and that a simple inverse square law applies for the force with an equidistance image charge. The potential due this is given by,

$$U_{qq} = \frac{q^2}{4\pi\epsilon_0 z_m}, \tag{5.32}$$

$$z_m = 2z, \text{the separation between the lens and the pendulum.} \tag{5.33}$$

The force and the acceleration on the pendulum due to it are,

$$f_{qq} = -\frac{q^2}{4\pi\epsilon_0 z_m^2}. \tag{5.34}$$

$$\text{Torque, } \tau_{qq} = -\frac{q^2}{16\pi\epsilon_0 l\theta^2}, \tag{5.35}$$

$$\ddot{\theta}_{qq} = -\frac{q^2}{16\pi\epsilon_0 lI\theta^2}, \tag{5.36}$$

$$= -2.94\times 10^{15}\frac{q^2}{\theta^2}. \tag{5.37}$$

where q is effective charge on the lens/pendulum. For a distributed charge the $\sim 1/\theta^2$ dependence will change over to a slower dependence of $\sim 1/\theta$. This will be the case with metallic surfaces when there are some residual charges on them.

Force due to charge and voltage on the lens:

One more source of electrostatic force is the combined effect of the charges and voltage differences present. The electric field, $\mathcal{E}$, due to these voltages, V interacts with the charge, q to apply an additional force on the pendulum of the form,

$$f_{vq} = -q\mathcal{E} = -\frac{qV}{z}, \tag{5.38}$$

$$\text{Torque, } \tau_{vq} = -\frac{qVl}{z}, \tag{5.39}$$

$$\text{Acceleration, } \ddot{\theta} = -\frac{qV}{I\theta}, \tag{5.40}$$

$$= -5.2 \times 10^4 \frac{qV}{\theta}. \tag{5.41}$$

$V_0 = V_{(0,dc)} + V_{(0,ac)}$; however, since the acceleration is linear in V as shown in Eqn 5.41 and the pick up voltages are at frequencies much higher than the frequency of oscillation of the balance at a few milliHertz, the A.C torques will average to zero and will not contribute.

Gravitational force:

The gravitational attraction of the lens on the pendulum gives rise to a torque of $\sim 4 \times 10^{-5}$ dyne.cm on it. This corresponds to the attraction between disc shaped masses of approximately 10 g each separated by an effective distance of about 5 mm. The 'compensating plate' (refer §2.5) is used to balance this gravitational torque of the lens. The mass of the compensating plate is equal to that of the lens but its position with respect to the torsion pendulum disc is not exactly the same as the lens. Therefore, the cancellation of the gravitational torque is only approximate and the residual gravitational torque on the pendulum is estimated to be $\sim 10^{-6}$ dyne.cm. This changes only by $\sim 10^{-8}$ dyne.cm when the lens is moved over the

distance of 50 μm, since the fractional change in the effective separation between the centers of gravity of the plate and the lens assembly is only 1/100. The change in angular acceleration of the pendulum due to this is below the present sensitivity of the experiment.

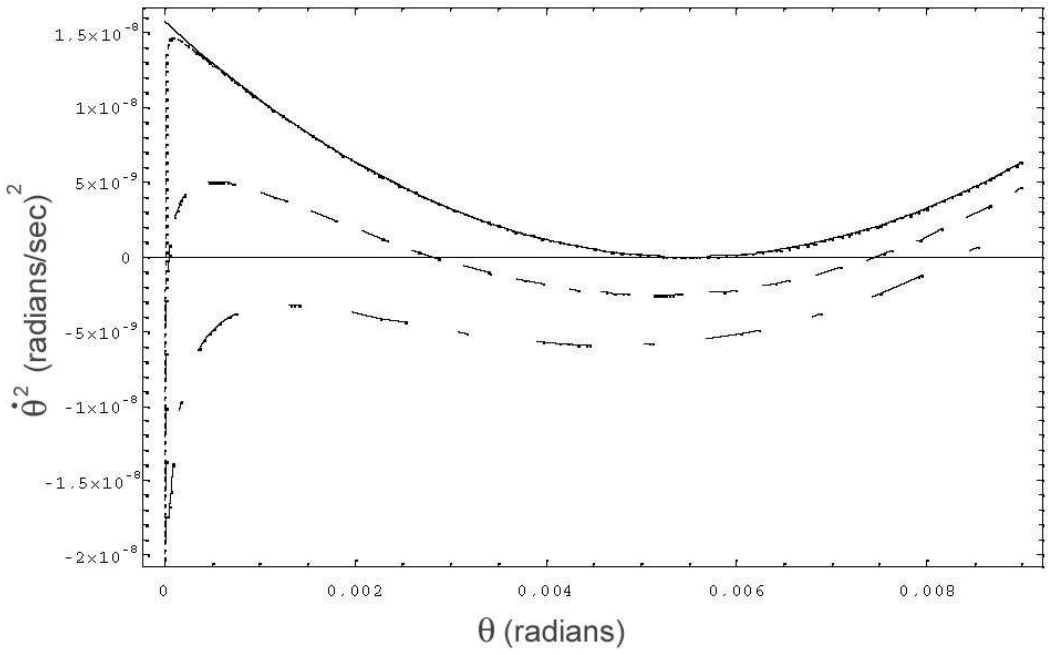

Fig. 5.3: A plot of normalized potential $U_N = 2U/I$ is shown as a function of θ. The solid line maps the potential due to the fibre restoring force when the equilibrium position of the pendulum, $\theta_0 = 5.3 \times 10^{-3}$ radians. The dotted line is a plot of the net potential due to the lens and the fibre for $V = 5$ mV, $q = 1 \times 10^{-15}$ C and $\lambda = 3.26$ μm. The dashed line is a plot for $V = 50$ mV and the dashed dot line for $V = 75$ mV on the lens

5.1.2 The Effect of these Forces on the Pendulum

A plot of the square of the angular velocity, $\dot{\theta}^2 = -U_N$ of the pendulum as a function of θ is shown in Fig. 5.3. This maps the potential in the region of oscillation of the pendulum in the absence of the lens (solid line) and when the lens is at a distance of about 120 μm from the null position θ_0 (various dashed lines). For calculating

the potential due to the lens, the net voltage difference between the lens and the pendulum V is set to 5 mV (dotted line), 50 mV (dashed line) and 75 mV (dashed dot line). The net charge, q is taken to be 1×10^{-15} C and the distance at which the Casimir force changes from zero to finite temperature form, λ is taken to be 3.26 μm.

From the plot it can be seen that the presence of the electrostatic and Casimir forces, considerably changes the potential between the lens and the plate. The potential is highly attractive towards the lens for small angular separations. The angular distance at which this change over to attractive potential happens depends on the net voltage on the lens. Thus, when the voltage on the lens is 5 mV, the change over happens at a distances of about 5×10^{-5} radians. As the voltage on the lens increases, the change over point extends away from the lens. The equilibrium position of oscillation of the pendulum is also shifted for voltages higher than 20 mV. The potential beyond 7×10^{-3} radians is shifted for higher voltages but is parallel to the pontetial due to free fibre. The potential below 7×10^{-3} radians is flatter than the potential due to free fibre. Thus the oscillation period of the pendulum is modified even for small amplitude oscillations of the pendulum.

As the lens is brought close to the pendulum *the signatures of the electrostatic forces can be seen by looking at changes in:*

(a) the equilibrium position of the pendulum,

(b) the time period of the pendulum, and

(c) the angular acceleration $\ddot{\theta}$ of the pendulum as a function of its angular position θ.

Since the Casimir force falls off more rapidly than the electrostatic force, to study the effects of Casimir force, we need to go closer to the lens, *i.e.*, $< 1 \times 10^{-3}$ radians. At those angular distances, the pendulum will no longer oscillate but will start to fall

towards the lens. The force in that region then can be elucidated only from the θ versus $\ddot{\theta}$ of the pendulum. *Hence, to estimate Casimir force, we need to look at the θ versus $\ddot{\theta}$ of the pendulum at angular distances of $< 1 \times 10^{-3}$ radians.*

To completely fathom the electrostatic forces though, in addition to measurements of the changes on the pendulum as a function of lens position, knowledge about these changes as a function of voltage on the lens are also essential. The force due to the capacitive coupling increases as the square of the net voltage on the lens, while the charge effect is linear in voltage. Hence, by studying the force dependance on the voltage, an estimate of the effect of both the residual voltage and the charge on the pendulum can be obtained.

5.2 Data Acquisition:

Despite considerable care taken during the assembly to minimize the voltages and charges on the lens and the pendulum, certain residuals are unavoidably present in the apparatus and it is essential to characterize these electrostatic forces. All the earlier experiments that looked for Casimir forces have seen the effect of these forces [8, 7, 16, 18, 24, 14, 4, 2]. Since the distance range in our experiment is larger than the earlier experiments on Casimir force, electrostatic forces are a strong background. Hence, the data acquisition was tuned to be able to estimate the electrostatic forces and subtract them in order to look at the Casimir force at separations between 2 μm - 10 μm.

The Casimir force falls off more rapidly with distance than the electrostatic forces. Thus, at distances > 25 μm the electrostatics forces will dominate by more than two orders of magnitude. At these separations corresponding to a angular distance of $> 1 \times 10^{-3}$ radians, even for a net voltage, V of 75 mV between the lens and the

pendulum, it will execute anharmonic oscillations. Hence, the presence of the electrostatic force can be studied by looking at the oscillations of the pendulum in the potentials summarized in the previous section.

Data was acquired in three main modes:

- Small amplitude oscillations that sampled the region within 5×10^{-4} radians of the equilibrium position.
- Large amplitude oscillations that sampled regions up to an angular separation of 1×10^{-3} radians from the lens.
- Accelerated fall of the pendulum onto the lens starting from an angular separation of $< 5 \times 10^{-4}$ radians.

Small amplitude oscillations

To start with, the lens is positioned at a distance of about 0.35 mm from the equilibrium position of the pendulum. The oscillations of the pendulum for amplitude of $\sim 2.5 \times 10^{-4}$ radians, i.e, 5.7 μm are monitored using the autocollimator. The lens is then moved stepwise slowly towards the pendulum until the separation between the two is reduced to 100 μm. At each separation, the pendulum is allowed to oscillate with an amplitude of $\sim 2.5 \times 10^{-4}$ radians for several (> 10) cycles. The position of the pendulum in units of CCD pixel numbers is recorded every 0.16 sec. Fig. 5.4 shows the raw data of few cycles of oscillations of the pendulum.

From this data the change in the period and the equilibrium position of the pendulum as a function of lens position is derived. As the lens is brought closer the equilibrium position, the period of the pendulum remained unchanged until the separation is > 250 μm. For lower separations, the equilibrium position of the pendulum shifts closer to the lens. The period changes from about 406 sec at 0.35 mm separation to

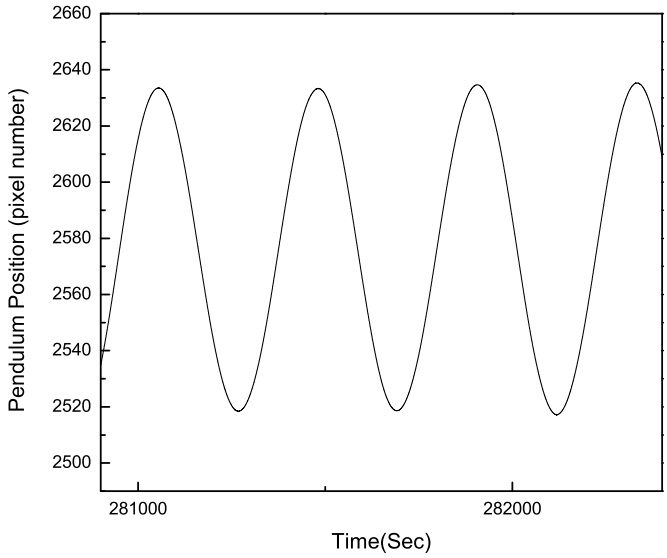

Fig. 5.4: The raw data showing a few cycles of small amplitude oscillations of the pendulum

about 503 sec at 100 μm separation.

These changes are shown in Figs. 5.5 and 5.6. Fig. 5.5 shows the change in equilibrium position as the lens is moved closer to the pendulum. The pixel numbers on the CCD are used as the reference to see this change. The equilibrium position is not measured with the lens as origin as the position of lens itself changes. The separation marked is the effective separation calculated taking into account both, the change in equilibrium position and the change in the lens position. Fig. 5.6 shows the variation in the time period of the pendulum for the same separations.

Thus, at *separations* $> 250\ \mu m$ the interaction of the pendulum with the lens is negligible and the motion of the pendulum is defined by properties of the suspension fibre. Hence, this region *can be used to characterize the fibre properties.* To study the effects of the interaction with the lens, separations $< 120\ \mu$m are ideal as the change in the equilibrium position and time period are steeper in this region.

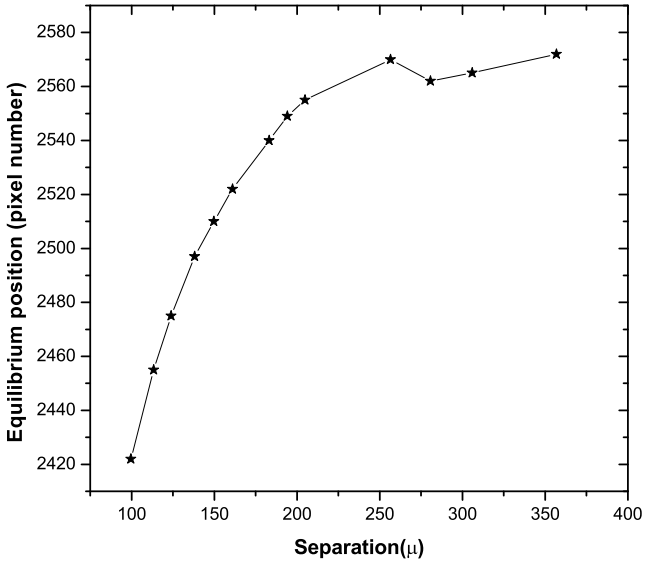

Fig. 5.5: The change in the equilibrium position of the pendulum as the lens is moved closer to it.

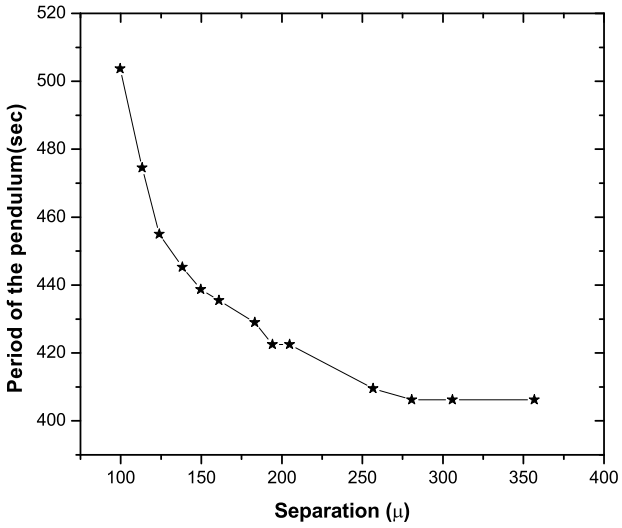

Fig. 5.6: The change in the time period of the pendulum as the lens is moved closer to it.

In addition to looking at the changes in the equilibrium position of the pendulum as a function of separation, the changes in the equilibrium position are also studied as a function of voltages applied on to the lens. The lens is kept at a fixed position and the voltage on the lens is scanned until the pendulum sees the least force from the lens. This would be the voltage at which the applied voltage V_{ap} balances the residual voltage on the lens $V_{0,dc}$. The data is taken for different null positions of the lens. The observations are summarized in Fig. 5.7

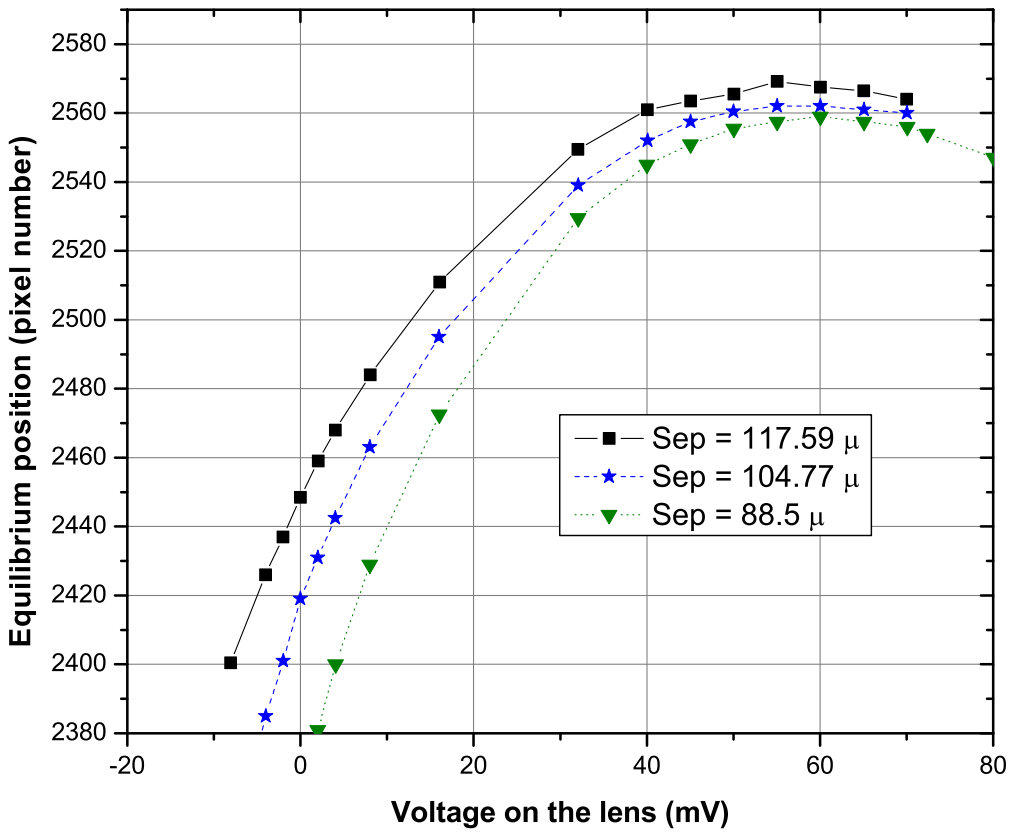

Fig. 5.7: The equilibrium position of the pendulum as a function of voltage applied on the lens at various lens positions

In Fig. 5.7, the separations marked are the distance between the lens and the pen-

dulum equilibrium when the applied voltage on the lens is zero. The separation of 117.59 μm corresponds to the data taken when the lens is at pixel number 1417, 104.77 μm to lens at pixel number 1500 and 88.5 μm to lens at pixel number 1585 respectively. As the voltage on the lens is increased, the equilibrium position shifts away from the lens, implying a reduction in the force of attraction from the lens until the voltage reaches between 55 to 60 mV beyond this voltage the attraction increases again. Hence, the electrostatic forces are minimum around this voltage range.

Thus, from the small amplitude data, we have an idea of the magnitude of the electrostatic forces acting on the pendulum. The distance and the voltage ranges over which observations are to be carried out in order to fully characterize the electrostatic and other forces are now clear.

Large amplitude oscillations

Another mode in which data is obtained is by sampling the potential in the regions that are very close to the point where the potential becomes completely attractive. As we observed in the small amplitude data, the electrostatic force on the pendulum is the least when the voltage is about 57 mV on the lens. This then means that at angular distance of about 1×10^{-3} radians, the potential in the region between the lens and the pendulum would be considerably different from the harmonic potential of the fibre, but will still have a minimum. Thus, if the pendulum is made to execute oscillations of very large amplitude about 2×10^{-3} radians, the oscillations of the pendulum will show marked anharmonicity especially during one half of the cycle.

The period and the equilibrium position of the pendulum in this case will be different from those in the small amplitude case. The $\dot{\theta}$ and $\ddot{\theta}$ of the pendulum will show marked change between the two halves of the cycle. Since in this mode we are sampling the potentials in regions that are reasonably far away from the lens - separations > 20 μm,

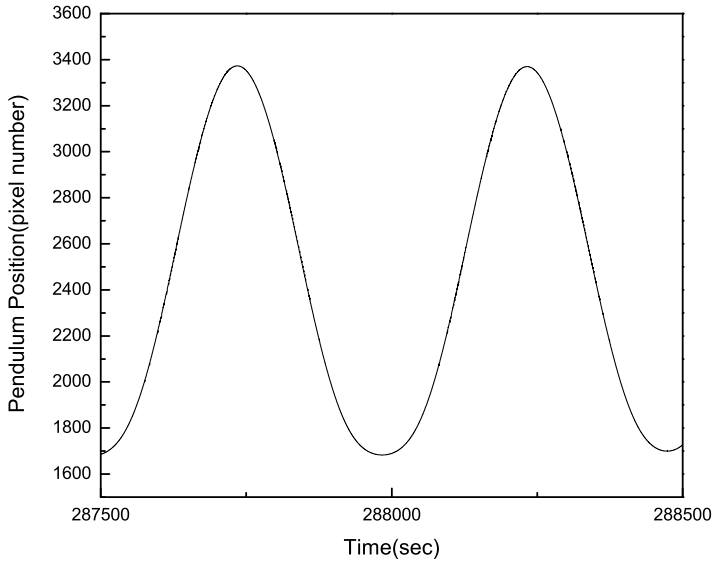

Fig. 5.8: The raw data showing large amplitude oscillations of the pendulum when an voltage of 75 mV was applied to the lens

the dominant force on the pendulum will be the electrostatic force. Thus, quantitative information about the electrostatic forces can be obtained from this data.

The amplitude of the pendulum is increased using the capacitor plates that were described in Chapter 2. The amplitude of the torsional oscillations of the pendulum can be controlled by applying appropriate voltage on these plates. The pendulum is made to oscillate such that it approaches to within 1×10^{-3} radians from the lens for about 10 cycles. Data is taken at 0.16 sec time intervals. The time period of these oscillations varies from 400 sec to 600 sec depending on the voltage present on the lens. The angular position of the pendulum is recorded in units of pixel numbers of the CCD. Fig. 5.8 displays a portion of the large amplitude data taken and shows the asymmetry in the oscillations on the side closer to the lens (lens is at about pixel number 1580 for the data shown). To fully understand the electrostatic forces, the large amplitude data is obtained by applying voltages on the lens. Since we expect the minimum in the force to be at about $V_{ap} = 57$ mV, voltages starting from 50 mV to 100 mV are applied on the lens in 5 mV steps.

Further analysis of these oscillations to comprehend the electrostatic forces will be

presented later in this chapter.

Pendulum 'falling' onto the lens

The Casimir force falls very rapidly with the distance from the lens. In order to measure Casimir force, the potential very close to the lens has to be studied. But in this region, the potential is highly attractive and the pendulum cannot oscillate. Instead, it is pulled steadily towards the lens until it hits the lens and bounces away from it. Thus, to quantify Casimir force, data is taken as the pendulum falls on to the lens.

The initial velocity of the fall is controlled by using the capacitor plates that damp the angular oscillations. By applying appropriate voltages to the capacitor plates, the pendulum is first pulled over the potential hill onto the attractive region of the potential. As the pendulum falls towards the lens, it is stopped and mildly pulled away from the lens. The velocity away from the lens is not sufficient for the pendulum to go over the potential hill again, but it just falls back onto the lens after moving away from it for a short distance. Thus, the fall data is available with zero initial velocity. [Fig.5.9]

Data is taken by making the pendulum fall onto the lens several times. The angular position of the pendulum θ is recorded every 0.16 sec as the pendulum falls. The voltage on the lens is also varied as in the case of the large amplitude oscillations. Fig. 5.9 shows the raw data of a single 'fall' of the lens on to the pendulum when a voltage of 80 mV is applied to the lens. The analysis of this data to extract information about the Casimir force is presented in the next section.

5.3 Analysis:

The angular position data obtained from the autocollimator, has to be analyzed to gain knowledge about the forces acting on the pendulum. The strategy followed

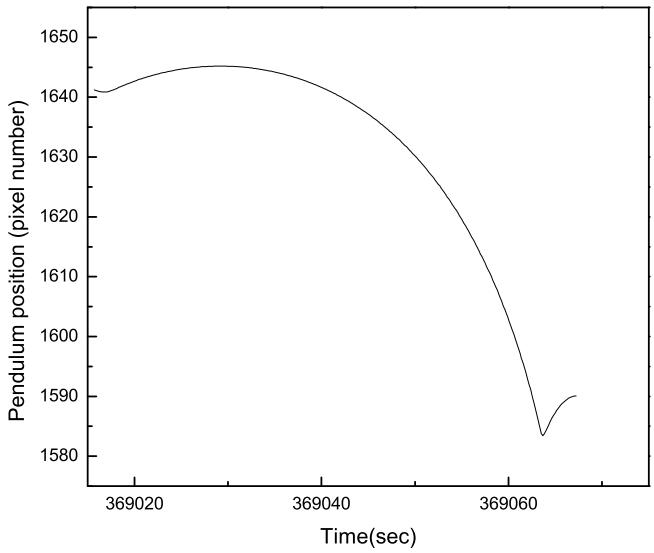

Fig. 5.9: The raw data showing the pendulum 'falling' onto the lens after being pulled away from it using the capacitor plates. For this data the lens is at pixel number of about 1580 and a voltage of 80 mV is applied to it.

involves the use of $\ddot{\theta}$ as a function of θ to extract information about the forces. Thus, the first step in the analysis is to convert the $(t-\theta)$ data to $(\theta-\ddot{\theta})$ map. This is then further analyzed to extract information about the force. The analysis of the data acquired as described in the previous sections is presented in this section.

Large amplitude oscillation:

The large amplitude oscillations of the pendulum give us information about the forces acting on the pendulum at separations > 20 μm from the lens. The electrostatic forces are the dominant forces at these separations.

An angular position plot of large amplitude oscillation is shown in Fig. 5.8. As a first step in the analysis of the data, the angular position is converted to angular separation, θ, taking into account the lens position during the run of the experiment. This data is filtered to remove θ values that have $> 3\sigma$ errors in them. These errors arise due to the non-uniformities in the CCD pixels. The θ values with errors $> 3\sigma$

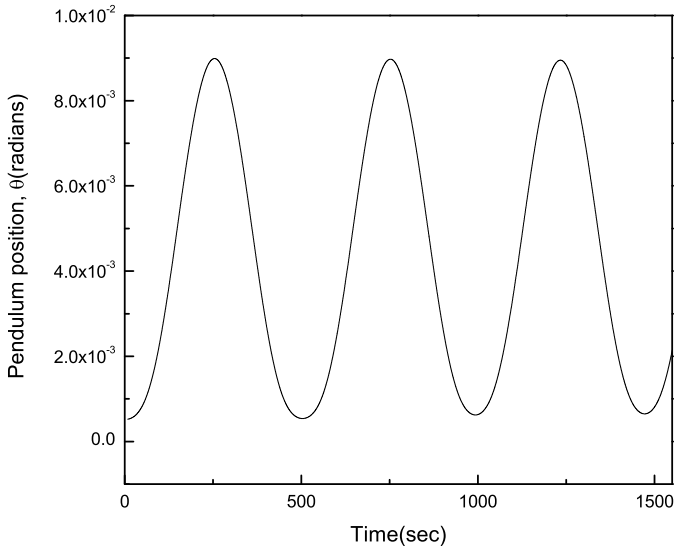

Fig. 5.10: Plot of smoothened $t-\theta$ Data taken with a voltage of 75 mV on the lens

are replaced by the mean θ of the neighbouring 10 points. Since the time period of the pendulum is much larger than the sampling time between points, the change in θ within this 10 point interval of 1.6 sec can be considered linear.

The $(t-\theta)$ data thus generated is further smoothened using a third order polynomial fit for every 51 points. This is a small fraction of the total of about 2500 points available per cycle of the pendulum. The central, 26^{th} point of this set is replaced by the smoothened θ obtained from the fit. A plot of the smoothened data is shown in Fig. 5.10. The next step is to obtain the angular velocities and accelerations. For this, in every 51 points of the smoothened $(t-\theta)$ data, the time at the 26^{th} point t_{26}, is subtracted from all ts. This is then fitted with a second order polynomial in t. Let this be $u+vt+wt^2$. Here u would be θ at $t=0$ which is the θ of the 26^{th} point. The angular acceleration and velocity are then calculated as follows,

$$\theta(t) = u+vt+wt^2, \tag{5.42}$$

$$\dot{\theta} = v+2wt, \quad \text{at } \theta=u, \tag{5.43}$$

$$\ddot{\theta} = 2v, \quad \text{at } \theta=u. \tag{5.44}$$

This is done for entire $(t-\theta)$ data by sliding over every consecutive 51 points. Thus,

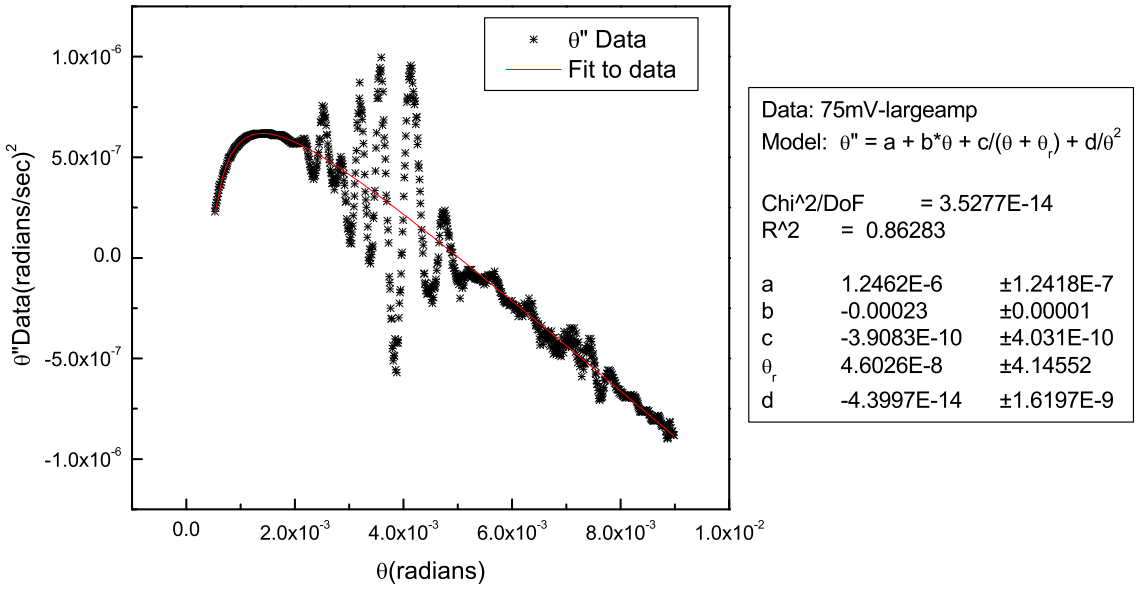

Fig. 5.11: $(\theta - \ddot{\theta})$ for large amplitude oscillations data taken with a voltage of 75 mV on the lens and a fit to the data

we get $\dot{\theta}, \ddot{\theta}$ at every θ. Since the $(t - \theta)$ is cyclic, the $(\theta - \dot{\theta})$ and $(\theta - \ddot{\theta})$ data will also be cyclic. The cycles are overlapped by ordering according to increasing θ. These are then averaged over a θ range of 1×10^{-5} radians. Thus, for every set of $(t - \theta)$ data, a set of $\theta, \dot{\theta}, \ddot{\theta}$ data is generated.

Fig. 5.11 shows a plot of $(\theta - \ddot{\theta})$ data. The 'asterisks' mark the data points obtained as described above. Almost periodic errors are present even after the averaging as can be seen. The error is large when the velocity of the pendulum is large and is perhaps caused by systematic errors in the timing generated by the PC. The PC runs Windows operating system and hence interrupts from the operating system could lead to non-uniformity in the time difference between 2 successive data acquisitions.

The linear portion of the plot, for $\theta > 4 \times 10^{-3}$ radians represents the force due to the fibre. The sharp curvature in the plot for $\theta < 2 \times 10^{-3}$ radians is predominantly caused by the electrostatic forces. To study these forces, described in §1 of this chapter, we

fit an equation of the form,

$$\ddot{\theta} \;=\; a + b\,\theta + \frac{c}{\theta+\theta_r} + \frac{d}{\theta^2}. \tag{5.45}$$

The coefficient b represents the force due to the fibre and c the voltage dependant electrostatic forces. The coefficient d is an estimate of the Casimir force at these separations. It was seen that the fitting coefficients θ_r and d, for this data at large separations, do not play a major role in determining the best fit parameters. The values of coefficients a, b and c do not change much even if θ_r and d are made zero. Parameters a and c change by about 0.001% while parameter b does not change at all. A fit of this form to the $(\theta - \ddot{\theta})$ data when a voltage of 75 mV is applied to the lens is shown in Fig. 5.11.

Tab. 5.1: Table of coefficients of the fit to $\theta - \ddot{\theta}$ for large amplitude oscillation data obtained with various voltages applied to the lens

Voltage on lens	Fit parameters				
(volts)	a	b	c	θ_r	d
0.05	1.278×10^{-6}	-2.3×10^{-4}	-5.0136×10^{-10}	-6.3578×10^{-7}	-1.198×10^{-13}
0.055	1.2433×10^{-6}	-2.3×10^{-4}	-4.2532×10^{-10}	-6.7919×10^{-8}	-1.5841×10^{-13}
0.06	1.2636×10^{-6}	-2.3×10^{-4}	-4.4659×10^{-10}	1.3246×10^{-8}	-9.2951×10^{-14}
0.065	1.2612×10^{-6}	-2.3×10^{-4}	-4.0365×10^{-10}	-5.4028×10^{-8}	-9.0942×10^{-14}
0.07	1.2657×10^{-6}	-2.3×10^{-4}	-4.2719×10^{-10}	9.3035×10^{-8}	-3.79×10^{-14}
0.075	1.2462×10^{-6}	-2.3×10^{-4}	-3.9083×10^{-10}	4.6026×10^{-8}	-4.3997×10^{-14}
0.08	1.2495×10^{-6}	-2.3×10^{-4}	-4.0554×10^{-10}	-3.0652×10^{-8}	-3.1951×10^{-14}
0.085	1.2525×10^{-6}	-2.3×10^{-4}	-4.1011×10^{-10}	1.0153×10^{-7}	-1.8389×10^{-14}
0.09	1.2543×10^{-6}	-2.3×10^{-4}	-4.3337×10^{-10}	5.0976×10^{-7}	-1.1825×10^{-14}
0.095	1.256×10^{-6}	-2.3×10^{-4}	-4.7088×10^{-10}	-1.1626×10^{-6}	-6.8344×10^{-15}
0.1	1.246×10^{-6}	-2.3×10^{-4}	-5.1666×10^{-10}	2×10^{-5}	-1×10^{-16}

Data obtained with voltages in the range of $50 - 100$ mV are analyzed following the same procedure. The fit parameters obtained for these data are tabulated in Table 5.1.

As seen from the table, the coefficient b is a constant independent of the voltage on the lens as is to be expected. Its value of -2.3×10^{-4} compares well with the value of -2.46×10^{-4} estimated from the time period of the pendulum in the absence of the lens. A plot of the coefficient, c, which describes the voltage and charge dependent forces as a function of voltage applied to the lens is shown in Fig. 5.12. The figure also contains a parabola fitted to the data. The minimum in the electrostatic force is determined by the balance between the charge dependent and the charge independent forces. The figure shows that c is minimum for an applied voltage of 75 mV. Thus, the background electrostatic forces acting on the pendulum at these separations are balanced when a voltage of 75 mV is present on the lens.

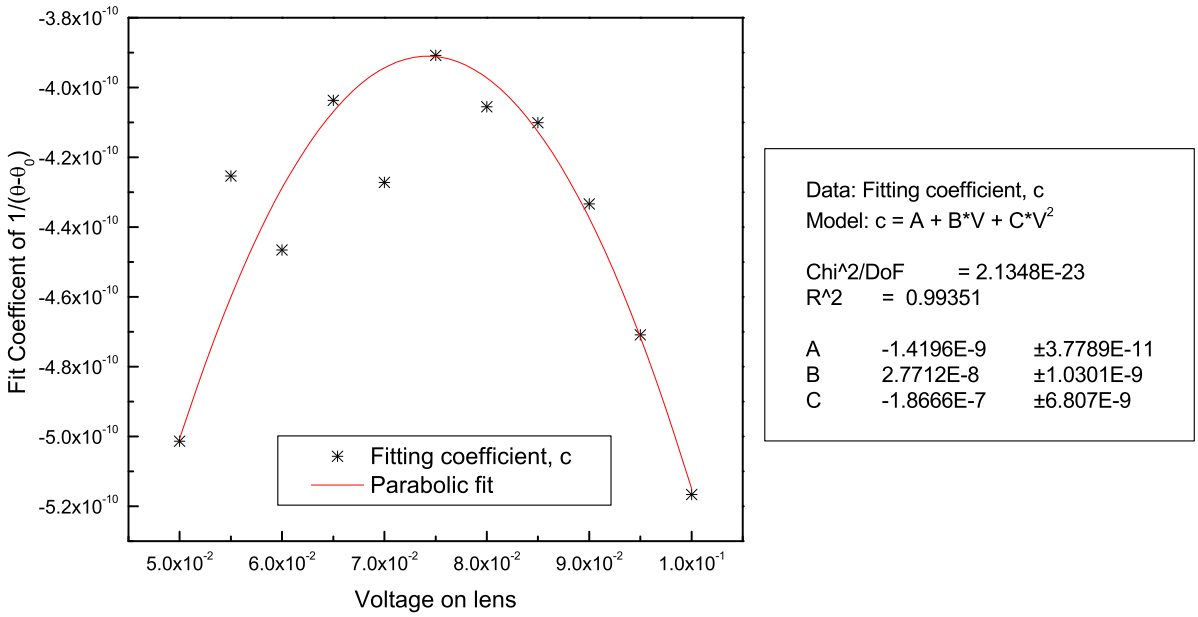

Fig. 5.12: A plot of the fitting parameter c, as a function of voltage on the lens calculated for the large amplitude oscillations of the pendulum.

Fall Data:

The other kind of data that was acquired is the data as the pendulum fall on the lens from separations of < 15 μm. The electrostatic forces and the Casimir force together

determine the motion of the pendulum in this region.

A sample plot of this data is shown in Fig. 5.9. The angular acceleration is estimated by fitting a second order polynomial as before to every 10 points in the $(t-\theta)$ data. The $(\theta-\ddot{\theta})$ are given by Eqn. 5.44. Here too the data from multiple falls is combined by ordering them increasing in θ. Data is averaged over a θ range of 1×10^{-5} radians. Fig. 5.13 shows a plot of $(\theta-\ddot{\theta})$ for the fall data with a voltage of 80 mV on the lens. The 'asterisks' mark the data points obtained as described above. This data is fitted with Eqn. 5.45. The coefficients a, b, c and d correspond to the various forces acting on the pendulum as mentioned earlier. The presence of parameters θ_r and d is essential for this fit. In the absence of d, the curvature in the data is not matched by the form of the fitting curve. Thus this data has signature of the Casimir force.

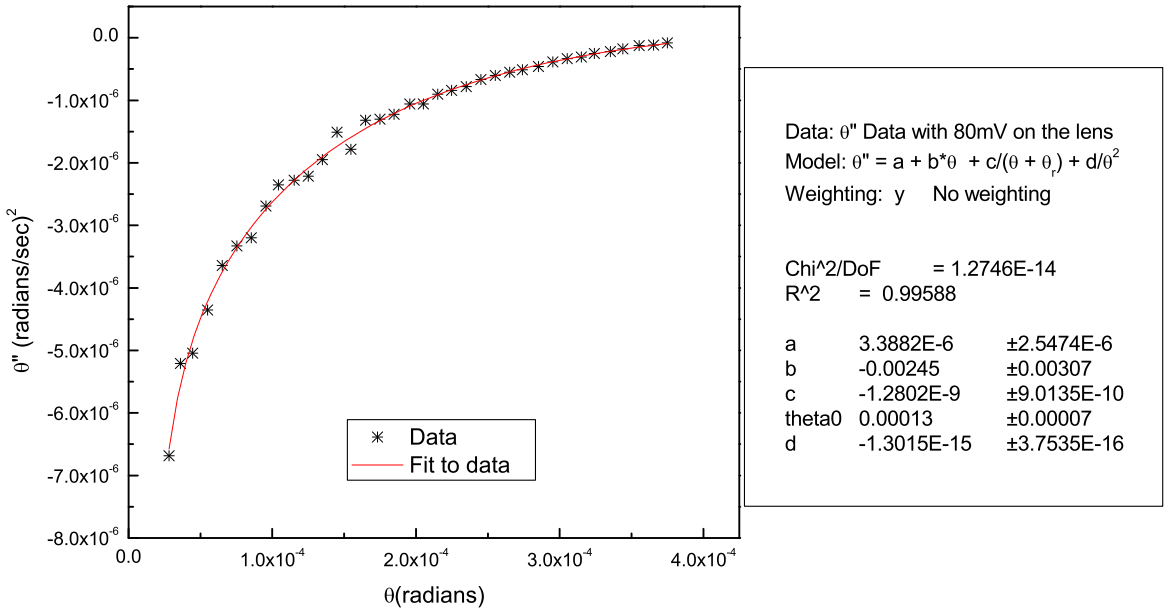

Fig. 5.13: $(\theta-\ddot{\theta})$ for fall data taken with a voltage of 80 mV on the lens and a fit to the data.

The electrostatic and fibre forces have to be subtracted from this data in order to study Casimir force. For this, the angular accelerations obtained using the fitting parameters $\ddot{\theta}(fit)$, are subtracted from the observed accelerations, $\ddot{\theta}(obs)$ to get the

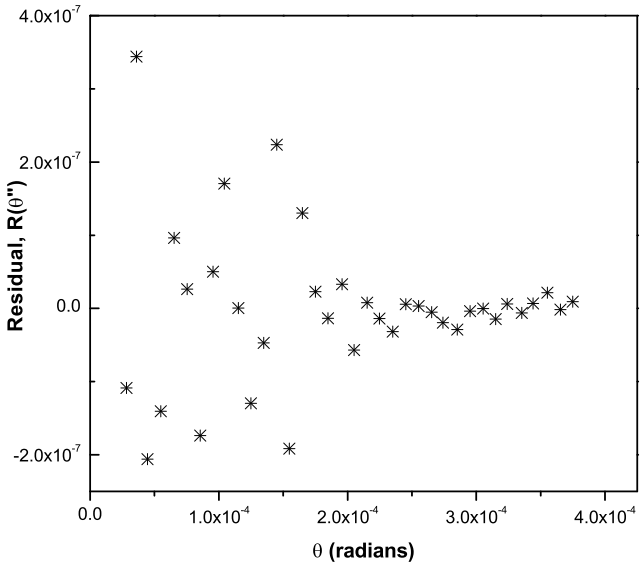

Fig. 5.14: Plot of the residual $R(\ddot{\theta})_i$, for the data with a voltage of 80 mV on the lens.

residuals,$R(\ddot{\theta})$ as a function of θ. Thus, for each θ_i in the data set, $R(\ddot{\theta})_i = \ddot{\theta}(obs)_i - \ddot{\theta}(fit)_i$. A plot of these residuals is shown in Fig. 5.14 . To minimize errors, $R(\ddot{\theta})$ are averaged over a θ range of 5×10^{-5} radians to get average residuals and error in the residuals as function of average θ as follows,

$$\langle\theta\rangle_i = \frac{\sum_{j=1}^{n} \theta_{ij}}{\sum_{j=1}^{n} 1} \tag{5.46}$$

$$\langle R(\ddot{\theta})\rangle_i = \frac{\sum_{j=1}^{n} R(\ddot{\theta})_{ij}}{\sum_{j=1}^{n} 1} \tag{5.47}$$

$$\triangle R_i = \frac{\left\{\sum_{j=1}^{n} \left(\langle R(\ddot{\theta})\rangle_i - R(\ddot{\theta})_{ij}\right)^2\right\}^{\frac{1}{2}}}{n}, \tag{5.48}$$

where n is the number of points with the θ range of 5×10^{-5} radians.

The average $1/\theta^2$ term of the fit has to be added to the $\langle R(\ddot{\theta})\rangle_i$ to get the remanent angular accelerations with only the electrostatic and fibre background forces removed, $\ddot{\theta}_i(\langle\theta\rangle_i)$. Thus, $\ddot{\theta}_i(\langle\theta\rangle_i) = \langle R(\ddot{\theta})\rangle_i + \langle\frac{d}{\theta^2}\rangle = \langle R(\ddot{\theta})\rangle_i + \frac{d}{\theta_{min,i} * \theta_{max,i}}$, where $\theta_{min,i}$ and $\theta_{max,i}$ are the minimum and maximum value respectively of θ in the range i that was averaged. Fig 5.15 shows a plot of remanent angular acceleration, $\ddot{\theta}_i(\langle\theta\rangle_i)$ as a function of $\langle\theta\rangle$ with a voltage of 80 mV on the lens. $\triangle R_i$, represents the error bars on the data.

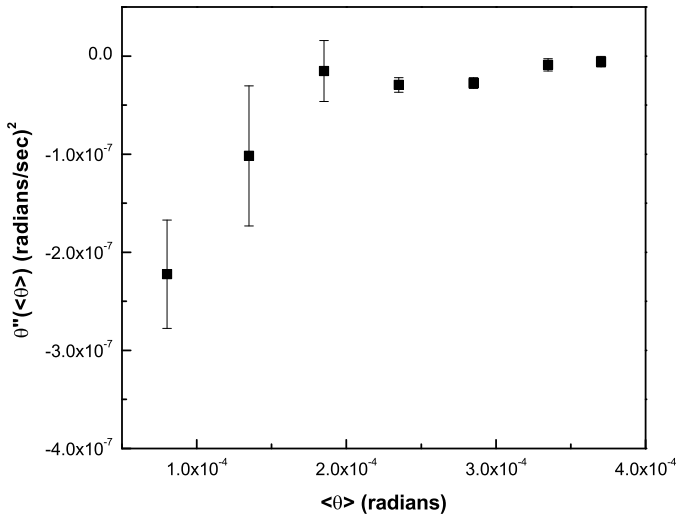

Fig. 5.15: Plot of $\ddot{\theta}_i(\langle\theta\rangle)$, for the data with a voltage of 80 mV on the lens.

The estimated $(\theta, \ddot{\theta})$ data, obtained with voltages V_α in the range of $70-100$ mV on the lens were analyzed following the same procedure to get the background subtracted, $\ddot{\theta}_i(\langle\theta\rangle, V_\alpha)$ and $\triangle R_i(V_\alpha)$. The fit parameters obtained are tabulated in Table 5.2. The average value of the coefficients obtained in the fit and the errors in them are tabulated in Table 5.3. A plot of $\ddot{\theta}_i(\langle\theta_i\rangle)$ as a function of $\langle\theta\rangle_i$ for three such data sets is shown in Fig. 5.16. A weighted average of the remanent acceleration from various voltages is obtained using,

$$\text{Average Remanent Acceleration, } \langle\ddot{\theta}(\langle\theta\rangle_i)\rangle = \frac{\sum_\alpha \ddot{\theta}_i(\langle\theta\rangle_i, V_\alpha)\frac{1}{\triangle\ R_i^2(V_\alpha)}}{\sum_\alpha \frac{1}{\triangle\ R_i^2(V_\alpha)}} \quad (5.49)$$

$$\triangle(\langle\theta\rangle_i) = \frac{\{\triangle\ R_i^2(V_\alpha\}^{1/2}}{\sum_\alpha 1} \quad (5.50)$$

A plot of this is shown in Fig. 5.17.

5.4 Discussion of results

The reduced data in Fig. 5.17 is the force of interaction between the spherical surface and the flat disc after subtracting the electrostatic forces, fibre force and constant

Tab. 5.2: Table of coefficients of the fit to $\theta - \ddot{\theta}$ for fall data obtained with various voltages applied to the lens

Voltage on lens (volts)	Fit parameters				
	a	b	c	θ_r	d
0.07	2.5782×10^{-6}	-1.13×10^{-4}	-1.1153×10^{-9}	1.0×10^{-4}	-8×10^{-16}
0.075	2.7099×10^{-6}	-1.59×10^{-4}	-1.0454×10^{-9}	8.0×10^{-5}	-8×10^{-16}
0.08	3.3882×10^{-6}	-2.45×10^{-4}	-1.2802×10^{-9}	1.3×10^{-4}	-1.3015×10^{-15}
0.085	2.1666×10^{-6}	-1.09×10^{-4}	-8.2853×10^{-10}	8.0×10^{-5}	-1.0614×10^{-15}
0.09	2.9664×10^{-6}	-1.9×10^{-4}	-1.3116×10^{-9}	1.2×10^{-4}	-8×10^{-16}
0.095	2.962×10^{-6}	-2.1×10^{-4}	-1.1186×10^{-9}	1.3×10^{-4}	-1.0701×10^{-15}
0.1	1.3246×10^{-6}	-2.6×10^{-4}	-5.7839×10^{-10}	7.35×10^{-5}	-9×10^{-16}

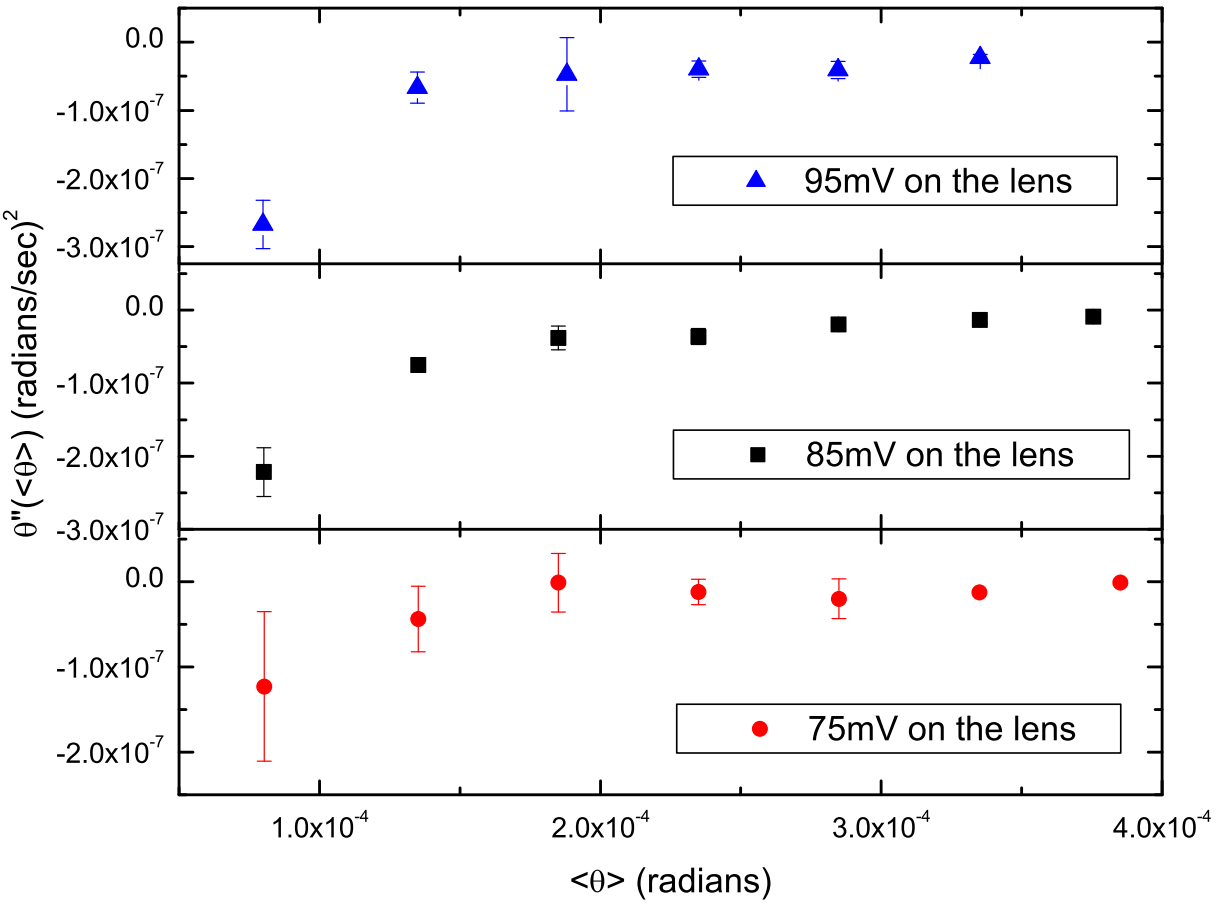

Fig. 5.16: Plot of $\ddot{\theta}_i(\langle\theta\rangle)$, for the data with a voltages of 75 mV, 85 mV and 95 mV on the lens.

Tab. 5.3: Table of average coefficients of the fit to $\theta - \ddot{\theta}$ for fall data obtained with various voltages applied to the lens

Fit parameter	Average value	Error in estimation
a	2.585×10^{-6}	2.541×10^{-7}
b	-0.00184	2.2625×10^{-4}
c	-1.014×10^{-9}	8.87796×10^{-11}
θ_r	1.01929×10^{-4}	9.35569×10^{-6}
d	-9.61857×10^{-16}	7.22763×10^{-17}

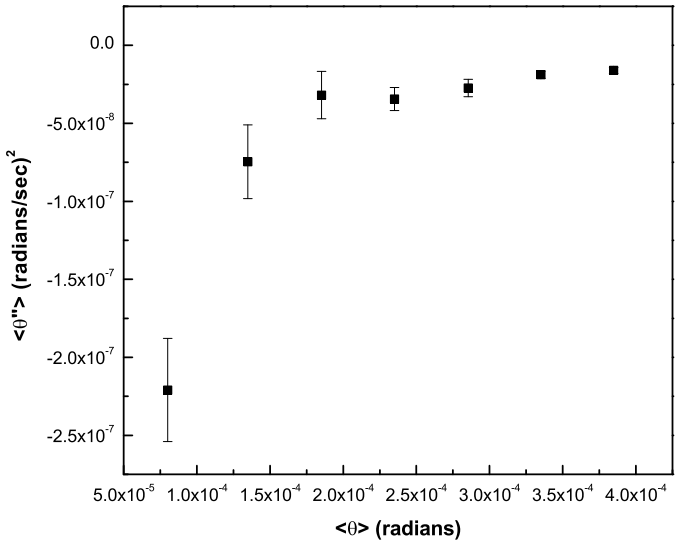

Fig. 5.17: Plot $\langle \ddot{\theta}(\langle \theta \rangle_i) \rangle$ estimated from the fall data, is shown.

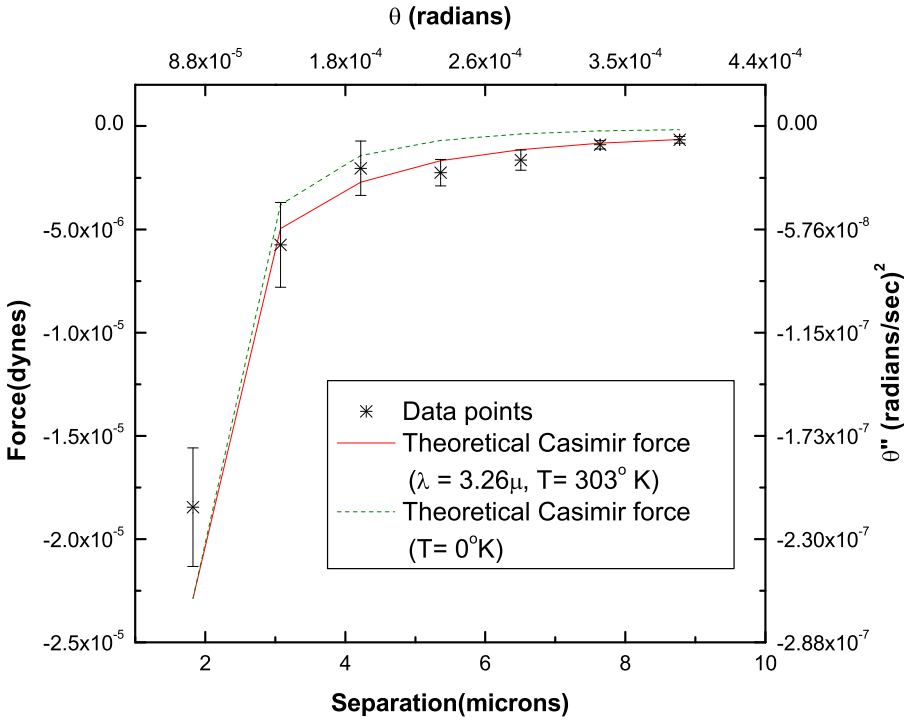

Fig. 5.18: Plot of force between the lens and the pendulum disc estimated from the fall data(stars) is shown along with theoretically estimated Casimir force. The solid lines represents the Casimir force estimated assuming $\lambda = 3.26$ μm and the dashed line represents the zero temperature Casimir force.

(distance independent) forces and offset. This measured force plotted along with theoretically expected Casimir force is shown in Fig. 5.18. The 'asterisks' represent the remanent force obtained after the subtraction of the electrostatic and the fibre background forces as described in the previous section. The Casimir force is estimated using Eqns. 5.18, 5.19 with $\lambda = 3.26$ μm consistent with the theoretical estimates of Genet, Lambrecht and Reynaud [17]. This is averaged over a range of 5×10^{-5} radians in separation θ and overploted (solid line). The Casimir force between the lens and the parallel plate without including finite temperature corrections is also averaged and plotted (dashed line). The error in the measurements at separations > 4 μm are less as compared to that at closer separations. This is because the pendulum spends less time in the region close to lens due to larger 'fall' velocity, and hence there are less number of data points in this region when θ is recorded as a function of t. There is an offset of the measured force from the theoretically expected force even in the region

where the errors are small. This offset is a small fraction of the error on the constant term 'a' in the fit, Eqn.5.45, to the entire data. If the data is normalized to the finite temperature Casimir force at 9 μm by adding a constant offset to all the data points, the measured force agrees with the theoretically calculated finite temperature Casimir force within the statistical errors of the data. The required offset of 8.4×10^{-9} (radians/sec)^2 or 3.61×10^{-7} dynes is $\sim 1/30^{th}$ of the error in the estimation of the constant coefficient from the fit, which is 2.541×10^{-7} (radians/sec)^2 [Table 5.1]. Also this offset is of the order of the expected residual gravitational force on the pendulum due to the lens [see §5.1.1]. The deviation of the data from the finite temperature Casimir force around separations of 4 μm is due to the fact that we have imposed a strict cut-off for the change over from zero temperature to finite temperature theory at $\lambda = 3.26$ μm. The actual force will gradually change from the dependance of $1/z^2$ to $1/z^3$ around $z = 3.26$ μm. Also there will be about 10% reduction in the estimated Casimir force through out the range due to finite conductivity corrections.

Thus, the measured force is consonant with the presence of a force that is $\sim 1/z^2$, viz., finite temperature Casimir force.

References

[1] E. G. Adelberger, B. R. Heckel, and A. E. Nelson. Tests of the Gravitational Inverse-Square Law. *ArXiv High Energy Physics - Phenomenology e-prints*, July 2003.

[2] J. Blocki et al. . *Ann. Phys. (N.Y.)*, 105:427, 1977.

[3] G. Bressi et al. Measurement of the Casimir Force between Parallel Metallic Surfaces. *Phys. Rev. Lett*, 88:041804–1, 2002.

[4] H. B. Chan et al. Quantum Mechanical Actuation of Micromechanical Systems by the Casimir Force. *Science*, 291:9, 2001.

[5] B. V Derjaguin. The Force Between Molecules. *Sci. Am.*, 203:47, 1960.

[6] B. V Derjaguin and J. J. Abrikossova. *Disc. Faraday Soc.*, 18:33, 1954.

[7] C. Genet, A. Lambrecht, and S. Reynaud. Temperature dependence of the Casimir effect between metallic mirrors. *Phy.Rev. A*, 62:012110, July 2000.

[8] S. K. Lamoreaux. Demonstration of the Casimir Force in the 0.6 to 6 μ Range. *Phys. Rev. Lett*, 78:5, 1997.

[9] U. Mohideen and A Roy. Precision Measurement of the Casimir Force from 0.1 to 0.9 μm Range. *Phys. Rev. Lett*, 81:4549, 1998.

[10] W. R Smythe. *Static and Dynamic Electricity.* McGraw Hill, 1939.

[11] M. J. Sparnaay. Attractive Forces Between Flat Plates. *Nature*, 180:334, 1957.

[12] C. C. Speake. Forces and force gradients due to patch fields and contact-potential differences. *Classical and Quantum Gravity*, 13:291–, November 1996.

[13] C. C. Speake and C. Trenkel. Forces between Conducting Surfaces due to Spatial Variations of Surface Potential. *Physical Review Letters*, 90:160403, 2003.

[14] P. H. G. M van Blokland and J. T. G. Overbeek. van der Waals Forces Between Objects Covered with Chromium Layer. *J. Chem. Soc. Faraday Trans. 72*, 72:2637, 1978.

6. COMPARISON OF EXPERIMENTS ON CASIMIR FORCE

Abstract: A brief review of various experiments performed to study the Casimir effect will be presented. We then compare the results from the recent experiments with our results. The first ever detection and measurement of finite temperature corrections to Casimir force in our experiment is highlighted.

6.1 Experiments to Study Casimir force

Experimental studies on Casimir force started half a century ago, a few years after Casimir predicted the existence of the force in 1948 [3]. A historical overview of the experiments was presented in the first chapter. Extensive reviews may be found in [4, 5]. We now discuss the details about some of the pioneering experiments measuring Casimir force.

Overbeek and Sparnaay [15] were the first to attempt to measure the Casimir force. They tried to measure the force between two parallel polished flat glass plates with a surface area of 1 cm^2, in the distance range of 0.6 μm to 1.5 μm. The distance was sometimes made 0.2 μm. The force was measured using a spring balance. The displacement of the spring was measured by means of a capacitive method. The measurements at 1.2 μm, 'pointed to the existence of a force which were of the expected order of magnitude' [17]. The hygroscopic behaviour of the glass (quartz) surfaces and presence of dust particles presented difficulties.

Results in the distance range 0.1 μm to 1.0 μm with several different materials were first obtained by Derjaguin and Abrikossova [8, 7]. They measured the force between plano-convex fused silica lens and a flat attached to a knife-edge balance. The deflection of the balance was observed optically. A current in proportion to the deflection of the balance from its mean position was generated and passed though a coil. The coil was pivoted between the pole pieces of a magnet. The magnet and the coil were mounted such that the current flowing through the coil produced a turning force on the balance opposite to that due to attractive molecular forces and kept the balance from turning. This current was, thus, a measure of the force. The separation between the lens and a flat was measured using "Newton's rings". They could show that Casimir's formula provided a better fit to the experimental data in contrast to London's theory for the van der Waals forces. They also did experiments with two quartz plates, quartz and chromium plates and with crystals made of thallium-bromide and thallium iodide. It was these experiments that, in a way, motivated Lifshitz to derive a macroscopic theory of molecular forces [4].

Sparnaay [16] repeated his measurements with metal plates in 1957. He measured the force between chromium plates and chromium steel plates. The measured scheme was similar to the previous experiment with a spring balance of sensitivity between $(0.1 - 1) \times 10^{-3}$ dynes. The distance was varied between 0.3 μm and 2 μm. The measurements did not 'contradict' the expected force per unit area from Casimir's relation. But large systematic errors and electrostatic forces prevented a detailed quantitative study.

The van der Waals force between two curved mica surfaces were measured in the distance range of 1.5 nm to 130 nm by Israelachvili and Tabor [10, 9]. They measured the force between two crossed cylindrical sheets of mica with the effective contact resembling that between a sphere and a plate. The surfaces were silvered and the

distance between them was measured by observing interference patterns with white light. The force was measured by two methods. In the short distance range of 1.5 nm -20 nm a 'jump method' was used. One surface was rigidly fixed to a moveable base and the other was mounted on a cantilever spring. When the fixed surface was moved towards the cantilever, at some point - depending on the stiffness of the spring - the two surfaces jumped into contact. The measurement of this jump distance as a function of spring distance was used to measure the force of attraction. For the distance range of 10 nm - 130 nm a resonant method was used. One surface was supported on a rigid piezo-electric crystal and was set vibrating at very small amplitudes over a convenient range of frequencies. The other was supported facing it on a stiff spring. The natural frequency of the latter depended both on the spring constant and on the van der Waals forces exerted on it by the other surface. By determining the resonant frequency as a function of separation, the force law was deduced. They showed that there is a gradual transition between the non-retarded and retarded van der Waals as the separation is increased from 12 nm to 50 nm.

The next major set of improved measurements with metallic surfaces were performed by van Blokland and Overbeek [18] in 1978. They measured the forces between a lens and a flat plate coated with chromium using a spring balance at distances between 0.13 μm and 0.67 μm. Precautions were taken to characterize and eliminate electrostatic forces by careful experimentation. Precise measurement of the separation was made by measuring the lens-plate capacitance. A detailed comparison of the data with Lifshitz theory, taking into account finite conductivity effects was done before concluding that "the measured force and the calculated force are in excellent agreement". It can be considered as the first unambiguous demonstration of the Casimir force between metallic surfaces.

After couple of dormant decades, interest in the measurement of forces in the sub-millimeter range was aroused by theories that predicted the existence of new forces

in this range. The earliest of these experiments was by Lamoreaux in 1997 [24] and around the same time we started the design of our experiment [5]. The apparatus built by Lamoreaux consists of a glass plate coated with gold over copper suspended as a torsional pendulum. Its attraction towards a spherical lens also coated with copper and gold was measured for distances between 0.6 μm - 6 μm. The plate was held fixed with respect to the spherical surface by a voltage applied to two compensating capacitor plates held parallel to the 'Casimir' plate. By measuring the change in the voltage required to hold the plates parallel when the lens was moved towards the 'Casimir' plate, the Casimir force was measured. He detected and corrected for a contact potential between the lens and the plate of 250 mV. The measured Casimir force agreed with theory at the level of 5% up to separation of about 2 μm. The sensitivity of the experiment was not adequate to measure the force beyond this range.

In a later experiment, Mohideen and Roy [14] measured the Casimir force between a metallized sphere of diameter 196 μm and a flat plate for separations from 0.1 to 0.9 μm. They used the high sensitivity of an Atomic force microscope to report a statistical precision of 1% at the smallest separations. The electrostatic force due a residual voltage of 29 mV was measured and subtracted from the data.

A micromechanical actuator based on Casimir force was developed by researchers at Bell Labs [4] in 2001. The device, fabricated using standard nanofabrication techniques, consists of a 3.5 μm thick, 500 μm square heavily doped polysilicon plate freely suspended on two opposite sides by thin torsional rods. The other ends of the torsional rods were anchored to the substrate. There was a 2 μm gap between the top plate and the underlying substrate. A gold coated ball was suspended above one side of the plate, which caused the plate to tilt due to Casimir force when the plate was brought close to the ball. This tilt was determined by measuring the capacitance between the plate and the substrate accurately. A residual voltage of 30 mV was determined and compensated for. The measurements matched with Casimir force

theory at the 1% level. The errors were mainly due to the corrections for finite conductivity and surface roughness that have to be applied to the theory.

Recently, Bressi *et al.* [2] have measured the Casimir force between parallel metallic surfaces. This is the first and only precision measurement of the Casimir force in the 'parallel plate' configuration. The force was exerted between a silicon cantilever coated with chromium and a similar rigid surface and was detected by looking at the shifts induced in the cantilever frequency when the latter was approached. The motion of the cantilever was monitored by means of a fiber optic interferometer. Electrostatic force due a residual voltage of ~ -68 mV is systematically determined and corrected for. The scaling of the Casimir force with the distance between the surfaces was tested in the 0.5 μm - 3.0 μm range, and the related force coefficient was determined at the 15% precision level.

Very recently, the Casimir force between two dissimilar metals was measured by Decca *et al.* [6] in the separation range of 0.52 μm - 2.0 μm. They measure the force of attraction between a copper layer evaporated on a micro-mechanical torsional pendulum and a gold layer deposited on an Aluminium oxide sphere with 600 μm nominal diameter. The force is inferred from the deflection angle of the torsional oscillator determined by measuring the capacitance between the oscillator and two fixed electrodes. The sensitivity of the force measurement was further improved by measuring the change in the resonant frequency of the oscillator due to the presence of the sphere. Residual voltage difference of 632.5 mV was determined by experimentation and corresponds to the difference in work functions of the gold and copper layers. The experiment highlights the need for simultaneous measurement of the dielectric constant of the metallic films used for a better understanding of the Casimir force between non-ideal bodies at these separations.

6.2 Comparison of results

The Casimir force has been measured over a wide range of separation from 1.5 nm to 3 μm by various techniques. Most experiments have been performed in the sphere-plate geometry rather than in the plate-plate geometry due to stringent conditions of parallelism required in the latter. All the experiments encountered a background of strong electrostatic forces due to residual voltages present on the interacting bodies even when these are well grounded. The Casimir force for the sphere-plate geometry, depends on the radius of the sphere used and is typically much larger than the electrostatic force at sub-micron separations. But at larger separations, the measurements are dominated by the electrostatic forces, making it difficult to perform experiments in the several microns range. For example, an electrostatic contribution comparable to the Casimir force at 1 μm becomes 10 times or more stronger than the finite temperature Casimir force at 10 μm. The experiments performed thus far, have been able to detect effects due to finite conductivity and surface roughness of the metals on the Casimir force but the finite temperature correction has not been observed.

Our experiment measures the Casimir force in the separation range of 2 μm to 9 μm. This region extends well into spacings beyond $\sim$ 3.3 μm where corrections to the Casimir force due to the $\sim$ 300° K environment become significant. As expected, the data clearly indicate the presence of the effects of finite temperature. Data from recent experiments that measured the force in the sphere-plate configuration are summarized in Fig. 6.1. The figure shows the force measured in these experiments divided by $2\pi R$, where R is the radius of curvature of sphere used in the respective experiments. The results presented in this thesis are represented by the 'stars'. The data from various experiments overlap in the region where the errors are small. Our data, below 3.3 μm overlaps well with the measurements by Lamoreaux. The slope of the data represents the power of the force law obeyed by the data. Around separation of $\sim$ 4 μm the plot distinctly shows the change in slope from ~ -3 to ~ -2 within the errors of the experiments. There is a clear indication of the change-over in the Casimir force law from the zero temperature theory to that due to finite temperature

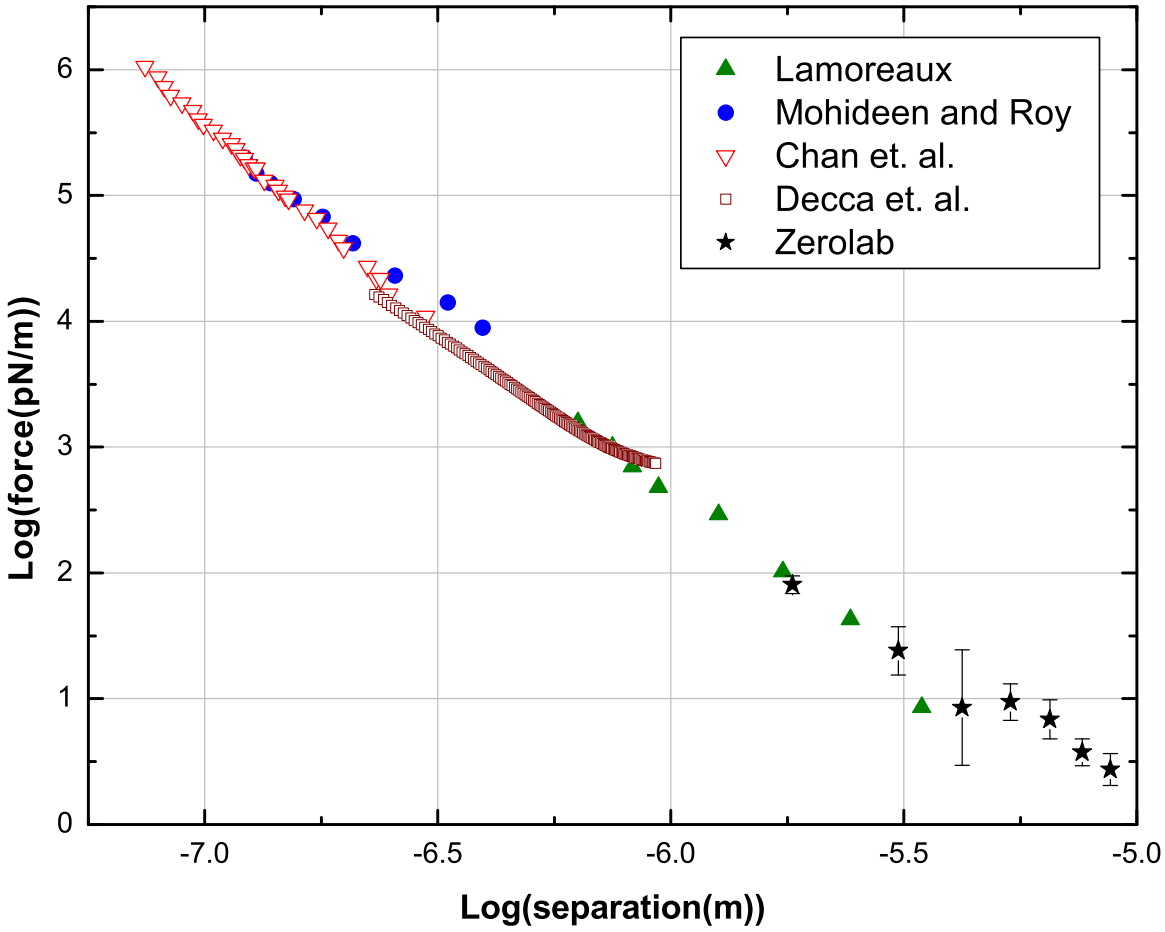

Fig. 6.1: Data from recent Casimir force experiments using the sphere-plate geometry by Lamoreaux [24], Mohideen and Roy [14], Chan *et. al.* [4], Decca *et. al.* [6] and data from our experiment.

around this separation.

In summary, our current study extends the observation of the Casimir effect up to separations of 9 μm, i.e., well into the region where finite temperature effects become important. The experiment confirms the existence of these effects and agrees with the standard theory at the 20% level.

Keeping in mind the wide-ranging importance of Casimir forces it would be useful to conduct such studies with greater accuracy and also extend them to longer separations of ~ 50 μm or more.

References

[1] M. Bordag, U. Mohideen, and V. M. Mostepanenko. New Developements in Casimir Force. *Phys. Rep.*, 353:1, 2001.

[2] G. Bressi et al. Measurement of the Casimir Force between Parallel Metallic Surfaces. *Phys. Rev. Lett*, 88:041804–1, 2002.

[3] H. B. Casimir. On the Attraction Between Two Perfectly Conducting Plates. *Proc. K. Ned. Akad. Wet.*, 51:793, 1948.

[4] H. B. Chan et al. Quantum Mechanical Actuation of Micromechanical Systems by the Casimir Force. *Science*, 291:9, 2001.

[5] R. Cowsik, B. P. Das, N. Krishnan, G. Rajalakshmi, D. Suresh, and C. S. Unnikrishnan. High Sensitivity Measurement of Casimir Force and Observability of Finite Temperature Effects. In *Proceedings of the Eighth Marcell-Grossmann Meeting on General Relativity*, page 949. World Scientific, 1998.

[6] R. Decca, D. López, E. Fischbach, and D. Krause. Measurement of the Casimir Force between Dissimilar Metals. *Phys. Rev. Lett.*, 91:050402, July 2003.

[7] B. V Derjaguin. The Force Between Molecules. *Sci. Am.*, 203:47, 1960.

[8] B. V Derjaguin and J. J. Abrikossova. *Disc. Faraday Soc.*, 18:33, 1954.

[9] Israelachvili and Tabor. The Measurement of van der Waals dispersion forces in the range 1.5 to 130nm. *Proc. R. Soc. Lond. A*, 331:39–55, 1972.

[10] Israelachvili and Tabor. Van der Waals dispersion forces-Measurements for curved mica surfaces separated by between 1.4 and 70 nm. *Nature Physical Science*, 236:106, April 1972.

[11] S. K. Lamoreaux. Demonstration of the Casimir Force in the 0.6 to 6 μ Range. *Phys. Rev. Lett*, 78:5, 1997.

[12] E. M. Lifshitz. Theory of molecular attraction between solids. *Sov. Phys. JETP*, 2:73, 1956.

[13] W. P Milonni. *The Quantum Vacuum: An Introduction to Quantum Electrodynamics*. Academic Press, Newyork, 1994.

[14] U. Mohideen and A Roy. Precision Measurement of the Casimir Force from 0.1 t0 0.9 μm Range. *Phys. Rev. Lett*, 81:4549, 1998.

[15] J. T. G. Overbeek and M. J. Sparnaay. *Proc. K. Ned. Akad. Wet.*, 54:387, 1952.

[16] M. J. Sparnaay. Attractive Forces Between Flat Plates. *Nature*, 180:334, 1957.

[17] M. J. Sparnaay. Historical Background of Casimir force. In A. Sarlemijn and M. J. Sparnaay, editors, *Physics in the Making*, North-Holland, 1989. Elsevier Science Publishers B V.

[18] P. H. G. M van Blokland and J. T. G. Overbeek. van der Waals Forces Between Objects Covered with Chromium Layer. *J. Chem. Soc. Faraday Trans. 72*, 72:2637, 1978.

7. BOUNDS ON THE STRENGTH OF NEW MACROSCOPIC FORCES AND FUTURE DIRECTIONS

Abstract: We briefly review the experimental bounds on the strength of inverse square law violating short-range interactions. The contribution of our experiment in this direction will be presented. The future scope of our experiment to test and constrain the predictions of fundamental theories will be discussed.

7.1 Constraints on new macroscopic forces

Extensions of the Standard Model predict the existence of a variety of neutral light bosons. The exchange of these will mediate forces that lead to deviations from the inverse square law of gravity at distances related to the mass of the bosons. String and M-theories that attempt to unify the fundamental forces close to the Planck scale or the theories with large extra dimensions that attempt to overcome the "hierarchy problem" by invoking unification of the fundamental forces at the TeV scale of electro-weak symmetry breaking, predict variations from the inverse square law of gravity at sub-millimeter distances. An overview of these effects was presented in Chapter 1. In general, the new macroscopic forces can be described by an addition of a Yukawa type potential term to the gravitational interaction between two point masses as given by,

$$V(r) = -\frac{GM_1M_2}{r}\left(1 + \alpha e^{-\frac{r}{\lambda}}\right) \tag{7.1}$$

where α represents the coupling strength of the interaction and λ the range. A recent review of the experimental and the theoretical status of the inverse square law tests can be found in [1]. Given this form for the potential, constraints can be placed on the parameter space of $\alpha - \lambda$ from experiments that study long-range interactions

7.1.1 Astrophysical Bounds

Astronomical tests provide the best constraint on the parameter α at distance scales $\lambda > 1$ km. These are typically obtained from observation of the Keplerian orbits of the planets and the satellites and looking for deviations from normal gravity. The measurements of precession of the lunar orbit using Lunar Laser Ranging studies provides very good constraints in the 10^8 m scale. Precession is expected due the quadrupole field of the Earth, gravitational perturbations from the other planets in the solar system and general relativistic effects. Presence of Yukawa type interactions, will add to the precession and hence limits can be placed on α after accounting for the expected sources of the precession. A summary of the constraints from astrophysical data is reproduced from [1, 15] in Fig. 7.1. In the range $\lambda < 1$ m, these limits have been surpassed by laboratory experiments [19, 22, 25]. Details on geophysical and laboratory constraints in the range $\lambda > 1$ m can be found in [23, 27] and [5]-[11].

Astronomical data can also provide evidence for the presence of extra dimensions [2]. The cooling rate of the supernovae will increase by the presence of the extra dimensions because energy from the explosion will be radiated into these dimensions as well. This would lead to the reduction in the number of neutrinos emitted from the supernovae. SN 1987A data constrains the size of the extra dimensions to < 0.7 μm when the number of extra dimensions is 2 [2, 12, 20, 21]. This does not imply that experiments at sub-millimeter scales will not observe effects due to the new dimensions. A single large dimension of size 1 mm with several much smaller extra dimensions is still allowed.

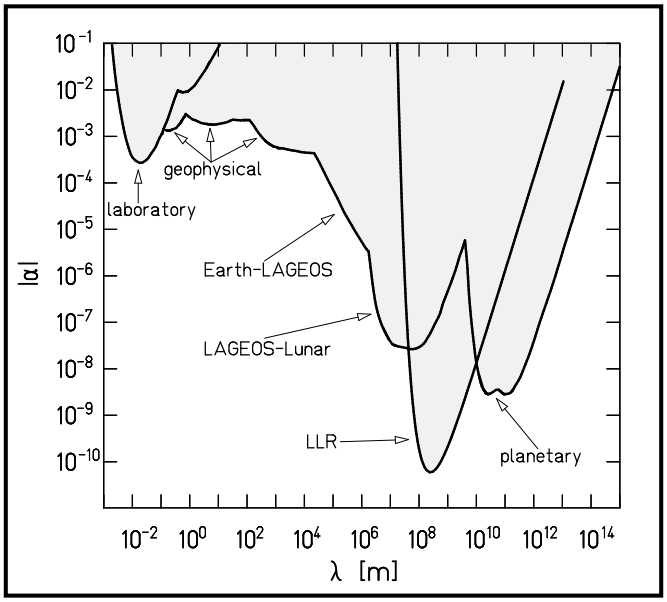

Fig. 7.1: Constraints on inverse square law-violating Yukawa interactions with $\lambda >$ 1cm. The Lunar Laser Ranging (LLR) constraint is based on the anomalous precession lunar orbit; the remaining constraints are based on Keplerian tests. This plot is reproduced from [1]. The region in the (α, λ) plane above each curve is excluded, and below each curve is allowed.

7.1.2 Bounds from Laboratory tests of Inverse square law

Constraints on α in the sub-millimeter to centimeter scales can be obtained from laboratory experiments of the Eötvos and Cavendish type. The Eötvos-type experiments test the equivalence principle by measuring the acceleration imparted by Sun, Earth or some laboratory attractor to various materials of the same mass. The presence of any additional force that couples to the material properties other than the mass will show up as a difference in the acceleration experienced by the various materials. The Cavendish-type experiments are direct tests of the Newton's inverse square law. The tightest constraints in the 1 mm to 200 μm region to date are provided by such experiments. These are shown in Fig. 7.2 (reproduced from [1]). The shaded region in the (α, λ) plane above the continuous curves is excluded.

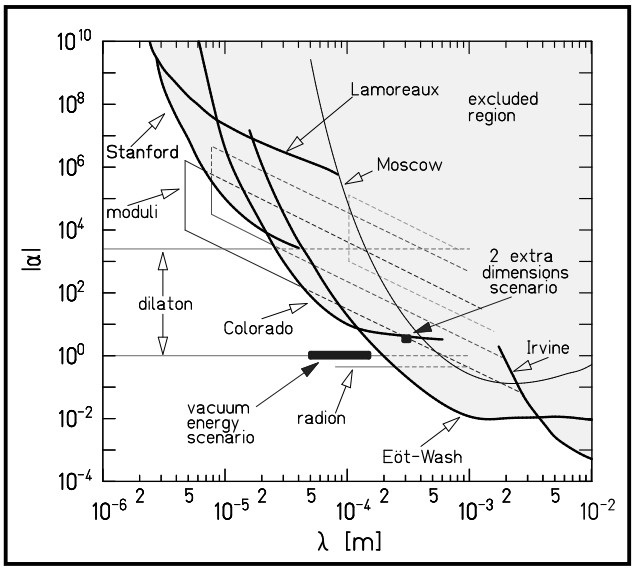

Fig. 7.2: Constraints on inverse square law-violating Yukawa interactions with 1 μm $< \lambda <$ 1 cm. This plot is from [1]. The heavy curves give experimental limits. The curve marked Irvine is a Eötvos type experiment. 'Lamoreaux' is a Casimir force measurement. The other curves are from Canvendish-type experiments. The theoretical expectations from various scenarios are also shown.

7.1.3 Bounds from Casimir Force Measurements

For distances of $\lesssim$ 0.1 mm, Casimir force measurements provide the tightest constraints. Casimir force has generated extensive experimental and theoretical interest in the last decade. Precision experiments have been performed in the distance range of about 0.1 μm to 3 μm and the theoretical correction to the Casimir force due to finite temperature, finite conductivity and surface roughness have been calculated accurately. This has enabled comparison between theory and experiment at the 1% level for the smallest separations. If the inverse square law violating interactions are present due to any of the scenarios mentioned in Chapter 1, they will show up as additional forces in the measurement. Thus, constraints on the strength of these interactions can be obtained by looking at the deviation of the measured Casimir force from the theoretically expected value and attributing it to Yukawa type inter-

actions [3, 4, 14, 13]. A plot of the constraints to date is summarized in Fig. 7.3.

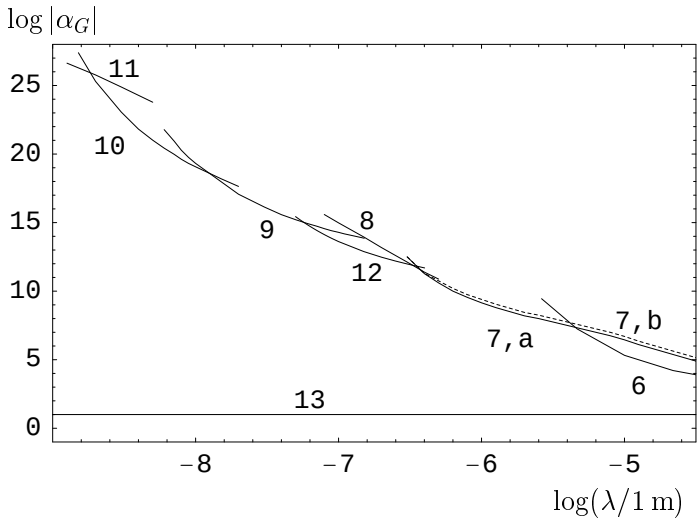

Fig. 7.3: Plot of the constraints on the Yukawa interaction parameter α from various ranges of λ reproduced from [26]. Curves 7-10, 12 follow from Casimir force measurements, Curve 11 from van der Waals force measurements. Curve 6 is from an experiment that measured deviations from Newton's law of gravity [25]. The typical prediction of extra dimensional physics is shown in Curve 13. The region, in the (α, λ) plane, above each curve is excluded and the region below each curve is allowed.

7.1.4 Estimation of bound from our experiment

Our experiment measures the Casimir force between a spherical lens and a flat disc made of 'BK7' glass (density, $\rho_v = 2.51$ g.cm^{-3}), coated with gold layer of thickness, $\delta = 1$ μm (with density, $\rho_s = 19.32$ g.cm^{-3}). The radius of curvature of the lens, $R = 38$ cm and its total height $x_{max} = 0.07$ cm. The radius of the flat disc, $l = 4$ cm and its thickness, $g = 0.4$ cm. The force due to Yukawa type potential for this

configuration is given by (see Appendix C for details),

$$\mathcal{F}_a(z) = 4\pi^2 G\alpha R\lambda^2 \left[\rho_s - (\rho_s - \rho_v)e^{-\delta/\lambda}\right] \rho_s\, \delta\, e^{-z/\lambda}, \quad \text{for } \lambda << \delta, \tag{7.2}$$

$$\mathcal{F}_b(z) = 4\pi^2 G\alpha R\lambda^2 \left[\rho_s - (\rho_s - \rho_v)e^{-\delta/\lambda}\right] \left(\, \rho_s\, \delta + \rho_v\, \lambda\, e^{-\delta/\lambda}\, \right) e^{-z/\lambda}, \tag{7.3}$$

$$\text{for } \lambda >> \delta.$$

where α and λ are parameters of the theory as defined by Eqn. 7.1.

The upper limit of constraints on the Yukawa-type interactions from our experiments can be estimated by two methods. A conservative estimate of the parameters of the Yukawa-type interactions can be obtained by assuming that all of the force, $f_{obs}(z)$ measured in our experiment is due to the Yukawa-type potential. Thus,

$$f_{obs}(z) = \mathcal{F}(z) \tag{7.4}$$

We solve Eqn. 7.4 for the observed values of the force at $z = 1.82$ μm, 3.08 μm, 4.22 μm, 5.36 μm, 6.51 μm, 7.641 μm, 8.77 μm to get α as a function of λ, we call this $\alpha_{conservative}(\lambda)$. Since the thickness of the gold coatings, $\delta = 1$ μm, we derive $\alpha_{conservative}(\lambda)$ in the range $\lambda = 2$ μm to 16 μm using Eqn. 7.3. This gives us seven possible functions for $\alpha_{conservative}(\lambda)$ corresponding to the seven separations at which we have measurements. A plot of these is shown in Fig. 7.4. The lowest values of $\alpha_{conservative}(\lambda)$ are obtained from data at $z = 8.77$ μm in the range 7 μm $\leq \lambda \leq$ 16 μm and from data at $z = 4.22$ μm in the range 3 μm $\leq \lambda <$ 7 μm.

An optimistic estimate of the parameters of the Yukawa-type interactions can be obtained from the error in the measurements of the force. Our experimental data matches with the finite temperature Casimir force between the lens and the plate within the errors of force measurement at separation $z > 4$ μm. The dominant contribution to the finite temperature Casimir force for our configurations [see Appendix A], at these separations is given by,

$$f_{cl}(z) = -\frac{\pi R A_c}{\lambda_T}\left\{\frac{1}{z^2} - \frac{1}{(z + x_{max})^2}\right\}, \quad \text{for } z > \lambda_T = 3.26\ \mu\text{m}; \tag{7.5}$$

$$A_c = \frac{\pi^2 \hbar c}{240} = 0.013 \times 10^{-18}\ \text{dyn.cm}^2. \tag{7.6}$$

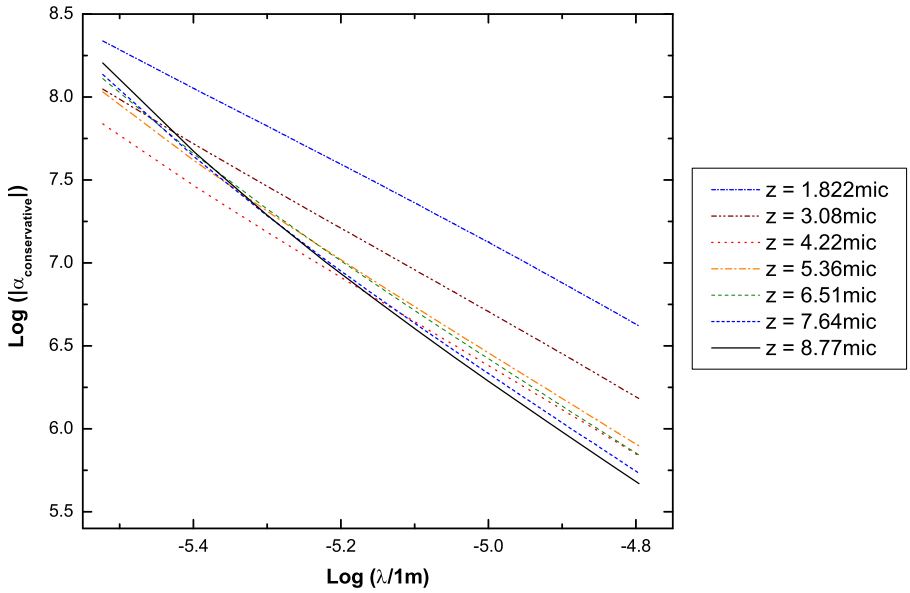

Fig. 7.4: $\alpha_{conservative}(\lambda)$ estimated from the total force measured in the experiment.

The corrections to Casimir force due to surface roughness are $< 0.6\%$ in the 4.5 μm to 9 μm range [3] and can be ignored. The finite conductivity of gold surface gives rise to a reduction in the Casimir force by 10% over the entire range of the experiment [17, 16]. Thus, the net theoretical force between the lens and the plate is given by,

$$f_{th} \quad = \quad f_{cl}(z) + \Delta_p f_{cl}(z) + \mathcal{F}(z); \tag{7.7}$$

where $\Delta_p f_{cl}(z)$ represents the corrections due to finite conductivity and $\mathcal{F}$ is the force due to hypothetical Yukawa-type interactions. This is derived in Appendix C for our geometry and is given by Eqns. 7.2 and 7.3. Thus, the Yukawa parameters can be estimated using,

$$\mid f_{th}(z) - f_{cl}(z) \mid \quad \leqslant \Delta F(z); \tag{7.8}$$

where $\Delta F(z)$ is the error in the measurement. If absolute error in our force measurement at a distance z is $e(z)$, we can solve Eqn. 7.8 assuming $\Delta F(z) = 3e(z)$. The corrections due to surface roughness become less important for larger separations and for $z < 4$ μm, the theoretical Casimir force is not strictly defined by Eqn. 7.5. We use

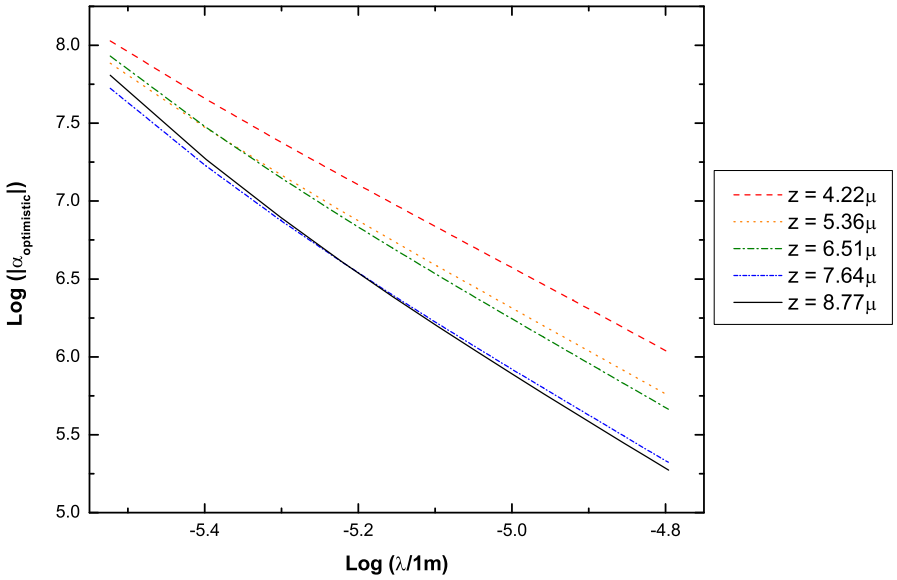

Fig. 7.5: $\alpha_{optimistic}(\lambda)$ estimated from the errors in the measurement.

the data at $z = 4.22$ μm, 5.36 μm, 6.51 μm, 7.64 μm, 8.77 μm and solve for α from Eqns. 7.7 and 7.8 in the range 3 μm $\leq \lambda \leq$ 16 μm. The values of α obtained by this method are represented by $\alpha_{optimistic}$ and are plotted in Fig. 7.5. The lowest values of $\alpha_{optimistic}(\lambda)$ are obtained from data at $z = 8.77$ μm in the range 6 μm $\leq \lambda \leq$ 16 μm and from data at $z = 7.64$ μm in the range 3 μm $\leq \lambda <$ 6 μm.

In Fig. 7.6, the lowest values of $\alpha_{conservative}(\lambda)$ and $\alpha_{optimistic}(\lambda)$ estimated as described above are plotted along with those from other experiments as presented by Mostepanenko in [26].

The lines marked 'Zerolab' are constraints as calculated from data presented in this thesis. Curve 6 is from the Canvendish-type experiment [25]. Curve $7, a$ is from the torsion balance experiment to measure Casimir force [24]. This is an upper limit of the constraint we can obtain from our experiment. The constraints from the conservative estimate are already at the level of those obtained from [24]. The optimistic estimates give the lowest values of α obtained so far in the range 3 μm $\leq \lambda <$ 6 μm and also the

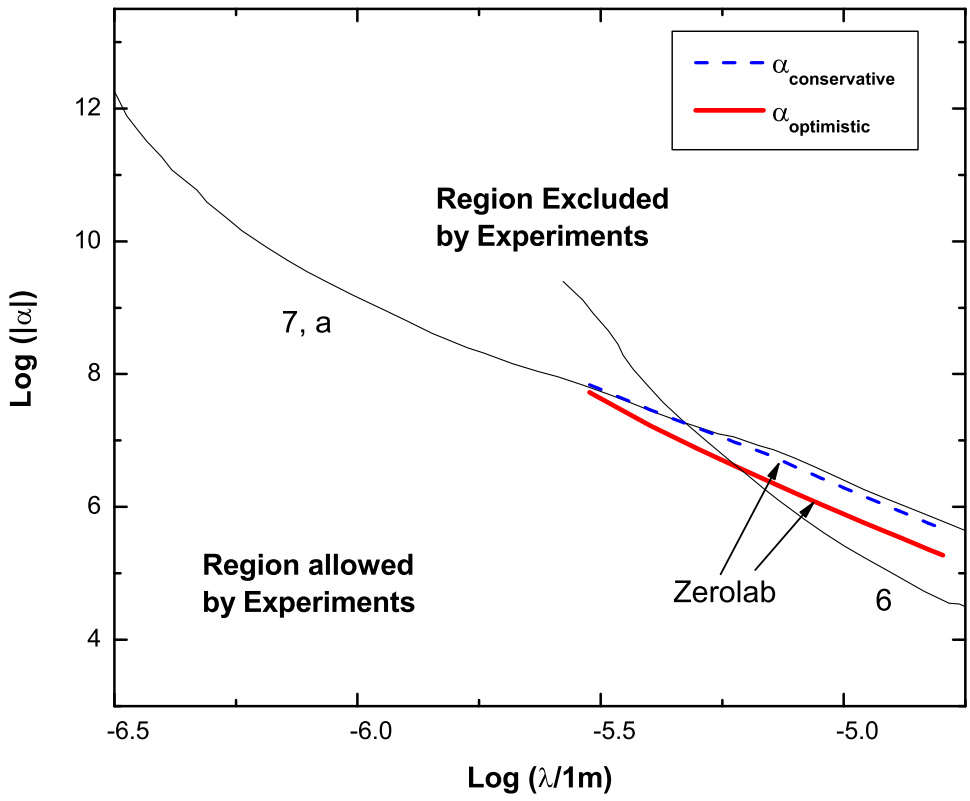

Fig. 7.6: Constraints on the inverse square law violating Yukawa interactions obtained from data presented in the thesis ('Zerolab') along with the best constraints in the same range of λ from [26]

best ever constraints from Casimir force measurements in the range 3 μm to 16 μm. By calculating the theoretical forces precisely, the constraints can be improved and also extended to shorter distances. This also means that by choosing the materials of the pendulum and attracting plate appropriately (for example, thicker coatings, or higher density materials) we may be able to improve the present constraints by more than an order of magnitude in the distance range 3 μm to 10 μm.

7.2 Future Directions

We are in the process of performing a next generation experiment, with the same general configuration but improved precision by reducing the systematic and statistical noise. In the new scheme we will perform a null experiment where the deflection of the pendulum due to the torque from the lens is balanced by the capacitive torques from a pair of metal plates located close to the disc of the pendulum (see §2.3). The voltages on capacitor plates are controlled through a servo-loop and the servo-signal is a direct measure of the torques acting on the balance. This mode of experiment has several advantages. The gain in the feed-back helps to reduce the noise in the system (see for example [18]). The statistical accuracy can be considerably improved by increasing the integration time. The errors associated with the estimation of acceleration from the limited time series data are avoided. The experiment can be performed at closer separations as well. The torque due the lens can be modulated by moving the lens back and forth, further reducing the noise in the bandwidth of the observation. Efforts are also on to characterize the background electrostatic forces better and hence decrease systematic errors.

With the lens-plate combination, Casimir force at separations greater than 30 μm will be difficult to measure as electrostatic and gravitational forces will start to dominate. A similar experiment would be repeated with a flat plate instead of a lens for separation up to about 100 μm. The parallelism between this plate and suspension disc is less critical at these separations. The dependance of the Casimir force on separation will be $1/d^3$ as opposed to the typical $1/d^2$ or $1/d$ dependance of the other background forces. Such an experiment will be able to put stronger constraints on the new forces with strength close to that of gravity in the sub-millimeter range as the parallel plate configuration maximizes the sensitivity to these forces as opposed to the plate-sphere experiments.

We expect a 5% accurate measurement of the Casimir force in the range 10 μm to

100 μm, and also improved constraints on hypothetical Yukawa-type forces with range 10 μm to 100 μm, from these future experiments.

References

[1] E. G. Adelberger, B. R. Heckel, and A. E. Nelson. Tests of the Gravitational Inverse-Square Law. *Ann. Rev. of Nuclear and Particle Science*, 53:77-121 2003.

[2] N. Arkani-Hamed, S. Dimopoulos, and G. Dvali. Phenomenology, astrophysics, and cosmology of theories with submillimeter dimensions and TeV scale quantum gravity. *Phys. Rev. D*, 59:086004, April 1999.

[3] M. Bordag, B. Geyer, G. L. Klimchitskaya, and V. M. Mostepanenko. Constraints for hypothetical interactions from a recent demonstration of the Casimir force and some possible improvements. *Phys. Rev. D*, 58:075003, October 1998.

[4] M. Bordag, U. Mohideen, and V. M. Mostepanenko. New Developements in Casimir Force. *Phys. Rep.*, 353:1, 2001.

[5] R Cowsik. A new torsion balance for studies in gravitation and cosmology. *Indian Journal of Physics*, 55B:487, 1981.

[6] R Cowsik. Challenges in experimental gravitation and cosmology. Technical report, Dept. of Science & Technology, New Delhi, 1982.

[7] R Cowsik. Search for new forces in nature. In *From Mantle to Meteorites (Prof. D.Lal Festschrift)*, 1990.

[8] R. Cowsik, N. Krishnan, P. Sarawat, S. N Tandon, and S. Unnikrishnan. The Fifth Force Experiment at the TIFR. In *Gravitational Measurements, Fundamental Metrology and Constants*, 1988.

[9] R. Cowsik, N. Krishnan, P. Sarawat, S. N Tandon, and S. Unnikrishnan. Limits on the strength of the fifth-force. In *Advances in Space Research (Proc. XXI COSPAR, Espoo)*, 1989.

[10] R. Cowsik, N. Krishnan, S. N. Tandon, and C. S. Unnikrishnan. Limit on the strength of intermediate-range forces coupling to isospin. *Physical Review Letters*, 61:2179–2181, November 1988.

[11] R. Cowsik, S. N Tandon, and N. Krishnan. Sensitive test of Equivalence Principle. Technical report, Dept. of Science & Technology, New Delhi, 1982.

[12] S. Cullen and M. Perelstein. SN 1987A Constraints on Large Compact Dimensions. *Physical Review Letters*, 83:268–271, July 1999.

[13] R. S. Decca, E. Fischbach, G. L. Klimchitskaya, D. E. Krause, D. López, and V. M. Mostepanenko. Improved tests of extra-dimensional physics and thermal quantum field theory from new Casimir force measurements. *Phys. Rev. D*, 68:116003, December 2003.

[14] E. Fischbach, D. E. Krause, V. M. Mostepanenko, and M. Novello. New constraints on ultrashort-ranged Yukawa interactions from atomic force microscopy. *Phys. Rev. D*, 64:075010, October 2001.

[15] E. Fischbach and C. L. Talmadge. *The Search for Non-Newtonian Gravity*. The Search for Non-Newtonian Gravity, XVII, 305 pp. 58 figs.. Springer-Verlag New York, 1999.

[16] C. Genet. *La Force de Casimir Entre Deux Miroirs Metalliques À température Non Nulle*. PhD thesis, Laboratoire Kastler Brossel, University of Paris, Paris, Italy, 1999.

[17] C. Genet, A. Lambrecht, and S. Reynaud. Temperature dependence of the Casimir effect between metallic mirrors. *Phy.Rev. A*, 62:012110, July 2000.

[18] F. Grassia, J.-M. Courty, S. Reynaud, and P. Touboul. Quantum theory of fluctuations in a cold damped accelerometer. *European Physical Journal D*, 8:101–110, 2000.

[19] J. H. Gundlach, G. L. Smith, E. G. Adelberger, B. R. Heckel, and H. E. Swanson. Short-Range Test of the Equivalence Principle. *Physical Review Letters*, 78:2523–2526, March 1997.

[20] C. Hanhart, D. R. Phillips, S. Reddy, and M. Savage. Extra dimensions, SN1987a, and nucleon-nucleon scattering data. *Nuclear Physics B*, 595:335–359, February 2001.

[21] C. Hanhart, J. A. Pons, D. R. Phillips, and S. Reddy. The likelihood of GODs' existence: improving the SN 1987a constraint on the size of large compact dimensions. *Physics Letters B*, 509:1–2, June 2001.

[22] C. D. Hoyle, U. Schmidt, B. R. Heckel, E. G. Adelberger, J. H. Gundlach, D. J. Kapner, and H. E. Swanson. Submillimeter Test of the Gravitational Inverse-Square Law: A Search for "Large" Extra Dimensions. *Physical Review Letters*, 86:1418–1421, February 2001.

[23] N. Krishnan. *Search for Intermidiate Range forces Weaker than Gravity.* PhD thesis, Tata Institute of Fundamental Research, Mumbai, India, 1989.

[24] S. K. Lamoreaux. Demonstration of the Casimir Force in the 0.6 to 6 μ Range. *Phys. Rev. Lett*, 78:5, 1997.

[25] J. C. Long et al. Upper Limit on Submillimeter-range Forces from Extra Space-time dimensions. *Nature*, 421:924, 2003.

[26] V. M. Mostepanenko. Constraints on Non-Newtonian Gravity from Recent Casimir Force Measurements. *ArXiv General Relativity and Quantum Cosmology e-prints*, November 2003.

[27] C. S. Unnikrishnan. *Torsion Balance Experiments to Search for New Composition Dependant Forces.* PhD thesis, Tata Institute of Fundamental Research, Mumbai, India, 1992.

APPENDIX

A. CASIMIR FORCE BETWEEN INFINITE PARALLEL PLATES

The Casimir force is a manifestation of zero point energy of the electromagnetic field. In the quantum mechanical description of the electromagnetic field, the allowed energy levels of the electromagnetic wave of angular frequency ω are given by the Planck relation $E_n = (n + \frac{1}{2})\hbar\omega, n = 0, 1, 2, 3 \ldots$. The integer n, for the electromagnetic field, corresponds to the number of photons. The $n = 0$ or the 'vacuum' state also has an energy of $1/2\hbar\omega$ associated with it. Thus, vacuum is not empty and contains fluctuations of the electromagnetic field.

Let us now calculate the effect of two parallel conducting plates separated by a distance d, placed in such a field using the 'mode counting' technique [5]. The field modes within this cavity (Fig. A.1) are different from the free space modes. In addition to satisfying the wave equation, $\nabla^2\vec{A} = \frac{1}{c^2}\frac{\partial^2\vec{A}}{\partial t^2}$, together with, $\nabla.\vec{A} = 0$, the field inside should have the tangential component of electric field vanishing at the

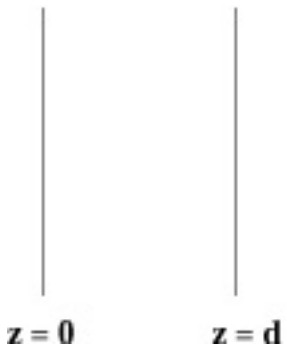

Fig. A.1: Two perfectly conducting infinite plates, placed distance d apart.

perfectly conducting boundaries. The solution that satisfies these conditions is given by,

$$\vec{A}(\vec{r}) = A_x(r)\hat{x} + A_y(r)\hat{y} + A_z(r)\hat{z}; \tag{A.1}$$

$$where \quad A_x(r) = \sqrt{\frac{8}{V}}\, a_x\, \cos k_x x\, \sin k_y y\, \sin k_z z, \tag{A.2}$$

$$A_y(r) = \sqrt{\frac{8}{V}}\, a_x\, \sin k_x x\, \cos k_y y\, \sin k_z z, \tag{A.3}$$

$$A_z(r) = \sqrt{\frac{8}{V}}\, a_x\, \sin k_x x\, \sin k_y y\, \cos k_z z; \tag{A.4}$$

with,

$$a_x^2 + a_y^2 + a_z^2 = 1; V = L^2 L_z \quad \& \tag{A.5}$$

$$k_x = \frac{\pi l}{L}; k_y = \frac{\pi m}{L}; k_z = \frac{\pi n}{L}; \qquad \text{where } l, m, n = 0, 1, 2, 3, \ldots \tag{A.6}$$

$\nabla.\vec{A} = 0$ also requires that

$$k_x A_x + k_y A_y + k_z A_z = 0 \quad \text{or} \tag{A.7}$$

$$\frac{\pi}{L}(lA_x + mA_x) + \frac{\pi}{L_z}(nA_z) = 0. \tag{A.8}$$

There are two polarizations possible for each value of l, m, n unless one of them is zero. In that case, only one polarization is possible due to Eqn. A.8. Thus, the allowed modes within the cavity are,

$$\omega_{lmn} = k_{lmn} c = \pi c \left(\frac{l^2}{L^2} + \frac{m^2}{L^2} + \frac{n^2}{L^2} \right)^{\frac{1}{2}}. \tag{A.9}$$

The zero-point energy of the field inside is,

$$E(d) = \sum_{lmn}{}' \, 2\frac{1}{2}\hbar\omega_{lmn} = \sum_{lmn}{}' \, \pi\hbar c \left(\frac{l^2}{L^2} + \frac{m^2}{L^2} + \frac{n^2}{L^2} \right)^{\frac{1}{2}}. \tag{A.10}$$

The factor 2 arises from the 2 independent polarizations for $l, m, n \neq 0$ and the prime on $\sum$ indicates that when l or m or $n = 0$, a factor of half has to be inserted.

When $L >> L_z = d$,

$$\begin{aligned}
\sum_{lmn}{}' &\longrightarrow \sum_{n}{}' \left(\frac{L}{\pi}\right)^2 \int\int dk_x dk_y \quad \text{and} \\
E(d) &= \sum_{lmn}{}' 2\frac{1}{2}\hbar\omega_{lmn} \qquad \text{(A.11)} \\
&= \left(\frac{L}{\pi}\right)^2 \hbar c \sum_{n=0}^{\infty}{}' \int_0^\infty \int_0^\infty dk_x dk_y \left(k_x^2 + k_y^2 + \frac{n^2\pi^2}{d^2}\right)^{\frac{1}{2}} \qquad \text{(A.12)}
\end{aligned}$$

This is *infinite*. Outside the cavity, $\sum_n$ will also be replaced by $\frac{d}{\pi}\int dk_z$ and

$$E(\infty) = \left(\frac{L}{\pi}\right)^2 \hbar c \frac{d}{\pi} \int_0^\infty \int_0^\infty \int_0^\infty dk_x dk_y dk_z \left(k_x^2 + k_y^2 + k_z^2\right)^{\frac{1}{2}}. \qquad \text{(A.13)}$$

This is also *infinite*. But the potential energy of the system when the plates are separated by a distance d is $U(d) = E(d) - E(\infty)$.

$$\begin{aligned}
U(d) &= \left(\frac{L}{\pi}\right)^2 \hbar c \left[\sum_{n=0}^{\infty}{}' \int_0^\infty \int_0^\infty dk_x dk_y \left(k_x^2 + k_y^2 + \frac{n^2\pi^2}{d^2}\right)^{\frac{1}{2}}\right. \\
&\quad \left. - \frac{d}{\pi}\int_0^\infty \int_0^\infty \int_0^\infty dk_x dk_y dk_z \left(k_x^2 + k_y^2 + k_z^2\right)^{\frac{1}{2}}\right]. \qquad \text{(A.14)}
\end{aligned}$$

In polar co-ordinates, u, θ in k_x, k_y plane, $dk_x dk_y = u du d\theta$, θ ranges from 0 to $\pi/2$ for positive k_x, k_y, and we have,

$$\begin{aligned}
U(d) &= \left(\frac{L}{\pi}\right)^2 \hbar c \frac{\pi}{2} \left[\sum_{n}{}' \int_0^\infty du\ u \left(u^2 + \frac{n^2\pi^2}{d^2}\right)^{\frac{1}{2}}\right. \\
&\quad \left. - \frac{d}{\pi}\int_0^\infty dk_z \int_0^\infty du\ u \left(u^2 + k_z^2\right)^{\frac{1}{2}}\right] \qquad \text{(A.15)}
\end{aligned}$$

This is still infinite. We now introduce a cut-off function $f(k) = f([u^2 + k^2]^{1/2})$ such that $f(k) = 1$ for $k << k_m$ and $f(k) = 0$ for $k >> k_m$. We could say that for wavelengths comparable to atomic dimensions, the assumption of perfect conductivity breaks down and hence a cut-off is necessary ($k_m \approx 1/a_0$, a_0 is Bohr radius). Thus,

Eqn. A.15 becomes,

$$U(d) = \left(\frac{L}{\pi}\right)^2 \hbar c \frac{\pi}{2}\left[\sum_{(n=0)}^{\infty}{}' \int_0^\infty du\, u\left(u^2+\frac{n^2\pi^2}{d^2}\right)^{\frac{1}{2}} f([u^2+k^2]^{\frac{1}{2}}) - \frac{d}{\pi}\int_0^\infty dk_z \int_0^\infty du\, u\left(u^2+k_z^2\right)^{\frac{1}{2}} f([u^2+k^2]^{\frac{1}{2}})\right] \quad \text{(A.16)}$$

Defining $x \equiv u^2d^2/\pi^2$ & $\kappa = k_z d/\pi$, (A.17)

$$= \frac{L^2\hbar c}{4\pi}\frac{\pi^3}{d^3}\left[\sum_n \int_0^\infty dx\left(x+n^2\right)^{\frac{1}{2}} f(\frac{\pi}{d}[x+k^2]^{\frac{1}{2}}) - \int_0^\infty d\kappa \int_0^\infty dx\left(x+\kappa^2\right)^{\frac{1}{2}} f(\frac{\pi}{d}[x+\kappa^2]^{\frac{1}{2}})\right]. \quad \text{(A.18)}$$

Now,

$$U(d) = \frac{\pi^2\hbar c}{4d^3}\left[\frac{1}{2}F(0)+\sum_{n=1}^{\infty}F(n)-\int_0^\infty d\kappa F(\kappa)\right]; \quad \text{(A.19)}$$

$$\text{where } F(\kappa) \equiv \int_0^\infty dx\left(x+\kappa^2\right)^{\frac{1}{2}} f(\frac{\pi}{d}[x+\kappa^2]^{\frac{1}{2}}). \quad \text{(A.20)}$$

According to Euler-Maclarin summation formula [1],

$$\sum_{n=1}^{\infty}F(n)-\int_0^\infty d\kappa F(\kappa) = -\frac{1}{2}F(0)-\frac{1}{12}F'(0)+\frac{1}{720}F''(0)+\cdots, \quad \text{(A.21)}$$

for $F(\infty)\to 0$. To evaluate $F^n(0)$, we note that,

$$F(\kappa)=\int_{\kappa^2}^\infty du\ \sqrt{u}f(\frac{\pi}{d}\sqrt{u}), \quad F'(\kappa)=-2\kappa^2 f(\frac{\pi}{d}\kappa). \quad \text{(A.22)}$$

Then $F'(0)=0, F'''(0)=-4$ and $F^n(0)=0$ for $n>3$, if the cut-off function vanishes at $\kappa=0$. Thus,

$$\sum_{n=1}^{\infty}F(n)-\int_0^\infty d\kappa F(\kappa) = -\frac{1}{2}F(0)-\frac{4}{720} \quad \text{(A.23)}$$

$$U(d) = \frac{\pi^2\hbar c}{4d^3}L^2\left(-\frac{4}{720}\right) \quad \text{(A.24)}$$

$$= \frac{\pi^2\hbar c}{720d^3}L^2 \quad \text{(A.25)}$$

which is finite and independent of the cut-off function. The attractive force per unit area,

$$F_c(d) = -\frac{\pi^2\hbar c}{240d^3}, \quad \text{(A.26)}$$

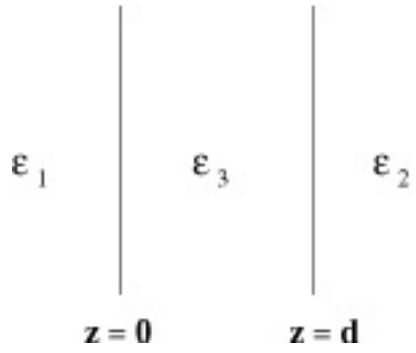

Fig. A.2: Two semi-infinite dielectric slabs of dielectric constants ϵ_1 and ϵ_2, placed distance d apart in a medium of dielectric constants ϵ_3.

which is the Casimir force. Thus, Casimir showed that changes in zero-point energy can be finite and observable.

A.1 Force between Dielectrics

In the previous section, we went through Casimir's derivation of the force between two perfectly conducting parallel plates. In experimental situations, the simplified assumption of perfect conductivity at all field frequencies is unrealistic. The dielectric properties of the media should also be included. Liftshitz [4], developed the first macroscopic theory of forces between dielectrics. His results reduce to the Casimir force derived above for the case of perfect conductors. We will now derive Lifshitz's results in a manner similar to Casimir's approach of mode counting [5].

Consider the case of a medium with dielectric constant $\epsilon_3(\omega)$ sandwiched between two semi-infinite media of dielectric constants $\epsilon_1(\omega)$ and $\epsilon_2(\omega)$ [Fig. A.2]. We will calculate the force per unit area from the total zero-point energy of the modes ω_n that are possible in this situation. The modes that are possible are the solutions of

the Maxwell's equations,

$$\begin{aligned} \nabla.\vec{D} &= 0, \\ \nabla \times \vec{E} &= -\frac{1}{c}\frac{\partial \vec{B}}{\partial t}, \\ \nabla.\vec{B} &= 0, \\ \nabla \times \vec{D} &= \frac{1}{c}\frac{\partial \vec{D}}{\partial t}, \end{aligned}$$

where, we have assumed the media to be isotropic, with magnetic permeability $\mu = 1$, and zero net charge density, so, $\vec{D}(\vec{r},t) = \epsilon(\omega)\vec{E}(\vec{r},t)$. These modes should also satisfy the appropriate boundary conditions. Consider solutions to the Maxwell's equations of the form $\vec{E}(\vec{r},t) = \vec{E_0}(\vec{r},t)e^{-i\omega t}$, $\vec{B}(\vec{r},t) = \vec{B_0}(\vec{r},t)e^{-i\omega t}$, such that in each region, $\nabla.\vec{E_0}, \nabla.\vec{B_0} = 0$ and,

$$\nabla^2\vec{E_0} + \frac{\omega^2}{c^2}\epsilon(\omega)\vec{E_0} = 0, \tag{A.27}$$

$$\nabla^2\vec{B_0} + \frac{\omega^2}{c^2}\epsilon(\omega)\vec{B_0} = 0. \tag{A.28}$$

Across the boundaries,

(i) normal component of $\vec{D}(= \epsilon\vec{E})$ should be continuous,

(ii) tangential component of $\vec{E}$ should be continuous,

(iii) normal component of $\vec{B}(= \vec{H})$ should be continuous, and

(iv) tangential component of $\vec{B}$ should be continuous.

Let us assume solutions of the form,

$$\vec{E_0}(\vec{r}) = [e_x(z)\hat{x} + e_y(z)\hat{y} + e_z(z)\hat{z}]\, e^{i(k_x x + k_y y)}, \tag{A.29}$$

$$\vec{B_0}(\vec{r}) = [b_x(z)\hat{x} + b_y(z)\hat{y} + b_z(z)\hat{z}]\, e^{i(k_x x + k_y y)}, \tag{A.30}$$

$$\text{so that,} \frac{d^2e_x}{dz^2} - K^2 e_x = 0, \qquad \frac{d^2b_x}{dz^2} - K^2 b_x = 0, \tag{A.31}$$

$$\text{where } K^2 = k_x^2 + k_y^2 - \frac{\omega^2}{c^2}\epsilon(\omega) \tag{A.32}$$

and likewise for y and z components. In free space, $\epsilon(\omega) = 1$ everywhere for all ω and the usual plane wave solutions are obtained for $K^2 < 0$; $k_x^2 + k_y^2 + k_z^2 = \frac{\omega^2}{c^2}$, $K^2 = -k_z^2$.

For the case under consideration, let us assume $\epsilon(\omega)$ to be real and $K^2 > 0$ in all three media. We can chose a coordinate system in which $k_y = 0$ and $K^2 = k^2 - \epsilon(\omega)\frac{\omega^2}{c^2}$, $k \equiv k_x$.

$$\nabla \vec{E_0} = 0, \text{ implies that } ike_x + \frac{de_z}{dz} = 0. \tag{A.33}$$

$\nabla \times \vec{E_0} = i\frac{\omega}{c}\vec{B_0}$, gives

$$\vec{B_0}(\vec{r}) = \left[i\frac{c}{\omega}\frac{de_y}{dz}\hat{x} - \frac{c}{\omega}\left(ke_z + i\frac{de_x}{dz} \right)\hat{y} + \frac{c}{\omega}ke_y\hat{z} \right] e^{ikx}. \tag{A.34}$$

$\nabla.\vec{B_0}$ is also identically satisfied by Eqn. A.34.

The boundary conditions mentioned above imply,

(i) $\epsilon(\omega)e_z(z)$ should be continuous,

(ii) e_x should be continuous which is satisfied if $\frac{de_x}{dz}$ is continuous (from Eqn. A.33), and

(iii) e_y should be continuous,

(iv) $\frac{de_y}{dz}$ and $ke_z + i\frac{de_x}{dz}$ should be continuous,

But, from Eqn. A.32 and A.33, $ke_z + i\frac{de_x}{dz} = \frac{1}{k}\epsilon(\omega)\frac{\omega^2}{c^2}e_z$. Thus, all conditions are satisfies if,

a. $\epsilon(\omega)e_z(z)$ and $\frac{de_x}{dz}$ are continuous, and

b. e_y and $\frac{de_y}{dz}$ are continuous.

Now, since $\frac{d^2e_z}{dz^2} - K^2e_z = 0$, in each region, ignoring exponential growing solutions, we have,

$$\begin{aligned} e_z(z) &= Ae^{k_1 z}, && \text{for } z < 0; && \text{(A.35)} \\ &= Be^{k_3 z} + Ce^{-k_3 z,} && \text{for } 0 \le z \le 0; && \text{(A.36)} \\ &= De^{-k_2 z,} && \text{for } z > 0; && \text{(A.37)} \end{aligned}$$

where $K_j^2 \equiv k^2 - \epsilon_j(\omega)\frac{\omega^2}{c^2}$. Applying the boundary conditions **'a'**, we have,

$$-\epsilon_1 A + \epsilon_3 B + \epsilon_3 C = 0; \tag{A.38}$$

$$-K_1 A + K_3 B - K_3 C = 0; \tag{A.39}$$

$$\epsilon_3 e^{K_3 d} B + \epsilon_3 e^{-K_3 d} C - \epsilon_2 e^{K_2 d} D = 0; \tag{A.40}$$

$$K_3 e^{K_3 d} B - K_3 e^{-K_3 d} C + K_2 e^{K_2 d} D = 0. \tag{A.41}$$

For non-trivial solutions to exist,

$$\begin{vmatrix} -\epsilon_1 & \epsilon_3 & \epsilon_3 & 0 \\ -K_1 & K_3 & -K_3 & 0 \\ 0 & \epsilon_3 e^{K_3 d} & \epsilon_3 e^{-K_3 d} & -\epsilon_2 e^{-K_2 d} \\ 0 & K_3 e^{K_3 d} & -K_3 e^{-K_3 d} & K_2 e^{-K_2 d} \end{vmatrix} = 0.$$

This yields,

$$\frac{\epsilon_3 K_1 + \epsilon_1 K_3}{\epsilon_3 K_1 - \epsilon_1 K_3} . \frac{\epsilon_3 K_2 + \epsilon_2 K_3}{\epsilon_3 K_2 - \epsilon_1 K_3} . e^{2K_3 d} - 1 = 0. \tag{A.42}$$

Similarly, it can be shown that the boundary conditions **'b'** are satisfied if,

$$\frac{K_1 + K_3}{K_1 - K_3} . \frac{K_2 + K_3}{K_2 - K_3} . e^{2K_3 d} - 1 = 0. \tag{A.43}$$

Equations A.42 and A.43 are the conditions on the allowed modes ω_n. Both cannot in general be satisfied simultaneously. For boundary conditions `a` and `b` to be satisfied simultaneously; (a) Eqn. A.42 should be satisfied with $e_y \equiv 0$ or (b) Eqn. A.43 should be satisfied with $e_z \equiv 0$. Thus we have two kinds of modes. Since these are exponentially decaying functions of z for $z < 0$ and $z > d$, these are called *surface modes* [2].

Let us now calculate the zero-point energy of these modes. The energy is given by,

$$E(d) = \sum_n \frac{1}{2}\hbar\omega_{na} + \sum_n \frac{1}{2}\hbar\omega_{nb}, \tag{A.44}$$

where ω_{na} are the modes of type (a) and ω_{nb} are the modes of type (b). Since k_x and k_y are continuous, the summations over them in $\omega_{n\alpha},\ \alpha = a, b$ can be replaced with integrals.

$$\sum_x \rightarrow \left(\frac{L}{2\pi}\right)^2 \int dk_x \int dk_y \sum_N = \left(\frac{L}{2\pi}\right)^2 \int 2\pi k dk \sum_N, \tag{A.45}$$

where L is the length along x and y sides of the 'quantization box' and $\sum_N$ denotes sum over the solutions of A.42 and A.43. Thus,

$$E(d) = \frac{\hbar L^2}{4\pi} \int_0^\infty dk\ k \left[\sum_N \omega_{Na}(k) + \sum_N \omega_{Nb}(k)\right]. \tag{A.46}$$

In order to evaluate this summation, we employ the 'argument theorem' from the theory of functions of complex variables: for a function $f(z)$ which is analytic except for poles on and inside a simple closed circle C,

$$\frac{1}{2\pi i} \oint_C \frac{f'(z)}{f(z)} dz = N - P, \tag{A.47}$$

where N is the number of zeros and P the number of poles $f(z)$ inside C (see for example, [3]). It can be shown from this that,

$$\begin{aligned} \frac{1}{2\pi i} \oint_C z \frac{f'(z)}{f(z)} dz &= \left[\sum_i z_i\right]_{f(z_i)=0} - \left[\sum_i z_i\right]_{f(z_i)=\infty}; & \text{(A.48)} \\ &= \text{sum of zero}'\text{s of } f(z_i) \text{ inside C} & \text{(A.49)} \\ &\quad - \text{sum of poles of } f(z_i) \text{ inside C.} & \text{(A.50)} \end{aligned}$$

Let $F_a(\omega)$ and $F_b(\omega)$ be the L.H.S of Eqns. A.42 and A.43 then,

$$\sum_N \omega_{N\alpha}(K) = \text{sum of zero}'\text{s of } F_\alpha,\ \alpha = a, b. \tag{A.51}$$

The poles of F_α, considered as function of complex variable ω, are independent of the boundaries and hence of d. Therefore,

$$\frac{1}{2\pi i} \oint_C \omega \frac{F'_\alpha(\omega)}{F_\alpha(\omega)} d\omega = \sum_N \omega_{N\alpha}(K) - \text{ (Term independant of } d). \tag{A.52}$$

The $\omega_{N\alpha}(K)$ of interest are those that are positive and real. Hence, the closed curve C is defined by the imaginary axis of complex ω plane and a semicircle in the right

half of this plane, with radius extending to infinity. As the d dependant term does not contribute to the force, for this analysis, we can write,

$$E(d) = \frac{\hbar L^2}{4\pi}\frac{1}{2\pi i}\int_0^\infty dk\ k\left[\oint_C \omega\frac{F_a'(\omega)}{F_a(\omega)}d\omega + \oint_C \omega\frac{F_b'(\omega)}{F_b(\omega)}d\omega\right]. \tag{A.53}$$

Each of these contour integrals, can be written as a part along the imaginary axis and a part along the infinite semicircle. The later integral is d-independent and does not contribute to the force. The former integral is,

$$\begin{aligned}\int_\infty^{-\infty} i\xi\frac{1}{F_\alpha(i\xi)}\frac{\partial F_\alpha(i\xi)}{\partial(i\xi)}id\xi &= -i\int_\infty^{-\infty} d\xi\ \xi\frac{G_\alpha'(\xi)}{G_\alpha(\xi)}; &\text{(A.54)}\\ &= -i\int_\infty^{-\infty} d\xi\ \xi\frac{d}{d\xi}\log G_\alpha(\xi); &\text{(A.55)}\\ &= i\int_{-\infty}^{\infty} d\xi\ logG_\alpha(\xi); &\text{(A.56)}\end{aligned}$$

where $G_\alpha(\xi) \equiv F_\alpha(i\xi),\ \alpha = a, b$. Writing explicitly,

$$\begin{aligned}G_a(\xi) &= \frac{\epsilon_3K_1+\epsilon_1K_3}{\epsilon_3K_1-\epsilon_1K_3}.\frac{\epsilon_3K_2+\epsilon_2K_3}{\epsilon_3K_2-\epsilon_1K_3}.e^{2K_3d}-1; &\text{(A.57)}\\ G_b(\xi) &= \frac{K_1+K_3}{K_1-K_3}.\frac{K_2+K_3}{K_2-K_3}.e^{2K_3d}-1; &\text{(A.58)}\end{aligned}$$

where, now $\epsilon_j = \epsilon_j(i\xi)$ and $K_j^2 = k^2 + \epsilon_j(i\xi)\frac{\xi^2}{c^2}$. The zero-point energy associated with the allowed modes is then,

$$E(d) = \frac{\hbar L^2}{8\pi^2}\int_0^\infty dk\ k\left[\int_{-\infty}^{\infty} d\xi\ logG_a(\xi) + \int_{-\infty}^{\infty} d\xi\ logG_a(\xi)\right] + \text{d independant term.} \tag{A.59}$$

The force $F(d) = -\frac{\partial}{\partial d}E(d)$,

$$F(d) = -\frac{\hbar L^2}{8\pi^2}\frac{\partial}{\partial d}\left[\int_0^\infty dk\ k\left\{\int_{-\infty}^{\infty} d\xi\ logG_a(\xi) + \int_{-\infty}^{\infty} d\xi\ logG_b(\xi)\right\}\right]. \tag{A.60}$$

But, from equation A.57 and A.58, $\frac{\partial}{\partial d}G_\alpha(\xi) = 2K_3\,(G_\alpha + 1)$, and

$$\begin{aligned}\frac{\partial}{\partial d}\int_{-\infty}^{\infty} d\xi\ logG_\alpha(\xi) &= \int_{-\infty}^{\infty} d\xi\ \frac{\partial}{\partial d}logG_\alpha(\xi); &\text{(A.61)}\\ &= \int_{-\infty}^{\infty} d\xi\ \frac{1}{G_\alpha(\xi)}\left[2K_3\,(G_\alpha+1)\right]; &\text{(A.62)}\\ &= 2\int_{-\infty}^{\infty} d\xi\ K_3 + 2\int_{-\infty}^{\infty} d\xi\ \frac{K_3}{G_\alpha(\xi)}. &\text{(A.63)}\end{aligned}$$

The first term is independent of the presence of the dielectric slabs and hence is not related to the force between them. Therefore, the force per unit area,

$$F(d) = -\frac{\hbar}{8\pi^2}\int_0^\infty dk\ k\int_{-\infty}^{\infty} d\xi\ 2K_3\left[\frac{1}{G_a(\xi)}+\frac{1}{G_b(\xi)}\right]. \tag{A.64}$$

K_j and ϵ_j are even functions of ξ, and so is G_α; Hence

$$F(d) = -\frac{\hbar}{2\pi^2}\int_0^\infty dk\ k\int_{0}^{\infty} d\xi\ K_3\left[\frac{1}{G_a(\xi)}+\frac{1}{G_b(\xi)}\right]. \tag{A.65}$$

More explicitly,

$$\begin{aligned} F(d) &= -\frac{\hbar}{2\pi^2}\int_0^\infty dk\ k\int_{0}^{\infty} d\xi\ K_3 \\ &\left[\left\{\frac{\epsilon_3K_1+\epsilon_1K_3}{\epsilon_3K_1-\epsilon_1K_3}.\frac{\epsilon_3K_2+\epsilon_2K_3}{\epsilon_3K_2-\epsilon_1K_3}.e^{2K_3d}-1\right\}^{-1}\right. \\ &\left.+\left\{\frac{K_1+K_3}{K_1-K_3}.\frac{K_2+K_3}{K_2-K_3}.e^{2K_3d}-1\right\}^{-1}\right]; \end{aligned} \tag{A.66}$$

where, $\epsilon_j = \epsilon_j(i\xi)$ and $K_j^2 = k^2+\epsilon_j(i\xi)\frac{\xi^2}{c^2}$.

To compare with Lifshitz theory we introduce a variable p such that,

$$k^2 = \epsilon_3\frac{\xi^2}{c^2}\left(p^2-1\right). \tag{A.67}$$

$$\text{Then, } K_3^2 = k^2+\epsilon_3\frac{\xi^2}{c^2} = \epsilon_3\frac{\xi^2}{c^2}p^2; \tag{A.68}$$

$$\begin{aligned} \text{and} K_{1,2}^2 = k^2+\epsilon_{1,2}\frac{\xi^2}{c^2} &= \epsilon_3\frac{\xi^2}{c^2}\left(p^2-1\right)+\epsilon_{1,2}\frac{\xi^2}{c^2}; \\ &= \epsilon_3\frac{\xi^2}{c^2}\left(p^2-1+\frac{\epsilon_{1,2}}{\epsilon_3}\right); \\ &\equiv \epsilon_3\frac{\xi^2}{c^2}s_{1,2}^2, \quad \text{where } s_{1,2}^2 = p^2-1+\frac{\epsilon_{1,2}}{\epsilon_3}. \end{aligned} \tag{A.69}$$

Changing to these set of variables, $dk\ k = \epsilon_3\frac{\xi^2}{c^2}dp\ p$ and,

$$\begin{aligned} F(d) &= -\frac{\hbar}{2\pi^2c^3}\int_1^\infty dp\ p^2\int_{0}^{\infty} d\xi\ \xi^3\epsilon_3^{3/2} \\ &\left[\left\{\frac{\epsilon_3s_1+\epsilon_1p}{\epsilon_3s_1-\epsilon_1p}.\frac{\epsilon_3s_2+\epsilon_2p}{\epsilon_3s_2-\epsilon_1p}.e^{2\xi p\sqrt{\epsilon_3}d/c}-1\right\}^{-1}\right. \\ &\left.+\left\{\frac{s_1+p}{s_1-p}.\frac{s_2+p}{s_2-p}.e^{2\xi p\sqrt{\epsilon_3}d/c}-1\right\}^{-1}\right] \end{aligned} \tag{A.70}$$

For the case when there is vacuum between the slabs, ($\epsilon_3 = 1$),

$$\begin{aligned} F(d) &= -\frac{\hbar}{2\pi^2 c^3}\int_1^\infty dp\ p^2 \int_0^\infty d\xi\ \xi^3 \\ &\left[\left\{\frac{s_1+\epsilon_1 p}{s_1-\epsilon_1 p}.\frac{s_2+\epsilon_2 p}{s_2-\epsilon_1 p}.e^{2\xi p d/c}-1\right\}^{-1}\right. \\ &\left.+\left\{\frac{s_1+p}{s_1-p}.\frac{s_2+p}{s_2-p}.e^{2\xi p d/c}-1\right\}^{-1}\right]. \end{aligned} \tag{A.71}$$

which matches with Lifshitz's result [4].

A.2 Casimir force at finite temperature

When we derived the Casimir pressure between the dielectric slabs, we assumed the vacuum state for the field and added only the zero-point energy of the allowed modes to calculate the energy of the field. At any finite temperature,

$$E_n = \left(n(\omega)+\frac{1}{2}\right)\hbar\omega, \text{ where } n(\omega) = \frac{1}{e^{\frac{\hbar\omega}{k_B T}}-1}. \tag{A.72}$$

Thus to calculate the energy of the allowed modes at a finite temperature, we have to use Eqn. A.72, rather than just $\frac{1}{2}\hbar\omega$,

$$E_{T>0}(d) = E(d).\frac{\left(n(\omega)+\frac{1}{2}\right)}{\frac{1}{2}}; \tag{A.73}$$

$$= E(d).2.\left(\frac{1}{e^{\frac{\hbar\omega}{k_B T}}-1}+\frac{1}{2}\right); \tag{A.74}$$

$$= E(d)\coth\frac{\hbar\omega}{2k_B T}. \tag{A.75}$$

The easiest way to now derive the force expression is to use $\omega = i\xi$ in Eqn. A.71 and multiply by the factor $\coth\frac{\hbar\omega}{2k_B T}$. For simplicity, let $\epsilon_3 = 1, K_3 = -i\frac{\omega}{c}p$ and,

$$\begin{aligned} F(d) &= -\frac{\hbar}{2\pi^2 c^3}\int_1^\infty dp\ p^2 \int_0^\infty d\omega\ \omega^3 \\ &\left[\left\{\frac{s_1+\epsilon_1 p}{s_1-\epsilon_1 p}.\frac{s_2+\epsilon_2 p}{s_2-\epsilon_1 p}.e^{-2i\omega p d/c}-1\right\}^{-1}\right. \\ &\left.+\left\{\frac{s_1+p}{s_1-p}.\frac{s_2+p}{s_2-p}.e^{-2i\omega p d/c}-1\right\}^{-1}\right]\coth\frac{\hbar\omega}{2k_B T}. \end{aligned} \tag{A.76}$$

To evaluate this integral, we could use $\omega \to i\xi$ as before. But, $\coth \frac{\hbar\omega}{2k_BT}$ has poles on the imaginary axis at $\omega_n = \frac{2\pi i n k_B T}{\hbar} \equiv i\xi_n$, for all integer n. So the closed curve C will now have semicircles around these poles in the path that runs along imaginary axis. The integration along the semicircles about ω_n contribute $i\pi$ times the residue of the integrand at ω_n for $n > 0$ and at $n = 0$ it will contribute $\frac{i\pi}{2}$ from the quarter circle.

$$\begin{aligned} F(d) &= -\frac{\hbar}{2\pi^2 c^3}\frac{2\pi i k_B T}{\hbar} i^3 {\sum_{n=0}}' \xi^3 \int_1^\infty dp\ p^2 \\ &\quad \left[\left\{ \frac{\epsilon_{1n} p}{s_{1n} - \epsilon_{1n} p} . \frac{s_{2n} + \epsilon_{2n} p}{s_{2n} - \epsilon_{1n} p} . e^{2\xi_n p d/c} - 1 \right\}^{-1} \right. \\ &\quad \left. + \left\{ \frac{s_{1n} + p}{s_{1n} - p} . \frac{s_{2n} + p}{s_{2n} - p} . e^{2\xi_n p d/c} - 1 \right\}^{-1} \right]; \end{aligned} \tag{A.77}$$

where $s_{jn} = \sqrt{p^2 - 1 + \epsilon_{jn}},\ \epsilon_{jn} = \epsilon_j(i\xi_n),\ j = 1, 2$ and the prime on the summation sign indicates that a factor half must be included in $n = 0$ term. This result was first derived by Lifshitz [4]. For the case when $\epsilon_{1,2} \to \infty$,

$$\begin{aligned} F(d) &= -\frac{k_B T}{\pi c^3} {\sum_{n=0}}' \xi^3 \int_1^\infty dp\ p^2 \left(\frac{2}{e^{2\xi_n p d/c} - 1} \right); \\ &= -\frac{2k_B T}{\pi c^3} {\sum_{n=0}}' \xi^3 \int_1^\infty dp\ \frac{p^2}{e^{2\xi_n p d/c} - 1}; \qquad \text{(A.78)} \\ &= -\frac{2k_B T}{\pi c^3} \frac{c^3}{8d^3} {\sum_{n=0}}' \int_{nx}^\infty dy\ \frac{y^2}{e^y - 1}; \qquad \text{(A.79)} \end{aligned}$$

where $x \equiv \frac{4\pi k_B T d}{\hbar c}$. When $x \gg 1$, the dominant contribution if from the $n = 0$ term

$$\begin{aligned} F(d) &= -\frac{k_B T}{4\pi d^3} \frac{1}{2} \int_0^\infty dy\ \frac{y^2}{e^y - 1}; \qquad \text{(A.80)} \\ &= -\frac{\zeta(3) k_B T}{4\pi d^3}. \qquad \text{(A.81)} \end{aligned}$$

Note that the distance dependance changes from $1/d^4$ at 'low temperature' to $1/d^3$ at 'high temperature'. Also, the high and low temperature regime are defined by the dimensionless parameter $x \equiv \frac{4\pi k_B T d}{\hbar c}$. At any given temperature T, we can always choose a large enough d, such that $x \gg 1$. Thus, low or high temperature is equivalent to smaller or larger separations.

References

[1] M. Abramowitz and Stegun I. A. *Handbook of Mathematical Functions.* Dover Books, Newyork, 1971.

[2] G. Barton. Some Surface Effects in the Hydrodynamic Model of Metals. *Rep. Prog. Phys.*, 42:963, 1979.

[3] M. L Boas. *Mathematical Methods in the Physical Sciences.* Wiley, Newyork, 1983.

[4] E. M. Lifshitz. Theory of molecular attraction between solids. *Sov. Phys. JETP*, 2:73, 1956.

[5] W. P Milonni. *The Quantum Vacuum: An Introduction to Quantum Electrodynamics.* Academic Press, Newyork, 1994.

B. CASIMIR FORCE BETWEEN SPHERICAL LENS AND FLAT PLATE

The Casimir force per unit area between two parallel conducting plates, at $T = 0$ K is given by,

$$f_{c0}(z) = -\frac{\pi^2 \hbar c}{240 z^4} \tag{B.1}$$

$$= -\frac{0.013}{z_\mu^4} \quad \text{dyn.cm}^{-2} \quad \text{where } z_\mu \equiv z \text{ in microns.} \tag{B.2}$$

For a finite temperature T we approximate the distance dependence as

$$f_{cT}(z) = f_{c0}(z), \qquad \text{for} \quad z < \lambda_T; \tag{B.3}$$

$$f_{cT}(z) = f_{c0}(z)\frac{z}{\lambda_T}, \qquad \text{for} \quad z > \lambda_T. \tag{B.4}$$

For convenience, we write Eqns. B.1 and B.4 as,

$$f_{c0}(z) \equiv -\frac{A_c}{z^4} \quad \text{dyn.cm}^{-2}, \tag{B.5}$$

$$f_{cT}(z) \equiv -\frac{A_c}{\lambda_T z^3} \quad \text{dyn.cm}^{-2}, \tag{B.6}$$

$$\text{where} \quad A_c = \frac{\pi^2 \hbar c}{240}. \tag{B.7}$$

The Casimir force between the lens and plate can now be estimated using the "Derjaguin (proximity) approximation", often called "proximity theorem" [1]. Here the total force is calculated by integrating over concentric rings on the lens surface that are equidistant from the plate. Thus, the Casimir force between the lens and plate is

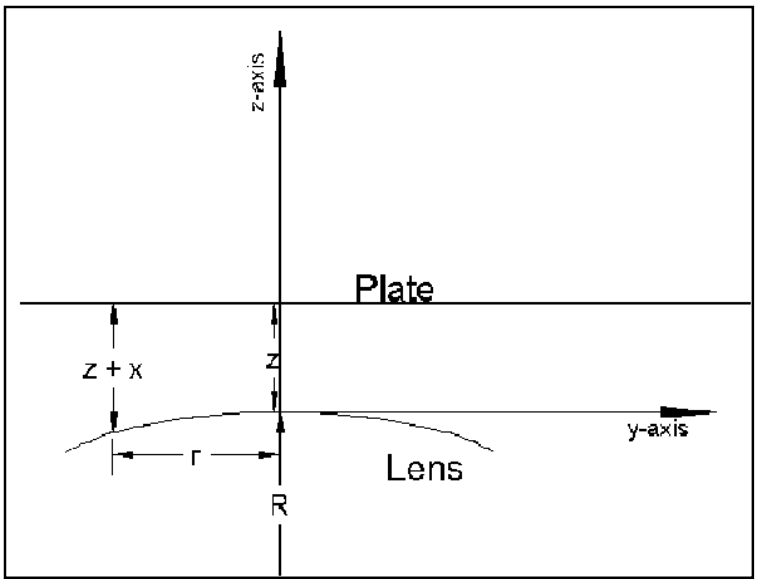

Fig. B.1: Reference axes for the system.

given by,

$$f_{cl}(z) = \int_0^{r_{max}} f(z + x(r)).2\pi r.dr, \tag{B.8}$$

$$\text{with} \quad (2R - x)x = r^2; \tag{B.9}$$

$$x \approx \frac{r^2}{2R}, \tag{B.10}$$

where z is the separation between the lens and the plate, R is the radius of curvature of the lens and r_{max} is the aperture radius of the lens [Fig. B.1]. The function, $f(z)$, takes different forms depending on z as compared with λ_T. For $\mathbf{z < \lambda_T}$,

$$f_{cl}(z) = \int_0^{\sqrt{2R\lambda_T}} f_{c0}(z + x(r)).2\pi r.dr + \int_{\sqrt{2R\lambda_T}}^{r_{max}} f_{cT}(z + x(r)).2\pi r.dr \tag{B.11}$$

$$= \int_0^{\sqrt{2R\lambda_T}} 2\pi A_c \frac{rdr}{\left(z + \frac{r^2}{2R}\right)^4} + \int_{\sqrt{2R\lambda_T}}^{r_{max}} \frac{2\pi A_c}{\lambda_T} \frac{rdr}{\left(z + \frac{r^2}{2R}\right)^3} \tag{B.12}$$

$$= -\frac{2\pi RA_c}{3}\left\{\frac{1}{z^3} - \frac{1}{(z + \lambda_T)^3}\right\} \tag{B.13}$$

$$-\frac{2\pi RA_c}{2\lambda_T}\left\{\frac{1}{(z + \lambda_T)^2} - \frac{1}{\left(z + \frac{r_{max}^2}{2R}\right)^2}\right\} \tag{B.14}$$

$$f_{cl}(z) = -\frac{2\pi RA_c}{3}\left[\frac{1}{z^3} - \frac{1}{(z + \lambda_T)^3} + \frac{3}{2\lambda_T}\left\{\frac{1}{(z + \lambda_T)^2} - \frac{1}{(z + x_{max})^2}\right\}\right] \tag{B.15}$$

where $x_{max} = \frac{r_{max}^2}{2R}$. For $\mathbf{z} > \lambda_{\mathbf{T}}$,

$$f_{cl}(z) = \int_0^{r_{max}} f_{cT}(z + x(r)).2\pi r.dr \quad \text{(B.16)}$$

$$= -\frac{\pi R A_c}{\lambda_T}\left[\frac{1}{z^2} - \frac{1}{(z + x_{max})^2}\right]. \quad \text{(B.17)}$$

References

[1] J. Blocki et al. . *Ann. Phys. (N.Y.)*, 105:427, 1977.

C. YUKAWA FORCE ON A GOLD COATED LENS DUE TO GOLD COATED PLATE

Let the Yukawa potential due to a point mass m at a distance r from the mass be given by,

$$Y(r) \;=\; -mG\alpha\frac{e^{-r/\lambda}}{r}. \tag{C.1}$$

Consider a glass plate of thickness, g and density, ρ_v, coated with a thin layer of gold of thickness, Δ and density, ρ_s. The Yukawa potential due to the plate at a height, z [Fig. C.1] from the surface of the plate is obtained by integrating the contribution

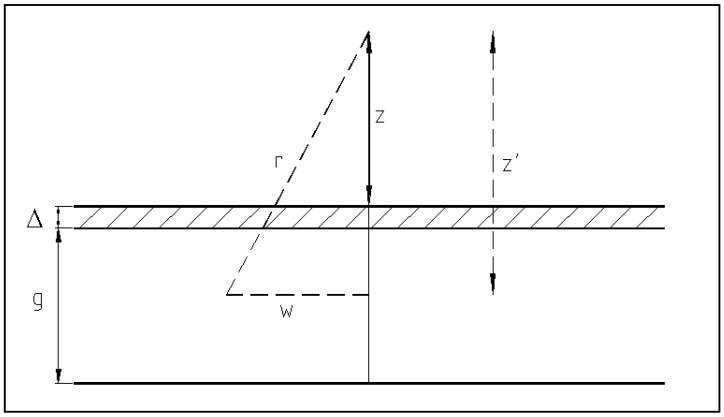

Fig. C.1: Schematic of the plate with coating.

due to various mass elements on the plate,

$$U(z) = -G\alpha \int \rho(r)\ \frac{e^{-r/\lambda}}{r} dV; \tag{C.2}$$

$$\text{where} \quad r^2 = w^2 + z'^2. \tag{C.3}$$

$$U(z) = -G\alpha \int \rho(z')\ \frac{e^{-\sqrt{(w^2+z'^2)}/\lambda}}{\sqrt{(w^2+z'^2)}} 2\pi w\ dw\ dz' \tag{C.4}$$

$$= -G\alpha 2\pi \int_{z+g+\Delta}^{z} dz'\ \rho(z') \int_{z'}^{\infty} dr\ e^{-r/\lambda} \tag{C.5}$$

$$= -2\pi G\alpha\lambda \int_{z+g+\Delta}^{z} dz' \rho(z') e^{-z'/\lambda} \tag{C.6}$$

$$= -2\pi G\alpha\lambda \left(\rho_v \int_{z+g+\Delta}^{z+\Delta} dz'\ e^{-z'/\lambda} + \rho_s \int_{z+\Delta}^{z} dz'\ e^{-z'/\lambda} \right) \tag{C.7}$$

$$= 2\pi G\alpha\lambda^2 \left[\rho_v \left\{ e^{-(z+\Delta)/\lambda} - e^{-(z+g+\Delta)/\lambda} \right\} + \right.$$

$$\left. \rho_s \left\{ e^{-z/\lambda} - e^{-(z+\Delta)/\lambda} \right\} \right]. \tag{C.8}$$

For $\lambda << g$, (C.9)

$$U(z) \approx 2\pi G\alpha\lambda^2 \left[\rho_v e^{-(z+\Delta)/\lambda} + \rho_s \left\{ e^{-z/\lambda} - e^{-(z+\Delta)/\lambda} \right\} \right]. \tag{C.10}$$

Keeping in mind that our interest is in the region $\lambda << g$ we use Eqn. C.10 in further analysis. The force due to this potential is,

$$f(z) = -\frac{\partial U}{\partial z} \tag{C.11}$$

$$= 2\pi G\alpha\lambda \left[\rho_v e^{-(z+\Delta)/\lambda} + \rho_s \left\{ e^{-z/\lambda} - e^{-(z+\Delta)/\lambda} \right\} \right] \tag{C.12}$$

$$= 2\pi G\alpha\lambda \left[\rho_s - (\rho_s - \rho_v) e^{-\Delta/\lambda} \right] e^{-z/\lambda} \tag{C.13}$$

$$= f_c e^{-z/\lambda}; \tag{C.14}$$

$$\text{where } f_c = 2\pi G\alpha\lambda \left[\rho_s - (\rho_s - \rho_v) e^{-\Delta/\lambda} \right]. \tag{C.15}$$

The lens has a radius of curvature R, a volume density ρ_l and a surface coating of uniform thickness δ with density ρ_c. We now proceed to derive the force on the lens in two limiting cases: (a) $\lambda << \delta$ and (b) $\lambda >> \delta$.

Case (a): $\lambda << \delta$ Here the lens may be assumed to be completely made of the coating material alone.

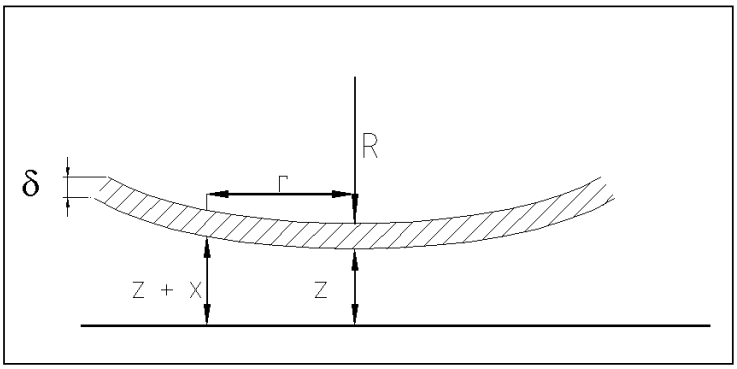

Fig. C.2: Schematic of the lens with coating.

$$\mathcal{F}_a(z) = \int f(z')\ \rho_c\ dV_l; \tag{C.16}$$

$$= \int f_c e^{-(z+x)/\lambda} \rho_c\ \delta\ dA(x); \tag{C.17}$$

$$\text{where } r^2 = 2Rx. \tag{C.18}$$

$$\mathcal{F}_a(z) = f_c\ \rho_c\ \delta\ e^{-z/\lambda} \int_0^{r_{max}} e^{-r^2/2R\lambda} 2\pi r dr \tag{C.19}$$

$$= f_c\ \rho_c\ \delta\ e^{-z/\lambda}\ 2\pi R\lambda \left(1 - e^{-r_{max}^2/2R\lambda}\right) \tag{C.20}$$

$$\text{For} \quad r_{max}^2/2R >> \lambda, \tag{C.21}$$

$$\mathcal{F}_a(z) \approx f_c\ 2\pi R\lambda\rho_c\ \delta\ e^{-z/\lambda}. \tag{C.22}$$

Case (b): $\lambda >> \delta$ This case contains two terms one for the contribution from the coating and the other for the body of the lens.

b1. Contribution from the coating: This is same as in case (a) and is given by Eqn.C.22.

$$\mathcal{F}_{b1}(z) = f_c\ 2\pi R\lambda\rho_c\ \delta\ e^{-z/\lambda}. \tag{C.23}$$

b2. Contribution from the lens:

$$\mathcal{F}_{b2}(z) = \int f(z')\ \rho_l\ dV_l; \tag{C.24}$$

$$= \int f_c\ e^{-(z+\delta+x)/\lambda}\ \rho_l\ \pi r^2 dx, \tag{C.25}$$

$$= f_c\, e^{-(z+\delta)/\lambda}\, \rho_l \int_0^{r_{max}^2/2R} e^{-x/\lambda}\, 2\pi R x dx \tag{C.26}$$

$$= f_c\, e^{-(z+\delta)/\lambda}\, \rho_l\, 2\pi R\lambda \left[-\frac{r_{max}^2}{2R}\, e^{r_{max}^2/2R\lambda} + \lambda \left(1 - e^{r_{max}^2/2R\lambda} \right) \right]. \tag{C.27}$$

For $r_{max}^2/2R >> \lambda$, (C.28)

$$\mathcal{F}_{b2}(z) \approx f_c\, e^{-(z+\delta)/\lambda}\, \rho_l\, 2\pi R\lambda. \tag{C.29}$$

The net force due to Yukawa potential between the lens and the plate for $\lambda >> \delta$ is given by,

$$\mathcal{F}_b = \mathcal{F}_{b1} + \mathcal{F}_{b2} \tag{C.30}$$

$$= f_c\, 2\pi R\lambda \left(\rho_c\, \delta + \rho_l\, \lambda\, e^{-\delta/\lambda} \right)\, e^{-z/\lambda}. \tag{C.31}$$

In the case our experimental set up, the lens and the plate are both made of the same material (BK7 glass) and coated with the gold of equal thickness (1 μm). Hence,

$$\rho_l = \rho_v\ ;\ \rho_c = \rho_s \text{ and } \Delta = \delta \tag{C.32}$$

Thus, the force in the two cases is given by,

$$\mathcal{F}_a(z) = 4\pi^2 G\alpha R\lambda^2 \left[\rho_s - (\rho_s - \rho_v) e^{-\delta/\lambda} \right]\, \rho_s\, \delta\, e^{-z/\lambda}, \quad \text{for } \lambda << \delta. \tag{C.33}$$

$$\mathcal{F}_b(z) = 4\pi^2 G\alpha R\lambda^2 \left[\rho_s - (\rho_s - \rho_v) e^{-\delta/\lambda} \right] \left(\rho_s\, \delta + \rho_v\, \lambda\, e^{-\delta/\lambda} \right)\, e^{-z/\lambda}, \tag{C.34}$$

for $\lambda >> \delta$.